Review Article

Nano Research
2022, 15(1): 38–70

ISSN 1998-0124 CN 11-5974/O4
https://doi.org/10.1007/s12274-021-3479-8

Applications of single-atom catalysts

Qiaoqiao Zhang and Jingqi Guan (✉)

Institute of Physical Chemistry, College of Chemistry, Jilin University, Changchun 130012, China

Received: 11 February 2021 / **Revised:** 27 March 2021 / **Accepted:** 29 March 2021

ABSTRACT

Owing to unsaturated coordination environment, quantum size effect and metal-support interaction, single- or dual-atom metal sites, such as Mn, Fe, Co, Ni, Cu, Zn, Mo, Ru, Rh, Pd, Ag, Sn, Ir, Pt, Au, Bi, and Er coordinated with nonmetallic elements such as O, N, P, and S, exhibit different electronic configurations, which endow them with high catalytic performances in multiple redox reactions and versatile applications in organic synthesis, environmental remediation, energy conversion, and biomedicine. Despite intense research, the relation of structure-activity for single-atom catalysts (SACs) still bedazzles researchers, since diversified configurations of active sites would bring about difficulty in structural identification and theoretical simulations. Here, recent results on the applications of SACs are reviewed with an emphasis on identifying the active sites and discussing the relation between structure and property.

KEYWORDS

biomedicine, energy conversion, environmental remediation, organic synthesis, single-atom catalysis

1 Introduction

Metal-containing nanomaterials have played an important role in heterogeneous catalysis to date, which are explored in extensive applications ranging over fine chemicals synthesis, energy conversion and storage, automobile emission regulation, sewage treatment, healthcare, and molecular sensing [1–5]. With the rapid development of nanotechnology, diverse nanocatalysts have been fabricated to promote the desired reactions [6–8]. Over the past few years, great progress has been made in practical applications of nanocatalysts, such as organic synthesis, industrial catalysis, air pollution control (including indoor air purification, fumes desulfurization and control of automobile tail gas), and cancer therapy [9–11]. Nevertheless, some disadvantages of nanocatalysts still exist, such as agglomeration of active metal species, catalyst poisoning, and loss of active components during long-time operation. Moreover, multiple elemental compositions and sophisticated structures of most nanocatalysts make them difficult to identify the real active sites and further unveil the relation of structure-activity for many catalytic reactions [12]. Hence, it is vitally important to take measures to construct catalysts with abundant and well-defined active sites. Recently, single-atom catalysts (SACs) are emerging as a new frontier in heterogeneous catalysis, which possess the maximum atom utilization and uniform active sites [13, 14]. Different from conventional nanocatalysts, the metal sites in SACs are isolated, which can be modified by different ligands with various coordination numbers, leading to much higher intrinsic activity of each active site than that in conventional nanocatalysts. Actually, the first discovery of SACs can ascend to the report by Thomas et al. in 1995 [15]. They found that highly dispersed Ti species supported on mesoporous silica can favorably catalyze the epoxidation of cyclic alkenes. In 2011, Zhang and co-workers synthesized atomically dispersed Pt on iron oxide (Pt_1/FeO_x) through coprecipitation method, and the concept of "single-atom catalysis/catalysts" was firstly put forward [16]. Afterwards, SACs, with isolated metal sites highly dispersed on various substrates, have drawn great attention. High activity and selectivity on SACs can be attributed to their 100% atom utilization and consistent configuration of active sites [17]. Furthermore, the strong interaction between isolated metal atoms and supports can help to realize good stability of SACs, and the highly dispersed metal sites in SACs contribute to the exact identification and characterization of active centers, leading to an in-depth insight into the relation of structure-property for specific catalytic reactions [18–21].

Nowadays, atomically dispersed transition metal-based catalysts have been designed, and significant achievements have been acquired in the synthesis, characterization, and experimental and theoretical research of single-/dual-metal-site SACs for catalytic reactions [22–26]. For example, organic transformations on SACs have been extensively reported so far, including hydrogenation, oxidation, hydroformylation, reforming, and coupling reactions [27]. With the aid of SACs, some valuable fine chemicals can be effectively and selectively produced, which can be used to manufacture pharmaceuticals, agrochemicals, food additives, dyestuffs, etc.. It has been reported that the degradation of gaseous/organic contaminant can also be facilitated by SACs, and much research on electrochemical technology/devices (such as water splitting, metal-air batteries, H_2/O_2 fuel cells) has been currently carried out at the atomic level [28–39]. The successful construction of SACs is conducive to realizing rapid energy conversion and storage, alleviating energy crisis and environmental problems to some extent. In the terms of heterogenous catalysis, some breakthroughs in the biomedicine have also been reported. Especially, SACs have played a significant role in cancer treatment, wound healing, bioassay, and biosensing applications [25, 40].

Address correspondence to guanjq@jlu.edu.cn

In this review, we summarize the recent progress of versatile applications of SACs in organic synthesis, environmental remediation, energy conversion, and biomedicine. Firstly, the preparation and characterization methods of SACs are introduced. Then, the catalytic performances and active sites of SACs are evaluated and analyzed for specific reactions. Some prominent cases of SACs in diverse fields are summarized with emphasis on unveiling the relation of structure-performance and catalytic mechanisms. Lastly, the promising prospects and tough challenges on single-atom catalysis are discussed.

2 Experimental preparation and characterization of SACs

2.1 Preparation methods

2.1.1 *Bottom-up strategies*

For the fabrication of most SACs, bottom-up strategies including mass-selected soft-landing, atomic-layer deposition, wet-chemistry, ball milling methods, etc. are generally adopted, where metal precursors are subsequently adsorbed, reduced, and confined by the vacancies/defects of supports [41–43]. Especially, wet-chemistry method has been extensively applied in labs without any specialized equipment, which is promising for the large-scale production of SACs [44, 45]. The common wet-chemistry routes include the introduction of metal precursors and subsequent calcination/activation. The anchoring of metal-containing complexes on supports can be achieved through chemical coordination. For instance, through coprecipitation and subsequent calcination process, Zhang and co-workers synthesized an atomic Pt_1/FeO_x catalyst for CO oxidation [16]. During coprecipitation, the mixture of $H_2PtCl_6{\cdot}6H_2O$ and $Fe(NO_3)_3{\cdot}9H_2O$ and Na_2CO_3 solution were chosen as the metal precursor and precipitant, respectively. As for the activation step, reductive/oxidative treatments are involved [46–48]. Taking the photochemical reduction for example, the preparation process of an atomically dispersed Pt-based catalyst was illustrated in Fig. 1(a) [48]. The frozen H_2PtCl_6 aqueous solution was irradiated with ultraviolet (UV) light, by which Pt^{4+} can be photochemically reduced onto various support materials (graphene, mesoporous carbon, multi-walled carbon nanotubes, TiO_2 nanoparticles, and ZnO nanowires).

In the terms of gas-phase synthesis approach, atomic layer deposition (ALD) has been viewed as a kind of powerful physicochemical vapor deposition method to prepare SACs. ALD is based on the surface reaction between gas-phase metal precursors and solid supports, by which the amount of deposited metal atoms can be accurately controlled by regulating the cycle numbers [49]. Furthermore, the uniform deposition of isolated metal atoms can be achieved on various substrates by this method, which shows great superiority [50]. Nevertheless, the large-scale production of SACs is still limited due to high cost and slow deposition rate of ALD. Moreover, single-atom alloys (SAAs) (such as Pd/Cu, Pd/Au, and Pt/Cu SAAs) can be synthesized by physical vapor deposition (PVD) strategies (including magnetron sputtering, sputtering ion plating, and plasma coating) [51–55]. Under ultrahigh vacuum, the isolated metal atoms anchored onto substrate can be realized via electron beam evaporators. However, special equipment and harsh experimental conditions are required for the PVD method [56]. Electrodeposition is also regarded as an adoptable way to fabricate SACs, by which the target metal species in electrolyte solutions are commonly deposited on cathodes, resulting in the stabilization of single metal atoms on various supports [57, 58]. The regulation of anode voltage and deposition time can help to control precisely atomic dispersion. The electrochemical deposition technology has been employed to synthesize single-atom Co, Ru, Pd, Pt, and Au on MoS_2 and other two-dimensional (2D) materials, which exhibited superior catalytic performances [59–61]. For the fabrication of Pt SACs, the deposition of Pt on cathodes can be realized using Pt foils/wires as counter electrodes. In a three-electrode system, Tan et al. used this approach to realize the embedding of single Pt atoms into Co vacancies (Fig. 1(b)), and the formed Pt/np-$Co_{0.85}Se$ showed high hydrogen evolution reaction (HER) activity under the neutral condition [62]. However, some challenges exist in the electrodeposition method. In the presence of other species in electrolyte solution, the resultant SACs may be polluted. Additionally, the adhesion of single metal atoms onto supports is also a considerable issue. As a potential bottom-up strategy, ball milling method has been developed to prepare SACs, which can achieve effective break and reconstruction of chemical bonds due to the input of high mechanical energy [63, 64]. As reported by Guo et al., atomically dispersed Fe on SiO_2 (Fe©SiO_2) was successfully prepared via the high-energy ball milling of ferrous metasilicate (Fe_2SiO_4) with SiO_2 in air [64]. The single metal atoms on graphene have also been constructed by the ball milling of metal phthalocyanines with graphene nanosheets [65, 66]. Such

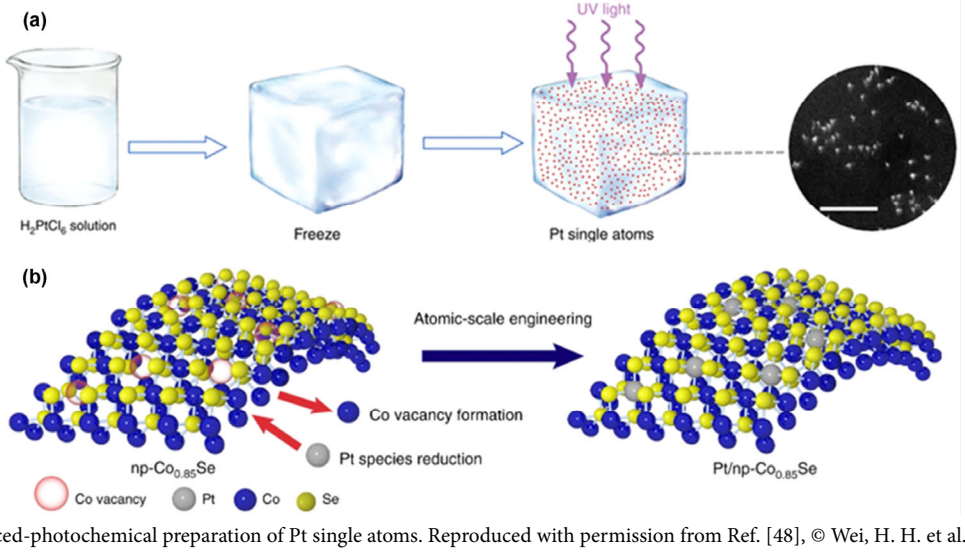

Figure 1 (a) The iced-photochemical preparation of Pt single atoms. Reproduced with permission from Ref. [48], © Wei, H. H. et al. 2017. (b) Schematic illustration for the fabrication of Pt/np-$Co_{0.85}Se$. Reproduced with permission from Ref. [62], © Jiang, K. et al. 2019.

method is low-cost and simple, and the size of SACs can be well controlled by adjusting rotational speed of balls. The resultant SACs by ball milling may be contaminated, arising from the balls and milling additives.

2.1.2 *Top-down strategies*

Based on the disbanding of ordered nanostructures into smaller pieces, top-down strategies are capable of realizing precise control of atomic structures [67, 68]. Over the last few years, high-temperature pyrolysis and gas-phase migration methods have been regarded as the main top-down synthesis techniques of SACs, which exhibited great perspectives in industrial applications [69]. In the terms of preparation of SACs, high-temperature pyrolysis is extensively developed, in which various precursors are selected to be decomposed under appropriate temperatures and gas atmospheres. This top-down synthesis strategy has been used to fabricate many carbon-based SACs, especially for atomically dispersed metals on N-doped porous carbon [63]. As regular porous materials, metal-organic frameworks (MOFs) have attracted great interest, whose three-dimensional (3D) molecular-scale cages are favorable for facile access of small molecules. By high-temperature pyrolysis of porous MOFs, high-surface-area SACs can be prepared. For the preparation of MOF-derived SACs, zeolitic imidazolate frameworks (ZIFs) and derivatives as precursors/templates are often explored. Li and co-workers reported that single-atom Co on N-doped carbon (Co SAs/N-C) can be fabricated by pyrolyzing a Zn/Co bimetallic ZIF [70]. During high-temperature pyrolysis, the evaporation of Zn can help to form abundant N sites, and the Co nodes were *in situ* reduced and further anchored on N-doped carbon (Fig. 2(a)). The incorporation of Zn was conducive to regulating the distance between Co atoms, which can help to prevent the formation of Co nanoparticles. They also reported that the ligand (2-amino terephthalic acid) of a derivative MOF UiO-66-NH_2 can be used to stabilize Ru ions, and Ru single atoms/clusters were *in situ* embedded into the porous carbon architecture by further pyrolysis and HF etching (Fig. 2(b)) [71]. Moreover, it was found that the adsorption of $Ru_3(CO)_{12}$ in the cavity of ZIF-8 and subsequent pyrolysis can lead to the formation of Ru_3 clusters for alcohol oxidation reactions (Fig. 2(c)) [72]. Under high-temperature condition, the mixture of metal salt with carbon source and irregular metal-containing complexes/polymers have also been pyrolyzed to obtain atomically dispersed catalysts. For instance, Ni SACs with high metal loading (~ 20 wt.%) can be prepared by pyrolysis of the mixture of $Ni(acac)_2$ and dicyandiamide [73]. The Mn-EDA-Cl (EDA = ethylenediamine) polymer was reported as the precursor to fabricate a N, Cl-coordinated single-atom Mn catalyst for electrochemical CO_2 reduction [74]. Noteworthily, template-assisted pyrolysis method is regarded as an important strategy to create 3D porous structures. With the addition of hard/soft template agents (SiO_2, a-FeOOH, water-soluble surfactant F127, etc.), abundant active sites of SACs can be exposed for various catalytic reactions [69, 75–77]. In the pyrolysis process, the migration and aggregation of metal species should be considered, which can be controlled by adjusting temperature, heating rate, gas flow velocity, etc.

Moreover, high-temperature atomic migration method has also been reported for the fabrication of SACs, which can effectively avoid the aggregation of metal species into larger particles [42]. Generally, metal nanoparticles are anchored on the target support through *in situ* trapping, which are then converted into the single metal atoms by high-temperature treatment. It has been found that single metal atoms supported on N-doped carbon can be synthesized by this method. For example, Li and co-workers used ZIF-8 to encapsulate Pd, Pt, and Au nanoparticles, followed by a heating treatment [78]. As a result, stable single noble metal atoms on N-doped carbon were converted from metal nanoparticles at 900 °C under inert gas atmosphere. They also fabricated porphyrin-like single Fe sites on N-doped carbon using high-temperature atomic migration method [79]. At high temperature, volatile Fe atoms were successfully produced from Fe powders, which were further migrated to N-doped carbon under N_2 atmosphere. By high-temperature atomic migration, SACs can also be manufactured from metal bulks. It is worth noting that metal bulks are more difficult to be volatilized to single metal atoms as compared to metal nanoparticles, which limits the practical applications to some extent.

2.2 Characterization methods

2.2.1 *Techniques for the identification of isolated metal atoms*

Scanning transmission electron microscopy (STEM) and TEM

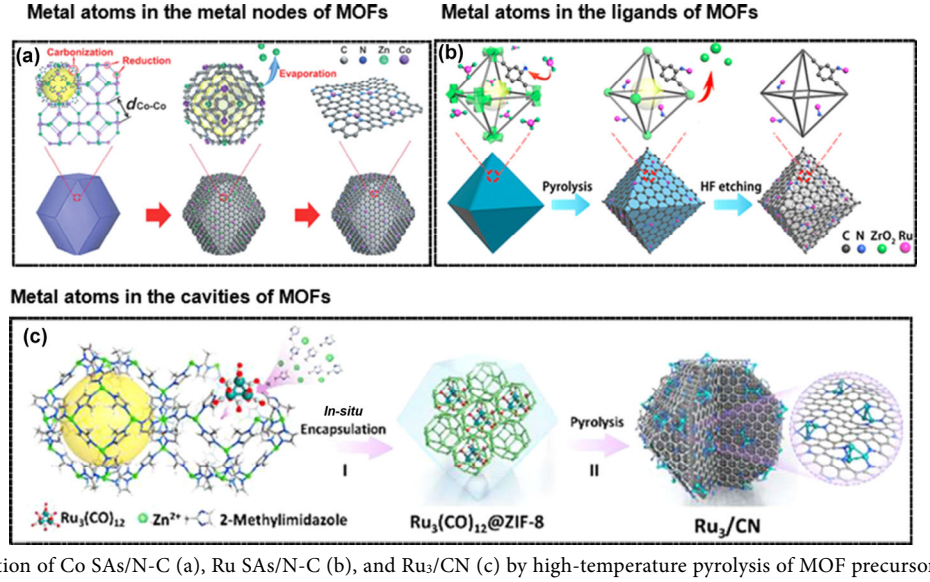

Figure 2 The formation of Co SAs/N-C (a), Ru SAs/N-C (b), and Ru_3/CN (c) by high-temperature pyrolysis of MOF precursors with Co residing in their nodes, Ru residing in their ligands, and Ru residing in their cavities, respectively. (a) Reproduced with permission from Ref. [70], © Wiley-VCH VerlagGmbH &Co. KGaA, Weinheim 2016. (b) Reproduced with permission from Ref. [71], © American Chemical Society 2017. (c) Reproduced with permission from Ref. [72], © American Chemical Society 2017.

as powerful morphology characterization techniques have been commonly employed to identify micro/nano-scale structures. Nevertheless, their resolutions are restricted by the magnetic lens aberration, which cannot make atomic sites characterized. In order to increase the resolution to Å levels, an aberration-corrected STEM (AC-STEM) technique was used to observe directly the distribution of isolated metal atoms on supports [80, 81]. By a combination of both high-angle annular dark-field (HAADF) detector and AC-STEM, AC-HAADF-STEM has been extensively developed to discern single metal atoms [82]. In AC-HAADF-STEM images, the metal atoms with higher atomic number are observed as brighter spots, which can help to identify whether metal nanoparticles/nanoclusters exist on the supporting materials, and even provide a fundamental guide to understand the relation of structure-property for SACs. In a study reported by Wu and co-workers, it was observed by AC-HAADF-STEM that the bright spots were evenly dispersed, which can be assigned to the single Co atoms (Fig. 3(a)) [83]. Furthermore, the electron energy loss spectroscopy (EELS) coupled with AC-HAADF-STEM was used to reveal the composition of single active sites, and the characterization results indicated that the isolated Co centers were coordinated with N atoms, forming atomic Co-N_x sites in the 20Co-NC-1100 catalyst (Figs. 3(b) and 3(c)).

For the identification of isolated metal sites, scanning tunneling microscopy (STM) and *in situ* environmental TEM (ETEM) can be viewed as useful microscopy characterizations. Both STM and *in situ* ETEM technologies have currently been developed to obtain atomic resolution. Using a low-temperature STM characterization technique, Bao et al. acquired atomic-resolution microscopic images of single FeN_4 sites [65]. The dynamic process of single metal atoms can be well monitored by *in situ* ETEM, which is conducive to the understanding of catalytic mechanisms and design of more efficient SACs [78]. Moreover, some spectroscopy characterizations (Fourier-transform infrared spectroscopy, X-ray absorption spectroscopy, etc.) can be used as complementary tools to identify isolated metal atoms. For example, extended X-ray absorption fine structure (EXAFS) is usually used to determine whether metal-metal bonds occur in SACs, which depends on the scattering interaction between photoelectrons and neighboring atoms [43].

2.2.2 *Techniques for the analysis of structural and electronic properties*

In the terms of atomic-scale structural and electronic properties, nuclear magnetic resonance (NMR) and electron paramagnetic resonance (EPR) spectroscopies can be used to determine the chemical coordination and oxidation state of various elements in SACs [43, 84]. Specifically, using an *in situ* NMR technique, the dynamic process of binding ligands is detected, contributing to a better understanding of the relation between structure and performance [44, 85]. However, their employments are limited. NMR is suitable to characterize the SACs with high elemental loadings, and EPR is only applicable for paramagnetic materials. In most cases, the discrimination of different Fe species can be well realized by Mössbauer spectroscopy. As shown in Fig. 4(a), the ^{57}Fe Mössbauer spectra of both Fe-N-C-600 and Fe-N-C-700 were well fitted with three doublets, while two doublets, one singlet, and one sextet were observed in the spectrum of Fe-N-C-800 [86]. These results indicated that isolated Fe atoms were exclusively dispersed in the Fe-N-C-600 and Fe-N-C-700 samples, and there were γ-Fe and Fe_xC species in Fe-N-C-800. Moreover, X-ray photoelectron spectroscopy (XPS) has been used to gain the surface structure of SACs. For instance, the oxidation state of single metal atoms can be revealed by a shift in binding energy [43].

X-ray absorption spectroscopy (XAS) is generally accepted as a powerful technique to provide the structural and electronic information of active moieties at the atomic scale, including extended X-ray absorption fine structure (EXAFS) and X-ray absorption near edge structure (XANES). By EXAFS analysis, some valuable information on the coordination environment of single metal centers is acquired, such as coordination atoms and numbers, and bond lengths. Wu et al. synthesized three single-atom Co samples by high-temperature pyrolysis (800, 900 and 1,000 °C), displaying standout performance for CO_2 reduction [87]. As shown in Fig. 4(b), a single prominent peak at 1.4 Å was derived from the Co-N contribution, corroborating the atomic dispersion of Co species. Notedly, the intensity of Co-N peaks was weakened with increasing pyrolysis temperature, suggesting that N coordination numbers of the single Co centers decreased as the pyrolysis temperatures increased (Fig. 4(b)).

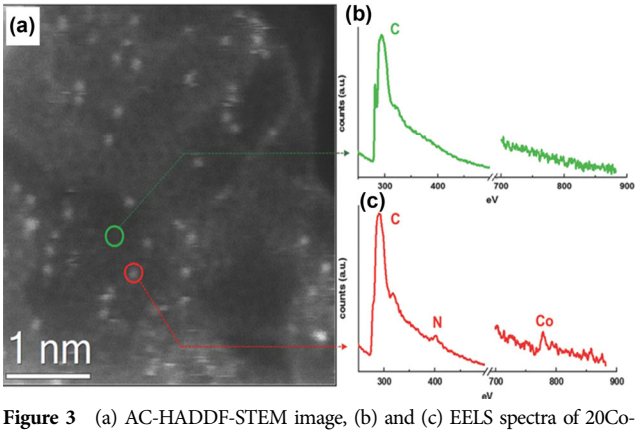

Figure 3 (a) AC-HADDF-STEM image, (b) and (c) EELS spectra of 20Co-NC-1100. Reproduced with permission from Ref. [83], © WILEY-VCH Verlag GmbH & Co. KGaA, Weinheim 2018.

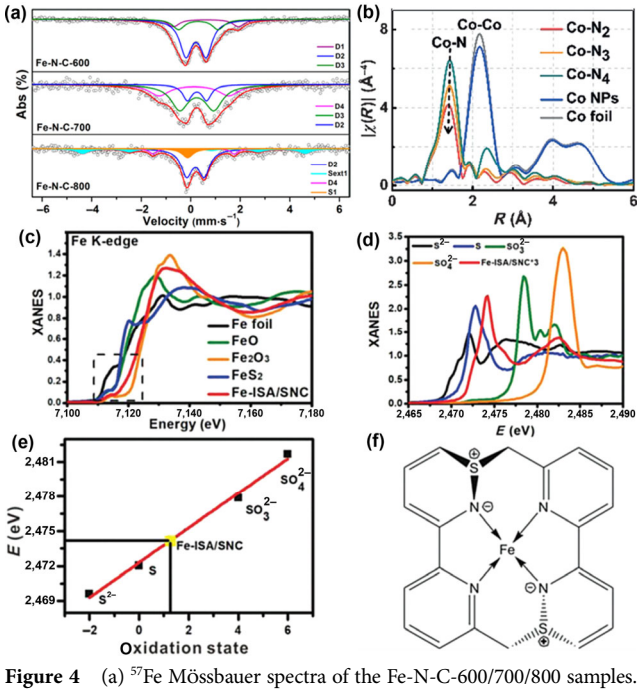

Figure 4 (a) ^{57}Fe Mössbauer spectra of the Fe-N-C-600/700/800 samples. (b) EXAFS analysis of Co-N_x species. (c) and (d) Fe K-edge XANES spectra and S K-edge XANES spectra, respectively, for Fe-ISA/SNC and reference samples. (e) The corresponding linear fitting curve of Fe-ISA/SNC. (f) Molecular configuration of the FeN_4S_2 active site in Fe-ISA/SNC. (a) Reproduced with permission from Ref. [86], © American Chemical Society 2017. (b) Reproduced with permission from Ref. [87], © WILEY-VCH Verlag GmbH &Co. KGaA, Weinheim 2018. (c)–(f) Reproduced with permission from Ref. [88], © WILEY-VCH Verlag GmbH & Co. KGaA, Weinheim 2018.

The EXAFS fitting results revealed that the Co-N coordination numbers were 4.1, 3.1, and 2.2, respectively, under the pyrolysis temperature of 800, 900, and 1,000 °C. Additionally, the analysis of XANES is more complex than that of EXAFS, which can be attributed to the multiple scattering from both many-body effect and polarization effect. The XANES characterization is highly sensitive to the oxidation state of probed atoms, and corresponding fitting is subtle to different structure models. Li et al. reported that single Fe sites supported on S, N co-doped carbon (Fe-ISA/SNC) were favorable for oxygen reduction reaction (ORR) [88]. By XANES analysis, it was found that the Fe valence was between +2 and +3, and the S valence was determined to be +1.2 (Figs. 4(c)–4(e)). Furthermore, the FeN_4S_2 active sites in Fe-ISA/SNC were revealed by the combination of XANES with EXAFS, and the detailed structure of FeN_4S_2 was shown in Fig. 4(f).

3 Applications of SACs in various fields

In the density of states (DOS) of a single-atom catalyst, the band narrowing and discrete energy levels usually occur. The changes of band and energy level are attributed to the ineffective electron density mixing of single atom and substrate, which can regulate the adsorbate bonding on the basis of the electronegativity and valence electron of adsorbates [89–91]. For SACs, metal sites are isolated on the support. As a result, SACs could reach a high activity plateau due to the maximized atom utilization and unique properties [13]. In the process of certain catalytic reactions, SACs show more excellent catalytic performance than their nanoparticle/cluster counterparts. Moreover, a strong interaction between single metal atoms and support leads to impressive chemical stability, which is of benefit to the practical applications of SACs. In the terms of coordination chemistry, the supports of SACs can exist as rigid ligands to coordinate with single metal atoms [92]. The unique coordination environments of single-site metals can tune their geometric and electronic structures, further affecting the physicochemical properties of SACs. Also, it is well known that SACs can be regarded as a bridge between homogeneous and heterogeneous catalysts. Therefore, the research on SACs could interlace with various fields including homogeneous catalysis, heterogeneous catalysis, and coordination chemistry. Furthermore, the characteristic of well-defined sites is a great advantage of SACs as compared to the metal nanoparticles/clusters, which might provide an ideal platform to deepen the atomic-scale insight into catalytic mechanisms.

In this review, the catalytic potentials of SACs in organic synthesis, environmental remediation, energy conversion, and biomedicine have been discussed in detail. It is well known that the activity, selectivity, and stability of catalysts are pivotal parameters to evaluate the catalytic performance in a specific reaction system. In the terms of activity/selectivity, the conversion rate, production/yield rate, Faradaic efficiency, degradation efficiency, detection limitation, overpotential/onset potential/half-wave potential etc. have been used to evaluate the catalytic ability of SACs toward certain reactions.

3.1 Organic synthesis

3.1.1 *Hydrogenation reaction*

Hydrogenation of unsaturated organics is regarded as a very significant transformation in the chemical industry, where SACs can help to lower the activation energy [23, 93–96]. With the catalysis of SACs, the selective hydrogenation reactions of different substrates including nitroarenes, alkenes, alkynes, carbonyl compounds, etc. can be facilitated, by which important raw materials can be manufactured for fine chemicals (such as pharmaceuticals, dyes, perfumes, rubbers and so on) [22]. In the last few years, SACs have been extensively used in the production of diverse anilines from nitroarene hydrogenations. For the hydrogenation of nitroarenes, atomically dispersed Co-, Pd-, Ir-, Pt-, Au-based materials exhibited prominent chemoselectivity to anilines. For instance, Wei et al. found that the positively charged single-atom Pt on FeO_x can favorably hydrogenate functionalized nitroarenes to anilines, exhibiting a high chemoselectivity of 98.6% [95]. They further introduced alkalis to regulate the electronic structure of single-atom Pt centers, and found that Pt loading can reach 2.16 wt.% [97]. As a result, the Pt-O-Na-O-Fe active sites can be formed, on which the chemoselectivity of 97.4% to anilines was achieved. In addition to the FeO_x support, carbon onion graphitic shell was also used to capture single Pt atoms for the chemoselective hydrogenation of nitroarenes [98]. The Pt_1@C catalyst fabricated by "arc discharge in liquid" strategy displayed excellent catalytic performance for the hydrogenation of 1-chloro-4-nitrobenzene, keeping a high chemoselectivity of > 99% over 10 cycles, which was much higher than that on Pt nanoparticles. In the terms of non-noble metals, Co has been frequently selected as the metal sites to prepare SACs for hydrogenation reactions. Gascon and co-workers fabricated an atomically dispersed Co-based catalyst (Co@mesoNC) with the metal loading of 3.5 wt.%, which was favorable for the hydrogenation of nitroarenes to corresponding anilines [99]. During the nitrobenzene hydrogenation process, high activity and chemoselectivity (> 99%) on Co@mesoNC were achieved. The superior catalytic performance can be attributed to the formation of Co-N_x active sites in mesoporous structures. Beside functional anilines, aromatic azo compounds are sometimes desired from nitroarene hydrogenations, which show wide applications in the synthesis of organic colorants [100–102]. For instance, it was demonstrated that both electron-rich and electron-deficient nitroarenes can be selectively converted into substituted azo compounds with the catalysis of Co-N-C [102]. As for the catalytic mechanism of nitroarene hydrogenation on SACs, it was concluded from theoretical calculations that the oxygen vacancies on supports or the basicity of supports were favorable for adsorbing the nitro group, and hydrogen molecules were easily activated on the positively charged single-atom metal centers [103]. At the interface between isolated metal atoms and supports, nitroarenes can be hydrogenated to form functional products via different reaction routes, of which a direct nitro-nitroso-hydroxylamine-aniline path was preferentially favored due to the effect of steric hindrance [104].

SACs, with unique geometric and electronic structures, are not only employed in the hydrogenation of nitroarenes, but also extensively applied in the hydrogenation of alkenes and alkynes. Lu and co-workers reported that 100% butene selectivity, 95% conversion and outstanding durability for 1,3-butadiene hydrogenation can be realized on an atomic Pd_1/graphene catalyst [105]. This research may provide more chances for the fabrication of efficient and robust carbon-based SACs in hydrogenation reactions. Single-atom Pd anchored by mesoporous polymeric graphitic carbon nitride ([Pd]mpg-C_3N_4) has been reported to exhibit high activity and selectivity (~ 100%) to 1-hexene for the 1-hexyne hydrogenation reaction [106]. Furthermore, there was no obvious decay of activity and selectivity within 20 h. By density functional theory (DFT) calculations, it was revealed that the hydrogen molecule was dissociated in a heterolytic path for the [Pd]mpg-C_3N_4-catalyzed alkyne hydrogenation reaction, in which one H atom was bonded to a N atom of mpg-C_3N_4 and another one was bonded to a Pd atom. As a consequence, the alkenes were readily desorbed,

which cannot be further over-hydrogenated or oligomerized. As for the hydrogenation reaction mechanism, most studies proposed that H_2 was dissociated on SACs in a heterolytic way, which is different from the homolytic dissociation of hydrogen over metal nanoparticles [96, 107, 108]. In the hydrogenation reactions catalyzed by SACs, H^+ and H^- species can be formed on supports and single-atom metal centers, respectively, boosting chemoselective hydrogenations [109, 110].

Moreover, Zheng and co-workers used a photochemical approach to fabricate single-atom Pd supported on ethylene glycolate (EG)-stabilized TiO_2 nanosheets (Pd_1/TiO_2-EG), where heterolytic dissociation of H_2 existed in C=C and C=O hydrogenation reactions, leaving H^+ bonded to an adjacent O atom of EG and H^- to a Pd atom [107]. Zhang and co-workers fabricated single/pseudo-single Pt atoms on mesoporous WO_x (Pt/WO_x) for glycerol hydrogenation reaction [108]. The heterolytic dissociation way of H_2 was also demonstrated in the Pt/WO_x-catalyzed hydrogenation reaction, in which H^+ and H^- species can be bonded to the W atoms and isolated Pd atoms, respectively. With the catalysis of Pt/WO_x, the 1,3-propanediol product can be smoothly converted from glycerol. Furthermore, it was found that the H_2 heterolytic dissociation process can be facilitated by introducing isolated Au atoms into the Pt/WO_x catalytic system, further improving the activity and 1,3-propanediol selectivity for glycerol hydrogenation [109]. The enhanced catalytic performance may be ascribed to the electronic regulation of active sites. The acetone hydrogenation on atomically dispersed Ru sites was reported by Qin et al. [111]. In the presence of alkali cations, single Ru atoms supported on Al_2O_3 can effectively catalyze the hydrogenation of acetone to isopropanol. The alkali cations were capable of stabilizing the negatively charged intermediates, thus facilitating the heterolytic dissociation of H_2 for acetone hydrogenation.

In addition, atomically dispersed non-precious metal sites have been reported in the hydrogenation of various organics. Sun et al. revealed that single-atom Co supported on MoS_2 (Co-^{S}MoS_2) was highly active and stable for 4-methylphenol hydrogenation, with a high toluene selectivity of 98.4% [112]. Compared to pure MoS_2, the Co-^{S}MoS_2 catalyst exhibited enhanced performance for the hydrogenation of 4-methylphenol to toluene, which can be ascribed to the formation of S-vacancies. Moreover, Li and co-workers reported that the energy barrier of quinoline hydrogenation can be significantly lowered on N-coordinated single-atom Cu catalyst (Cu_1/CN), showing a superior selectivity (99%) of 1,2,3,4-tetrahydroquinoline [113]. By contrast, the Cu nanoparticle counterpart showed very poor activity under the same conditions. The improved catalytic activity of SA Cu was realized by the coordination of pyrrolic-N rather than pyridinic-N. Furthermore, single-atom alloy (SAA) catalysts have been explored in hydrogenation reactions, such Pd-Cu [51]. In the Pd-Cu catalysts, the active Pd centers can be totally isolated by ambient less active Cu atoms, which was conducive to promoting the dissociation of H_2 on single-atom Pd sites, lowering the binding energy of intermediates by spillover to the less active Cu atoms.

3.1.2 *Oxidation reaction*

Selective oxidation reaction is an important chemical process to produce oxygenated chemicals in organic synthesis [114]. To date, a number of SACs have been fabricated for the catalytic oxidation of organic compounds, such as alcohols, aldehydes, ethers, hydrocarbons, silanes and so on. Early in 2007, Lee and co-workers reported that single-site Pd supported on mesoporous alumina (Pd/meso-Al_2O_3) was capable of facilitating the aerobic oxidation of allylic alcohols (cinnamyl alcohol, crotyl alcohol, and benzyl alcohol), giving turnover frequency (TOF) of 4,096–7,080 h^{-1} and aldehyde selectivity of > 91% [115]. It was demonstrated that the Pd/meso-Al_2O_3 catalyst with 0.03 wt.% Pd loading exhibited high alcohol conversion and aldehyde selectivity, where atomically dispersed Pd^{II} centers were viewed as active sites for the oxidation reactions (as revealed from atomic characterizations). After a few days, the oxidation performance of allylic alcohols over Pd/meso-Al_2O_3 was unchanged, which can be assigned to the stable single-atom Pd^{II} centers as reflected in operando EXAFS spectra. Tsukuda and co-workers revealed that single-atom Pd embedded into carbon nanotubes (CNTs) anchored Au_{25} clusters (Pd_1Au_{24}/CNT) can significantly promote the oxidation of benzyl alcohol, exhibiting improved conversion (74%) and benzoic acid yield (53%) [116]. It was verified for the first time that the doping of single metal atoms had a positive effect on the catalytic performance of metal cluster catalysts in oxidative reactions. The enhanced performance on Pd_1Au_{24}/CNT may be attributed to the modulation of electronic structure of Au sites. The superior selectivity to benzaldehyde on single Au sites has been discovered for benzyl alcohol oxidation [117]. As reported by Li and co-workers, single Au atoms on CeO_2 (Au_1/CeO_2) were capable of catalyzing the selective oxidation of benzyl alcohol to produce benzaldehyde. As compared to Au/CeO_2 nanoparticles, the atomic Au_1/CeO_2 catalyst exhibited higher benzaldehyde selectivity (~ 93%) and stability during the oxidative process. The maximization of interfacial sites can lead to the enhanced catalytic performance, by which a foundation for developing high-performance SACs in other oxidative reactions was established. In addition to noble-metal-based SACs, in the terms of alcohols oxidation, atomically dispersed earth-abundant non-noble metal SACs have been extensively developed. For the selective oxidation of benzyl alcohol to benzaldehyde, an atomically dispersed Cu-N-C catalyst has been demonstrated to be active and stable, which can be ascribed to the fast β-H elimination [118]. Furthermore, atomic Co-N-C samples showed excellent catalytic performance in alcohol oxidation reactions. Guan's group synthesized successfully single-atom Co supported on N-doped graphene (Co-NG-T) by the pyrolysis method [119]. In the resultant sample Co-NG-750, it can be observed that there was a sheet-like structure modified with atomically dispersed Co (Figs. 5(a)–5(d)). The experimental results showed that the Co-NG-750 catalyst exhibited superior catalytic performance for the selective oxidation of a wide range of alcohols including benzyl alcohol, 4-chloro-benzyl alcohol, 4-hydroxy-benzyl alcohol, etc. Especially, high benzyl alcohol conversion of 94.8% and benzaldehyde selectivity of 97.5% can be achieved on Co-NG-750. During the benzyl alcohol oxidation process, high stability of Co-NG-750 was demonstrated as shown in Figs. 5(e) and 5(f). Yu et al. fabricated an atomically dispersed Co-N-C catalyst for the oxidation of benzyl alcohol to benzaldehyde, where there was competitive adsorption of both benzyl alcohol (BA) and O_2 on CoN_4 (Figs. 5(g) and 5(h)) [120]. It was revealed by kinetic experiments and DFT calculations that the access of dioxygen to Co-N_4 sites would be hindered by the strong interaction between BA and Co-N_4, while the adsorption of BA on Co-N_4-O was favored (Figs. 5(i)–5(k)). Additionally, the oxidation of aldehydes and ethers on SACs has also been reported. For instance, single-atom Ag anchored by hollandite manganese oxide (HMO) showed excellent catalytic activity for formaldehyde oxidation at low temperatures, resulting from the strong electronic interaction between Ag and HMO [121]. Wu and co-workers constructed successfully Cu ionic single atoms (ISAs) embedded into the pore of an anionic porphyrinic framework (CZJ-22) by the cation exchange process [122]. The experimental results showed that the obtained CZJ-22-Cu sample can effectively and

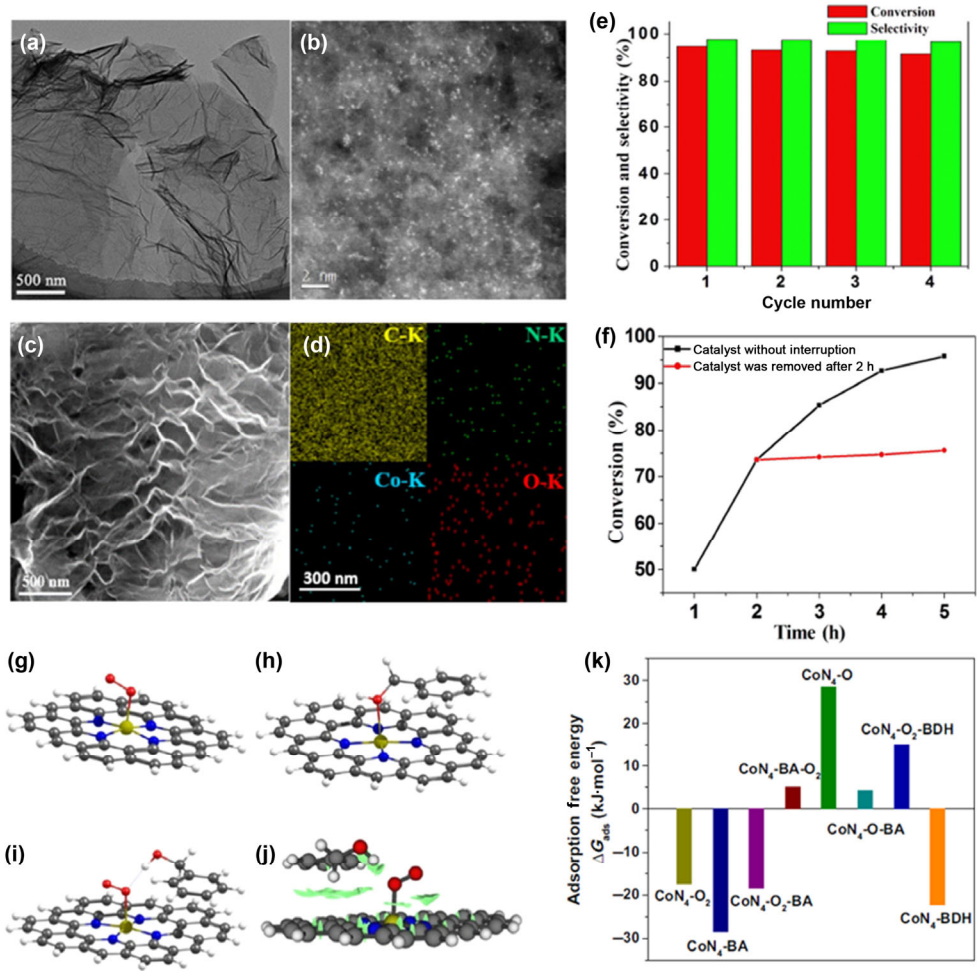

Figure 5 (a)–(d) Representative TEM, HADDF-STEM, SEM, and the corresponding EDX mapping images of Co-NG-750. (e) and (f) Reusability tests and leaching experiments of Co-NG-750 in the aerobic oxidation of benzyl alcohol. (g)–(i) Optimized geometric structures of CoN_4 sites with different adsorbates: CoN_4-O_2, CoN_4-BA, and CoN_4-O_2-BA. (j) The π-π stacking interaction of CoN_4-O_2-BA visualized using Multiwfn software. (k) The adsorption free energies of various adsorbates on CoN_4. (a)–(f) Reproduced with permission from Ref. [119], © Elsevier B.V. 2017. (g)–(k) Reproduced with permission from Ref. [120], © Elsevier Inc. 2019.

stably catalyze the oxidation of ethers to esters, originating from the special structure of CZJ-22-Cu. The Cu-ISAs suspended on anionic pores were almost completely available at the coordination site, which can increase the number of dangling bonds and empty d orbitals, further maximizing the surface free energy of oxygen activation.

Additionally, the selective oxidation of C–H bonds in hydrocarbons is vital but keeps challenging due to high C–H dissociation energy and over-oxidation byproduct formation [123]. Bao and co-workers adopted a ball milling strategy to fabricate atomically dispersed FeN_4 sites on graphene nanosheets (FeN_4/GN), on which the benzene conversion of 23.4% and phenol yield of 18.7% were achieved [65]. In the presence of H_2O_2, the formation of Fe=O intermediates was revealed as a crucial step to promote the selective oxidation of benzene to phenol. Li et al. used a core-shell synthesis method to prepare various single metal atoms on CN materials (SA-M/CN), among which the SA-Fe/CN sample was active and stable for the selective oxidation of benzene to phenol [69]. For the SA-Fe/CN-catalyzed benzene oxidation reaction, the benzene conversion of 45% and selectivity of 94% toward phenol can be realized. In the presence of H_2O_2, it was found that the overall reaction barrier on SA-Fe/CN was significantly reduced as compared to that on Fe nanoparticles/CN. With the catalysis of SA-Fe/CN, two hydroxyls (2HO*) dissociated from H_2O_2 were adsorbed on single Fe sites, which then readily combined to release a H_2O molecule to further form the active oxygen species (O*), with a small barrier of 0.79 eV. The formed O* can well oxidize the benzene to phenol, during which the barrier of 1.08 eV was required to overcome. On Fe nanoparticles/CN, the two hydroxyls were highly difficult to form active oxygen species, and the next reaction barrier of benzene oxidation was as high as 1.73 eV. Different from Fe-N_4, the medium-spin $Fe^{III}N_5$ site was highly favored for C–H oxidation as reported by Zhang et al. [86]. The resultant Fe–N–C catalysts prepared by pyrolysis can effectively catalyze the oxidation of aromatic, heterocyclic, and aliphatic alkanes at the room temperature, whose concentration ratio of each FeN_x species was greatly influenced by the pyrolysis temperature. In the terms of Fe-N_x sites, the medium-spin $Fe^{III}N_5$ in Fe–N–C showed much higher catalytic activity than $Fe^{III}N_6$ and $Fe^{II}N_4$, on which a possible mechanism was suggested in Fig. 6(a). On $Fe^{III}N_5$ sites, the adsorption and activation of TBHP occurred by the interaction between distant oxygen in TBHP and central Fe^{III} as well as the hydrogen bonding between both N and H atoms, along with the production of both tert-butyl oxygen radical (t-BuO•) and hydroxyl radical (•OH) via homolytic cleavage (step 1). Simultaneously, there was an ethylbenzene adsorption on the N/O-groups next to Fe-N_x sites (step 2). The t-BuO• then captured an α-H of ethylbenzene to form α-ethylbenzene radical, further reacting with •OH to obtain 1-phenylethyl alcohol (steps 3 and 4). Whereafter, the H of hydroxyl group in 1-phenylethyl alcohol can be abstracted by t-BuO•, thereby forming 1-ethylbenzene oxygen radical (step 5). By

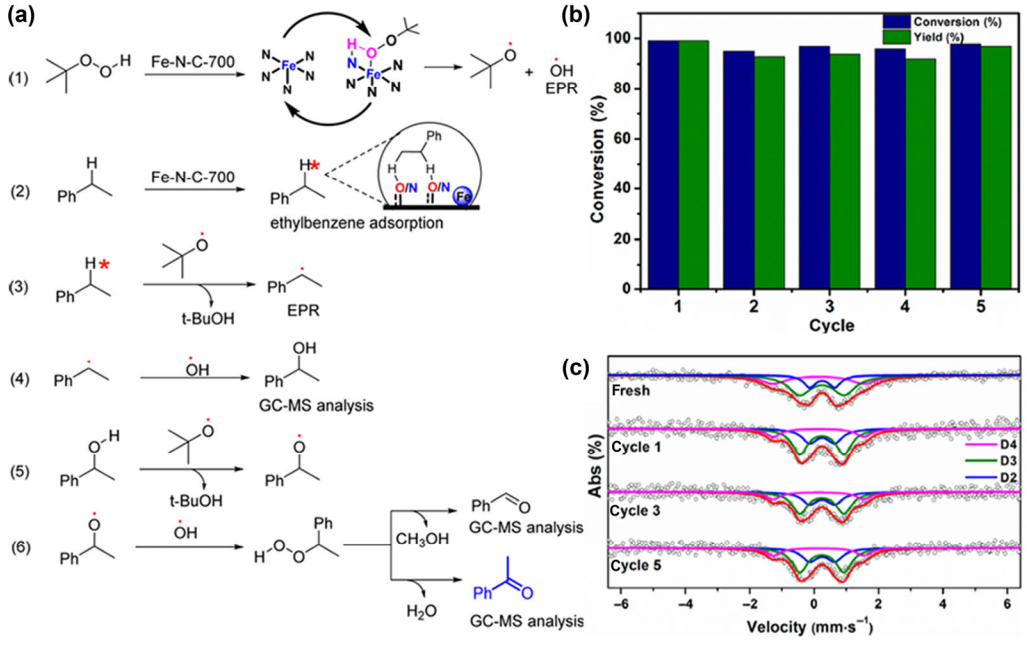

Figure 6 (a) Proposed reaction mechanism of ethylbenzene oxidation on the Fe-N-C-700 catalyst. (b) Reusability of the Fe-N-C-700 catalyst. (c) The ^{57}Fe Mössbauer spectra of Fe-N-C-700 before and after different cycles of reaction. Reproduced with permission from Ref. [86], © American Chemical Society 2017.

a reaction of 1-ethylbenzene oxygen radical with •OH, 1-hydroperoxyethylbenzene was subsequently produced, whose carbonyl-forming elimination can help to generate the desired acetophenone product (step 6). During the whole reaction process, the bond energy of α-H of ethylbenzene was as high as 412 kJ·mol^{-1}, and the step 3 was proposed as a rate-limiting reaction. Impressively, the ethylbenzene conversion and acetophenone selectivity on Fe-N-C-700 can reach ~ 99% after 7 h with the aid of tert-butyl hydroperoxide (TBHP), which can remain stable within 5 cycles (Fig. 6(b)). Furthermore, using Mössbauer spectroscopy characterization, it was disclosed that the Fe-N$_x$ sites in Fe-N-C-700 were unchanged within 5 cycles, indicating good stability of Fe-N-C-700 (Fig. 6(c)). Besides, atomically dispersed Co-N-C catalysts were also reported in the aerobic oxidation of ethylbenzene. For instance, Li and co-workers fabricated a single-atom Co catalyst (Co SAC/CN) with a high Co loading of 23.58 wt.% for the ethylbenzene oxidation, showing high selectivity (97%) and stability [124]. The selective oxidation of silanes toward silanols has attracted attention due to its safety and decreased byproducts (hydrogen gas) [125–127]. Meaningful work about silane oxidation reactions was reported by Chen et al., in which single-atom Au on mesoporous graphitic carbon nitrides (Au/mpg-C_3N_4) showed excellent catalytic activity and stability for the oxidation of silanes with water [128]. During the catalytic process over Au/mpg-C_3N_4, Si-Au(III)-H intermediates were produced from the oxidative insertion of Au^{I} species into Si-H bonds, which were conducive to forming silanols and hydrogen gases.

3.1.3 *C–C coupling reaction*

C–C bonds can be reconstructed via coupling reactions such as Ullmann reaction, Sonogashira coupling reaction, Suzuki cross-coupling reaction, and oxidative coupling reaction, which are very meaningful in organic synthesis [27, 129–131]. Notwithstanding, in recent studies reported for catalytic C–C couplings, the achievement of high selectivity in catalytic systems is still challenging. At the atomic level, some single-atom noble metal catalysts such as Pd SACs exhibited high conversion, selectivity and stability for C–C coupling reactions, which help to boost the production of complicated organics from simple molecules. It was reported that single-atom Pd supported on TiO_2 (Pd_1/TiO_2) was favorable for the Sonogashira coupling reaction, which displayed much higher activity than Pd^{II}-based complexes such as the homogeneous $Pd(PPh_3)_2Cl_2$ catalyst and Pd nanoparticles (Fig. 7(a)) [131]. On the basis of a combination of XPS and XAS characterizations with DFT calculations, it was revealed that an atomic Pd_1O_4 structure in Pd_1/TiO_2 was viewed as the active site for the Sonogashira coupling reaction of iodobenzene with phenylacetylene,

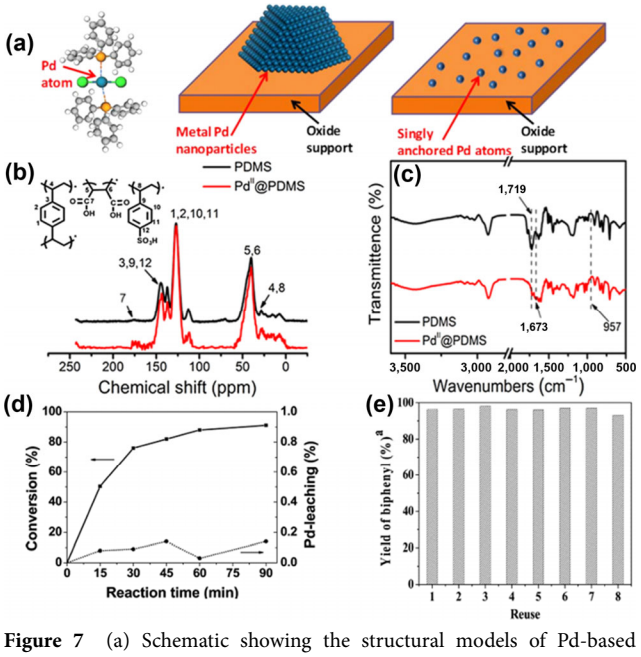

Figure 7 (a) Schematic showing the structural models of Pd-based molecular catalyst $Pd(PPh_3)_2Cl_2$, Pd nanoparticle catalyst and single-atom Pd catalyst (Pd_1/TiO_2). (b) and (c) Solid ^{13}C CP/MAS NMR and FT-IR spectra of PDMS and Pd^{II}@PDMS. (d) Kinetic studies of the Ullmann reaction over Au_4Pd/resin. (e) Recovery and reuse of Au_4Pd/resin for the Ullmann reaction. (a) Reproduced with permission from Ref. [131], © American Chemical Society 2017. (b) and (c) Reproduced with permission from Ref. [133], © Elsevier B.V. 2017. (d) and (e) Reproduced with permission from Ref. [134], © American Chemical Society 2014.

affording a low activation energy of 28.9 kJ·mol^{-1}. Chen et al. demonstrated that single-atom Pd on exfoliated graphitic carbon nitride (Pd-ECN) can effectively and stably catalyze the Suzuki coupling of bromobenzene with phenylboronic acid pinacol ester, on which the macroheterocycle of ECN was conducive to boosting the Suzuki coupling process [132]. As a consequence, 63% conversion and 90% selectivity on Pd-ECN were achieved after 13 h, which were unchanged during the whole catalytic process. The carboxyl acid and sulfonic acid groups of porous organic polymers (POPs) can strongly interact with isolated Pd atoms to generate an atomically dispersed palladium(II)-porous organic polymer catalyst (denoted as Pd^{II}@PDMS) for the oxidative coupling of benzene to biphenyl [133]. In the Pd^{II}@PDMS sample, the double carboxyl acid groups can combine with Pd to form a seven-membered ring structure, while sulfonic acid groups were conducive to improving the electrophilicity of single Pd atoms. From the solid ^{13}C NMR spectra, it was suggested that a similar framework structure was achieved in Pd^{II}@PDMS and PDMS samples (Fig. 7(b)). For Pd^{II}@PDMS, the peak at 1,719 cm^{-1} was weaken, and a new peak occurred at 1,673 cm^{-1} in the Fourier transform infrared (FT-IR) spectrum (Fig. 7(c)), which indicated the COO-Pd^{2+} formation. Experimentally, Pd^{II}@PDMS exhibited a TOF of 352 h^{-1} and biphenyl yield of 26.1% for the oxidative coupling of benzene with dioxygen, which was stable and can be reused. Moreover, Au alloyed single-atom Pd on ion exchange resin (Au-Pd/resin) has also been developed as a promoter for the Ullmann reaction of aryl halides [134]. With the catalysis of Au_4Pd/resin, the biphenyl yield and selectivity were obviously enhanced to 94.5% and 95%, respectively. By the kinetic studies, it was indicated that the reaction rate on Au_4Pd/resin was not influenced by leached Pd content, demonstrating the intrinsically catalytic property of a heterogeneous catalyst (Fig. 7(d)). Moreover, the Au_4Pd/resin catalyst was stable, with an insignificant change of biphenyl yield after recycling for 8 times (Fig. 7(e)). The discovery of Au-Pd/resin was extremely meaningful in the fabrication of other atomically dispersed metal-based catalysts in organic synthesis. In addition to atomic Pd-based catalysts, Pt SACs have also been developed for catalytic C–C couplings. For example, single-atom Pt anchored on thiolated multi-walled nanotubes (Pt-S-MWNT) was active and stable in the Suzuki coupling of 4-iodoanisoles with 4-methylbenzene boronic acid, exhibiting a high reaction yield of 99.5% for 24 h. On Pt-S-MWNT, the reaction yield was finally kept as 82% after 12 cycles. The superior catalytic performance of S-MWNT can be assigned to the highly dispersed Pt atoms on large-surface-area support and fast charge compensation of Pt by S atoms.

In the terms of nonprecious metal SACs, atomically dispersed Co-based materials have been regarded as excellent catalysts to boost the construction of C–C bonds. For instance, Zhang and co-workers found that an atomic Co–N–C catalyst can catalyze the environmentally friendly oxidative cross coupling of primary and secondary alcohols to α,β-unsaturated ketones with yields up to 99% [135]. Furthermore, such catalyst can be recycled with insignificant change of α,β-unsaturated ketone yields. On appropriate catalysts, saturated and α,β-unsaturated ketones can be easily produced by the dehydrogenative and aerobic oxidative coupling of primary and secondary alcohols, respectively (Figs. 8(a) and 8(b)). On the Co–N–C, the possible mechanism for the production of α,β-unsaturated ketones was proposed in Fig. 8(c). Firstly, dioxygen was activated on Co–N–C to generate the superoxide. Followed by a slow abstraction of β-C–H in primary and secondary alcohols, and the corresponding aldehydes and ketones can be produced in the presence of additive LiOH, which was regarded as a rate-determining reaction step. Lastly, the obtained α,β-unsaturated ketones were prepared via the aldol condensation between aldehydes and ketones. The catalytic performance for organic synthesis on various SACs is listed in Table 1.

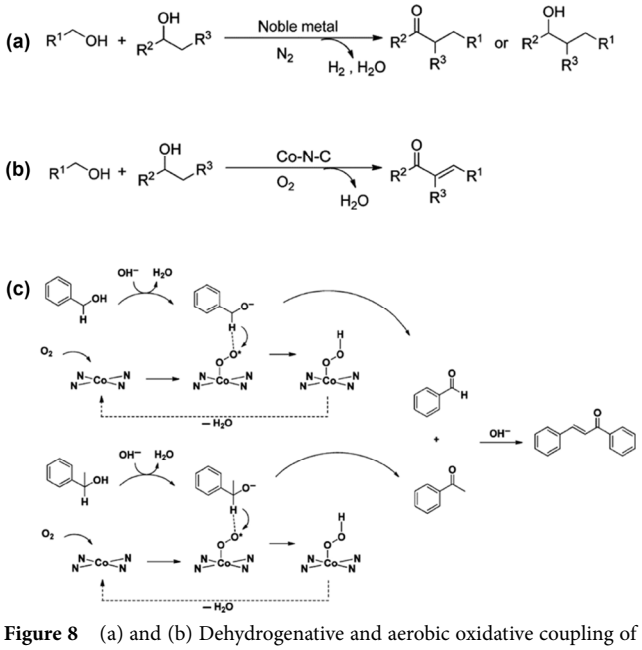

Figure 8 (a) and (b) Dehydrogenative and aerobic oxidative coupling of primary and secondary alcohols. (c) Proposed reaction mechanism of oxidative coupling of primary and secondary alcohols over Co-N-C. Reproduced with permission from Ref. [135], © American Chemical Society 2015.

Table 1 Catalytic organic synthesis performance on SACs

Organic synthesis	SACs	Conversion (%)	Selectivity (%)	Ref.
3-Nitrostyrene hydrogenation	Pt/FeO_x	96.5	98.6 (3-aminostyrene)	[95]
Chloronitrobenzene hydrogenation	Pt_1@C	> 99	> 99 (p-chloroaniline)	[98]
1,3-Butadiene hydrogenation	Pd_1/graphene	95	100 (butene)	[105]
4-Methylphenol hydrogenation	Co-^{S}MoS_2	97.6	98.4 (toluene)	[112]
Quinoline hydrogenation	Cu_1/CN	—	99 (tetrahydroquinoline)	[113]
Benzyl alcohol oxidation	Pd_1Au_{24}/CNT	74	53 (benzoic acid)	[116]
Benzyl alcohol oxidation	Co-NG-750	94.8	97.5 (benzaldehyde)	[119]
Benzene oxidation	FeN_4/GN	23.4	18.7 (phenol)	[65]
Benzene oxidation	SA-Fe/CN	45	94 (phenol)	[69]
Ethylbenzene oxidation	Co SAC/CN	46	97 (acetophenone)	[124]
Suzuki coupling of bromobenzene with phenylboronic acid pinacol ester	Pd-ECN	63	90 (biphenyl)	[132]
Ullmann reaction of aryl halides	Au-Pd/resin	94.5	95 (biphenyl)	[134]

3.2 Environmental remediation

3.2.1 Gas fixation

3.2.1.1 Electrocatalytic and photocatalytic CO_2 reduction

With increasing concerns over environmental issues, the fixation of gaseous contaminations has attracted intensive attention, which is a powerful measure to convert polluted gases into value-added fuels or chemicals [31]. In the past few years, global warming has become more and more serious, mainly originating from the massive emission of carbon dioxide (a kind of greenhouse gas). Hence, it is essential to adopt effective and feasible ways to decrease CO_2 gas in the atmosphere, such as electrocatalytic CO_2 reduction, photocatalytic CO_2 reduction, CO_2 hydrogenation and so on. Currently, the electrocatalysis and photocatalysis of CO_2 reduction are playing important roles in environmental remediation, whose reaction kinetics can be boosted by SACs including atomically dispersed Fe, Co, Ni, Cu, Zn, Sn, Bi, Rh, Pd, Ag, Pt, and Er sites [30, 38, 136–140]. For instance, Wu and co-workers reported that single-atom Co center coordinated with two N atoms (Co-N_2) can electrochemically catalyze the CO_2 reduction reaction (CO_2RR), delivering 94% of Faradaic efficiency at a current density of 18.1 mA·cm^{-2}, and TOF of 18,200 h^{-1} for CO production [87]. They also revealed that the activity can be regulated by tuning coordination environments of catalytic sites, and a low coordination number of Co (Co-N_2) rather than Co-N_4 and Co nanoparticles can boost CO_2 activation. Moreover, Fe-N coordination has also been constructed for CO_2RR. Li and co-workers synthesized an axial Fe-N/CNT electrocatalyst under high-temperature pyrolysis for CO_2RR [141]. DFT calculations showed that the axial Fe-N coordination can lower the free energy of *CO desorption and suppress the HER, thereby exhibiting high CO_2RR activity and CO selectivity. Experimentally, it was demonstrated that the axial Fe-N/CNT catalyst was highly active and stable for CO_2RR, delivering a high CO Faradaic efficiency of 95.47% at –0.6 V vs. RHE. In another study, it was revealed that the edge-hosted M-N_{2+2}-C_8 can be used as active sites for electrochemical CO_2RR [142]. Especially, Fe-N_{2+2}-C_8 displayed high activity and selectivity toward CO during CO_2RR process. Impressively, single-atom Ni supported on N-doped CNTs (Ni/CNTs) was fabricated, which realized high CO Faradaic efficiency (98%), TOF (9,366 h^{-1}), and current density (34.3 mA·cm^{-2}), as well as remarkable stability for electrochemical CO_2RR [143]. The formation of atomically dispersed Ni-N_x active sites for electrochemical CO_2RR accounted for superior CO_2RR performance, as revealed by XAS analysis and DFT calculations. Recently, Zhou et al. found that dual-atom Ag_2/graphene (Ag_2/G) was favorable for electrochemical CO_2RR, where AgN_3-AgN_3 active center has been identified [144]. In comparison with single-atom Ag_1/graphene (Ag_1/G), Ag_2/G showed lower energy barrier of *COOH formation, where intermediates (*COO, *COOH and *CO) were more stable. As a consequence, Ag_2/G can effectively catalyze CO_2RR to produce CO, with high Faradaic efficiency (93.4%), current density (11.87 mA·cm^{-2}), and stability. With the catalysis of SACs, it was also reported that CH_4, C_2H_4, CH_3COCH_3, etc. can be selectively produced from electrochemical CO_2RR. As revealed by Zheng and co-workers, the Cu-N_x moieties of atomically dispersed Cu-N-C catalysts were viewed as dominant active sites for electrochemical CO_2RR [145]. By XAS analysis, it was revealed that single Cu atoms existed in the form of mixed oxidation states, and the Cu-N_x configuration was proposed in Cu-N-C samples (Figs. 9(a)–9(c)). Neighboring Cu-N_2 sites favored the C_2H_4 formation, while isolated Cu-N_4 and Cu-N_2 sites were highly active for the generation of CH_4. Experimental results showed that the as-synthesized Cu-N-C-800 catalyst delivered a C_2H_4 Faradaic efficiency of 24.8%, and the Cu-N-C-900 showed the CH_4 Faradaic efficiency of 38.6%. Single-atom Cu on N-doped porous carbon (Cu-SA/NPC) was reported to display the CH_3COCH_3 Faradaic efficiency of 36.7% and production rate of 336.1 μg·h^{-1} during electrochemical CO_2RR process [146]. In the Cu-SA/NPC catalyst, Cu-pyrrolic-N_4 active sites can lower the reaction energy of CO_2 activation and C–C bond coupling, facilitating CH_3COCH_3 production. Xin et al. found that single-atom Zn on microporous N-doped carbon (SA-Zn/MNC) can effectively catalyze the CO_2 electroreduction to produce CH_4, exhibiting the Faradaic efficiency of 85% (Figs. 9(d) and 9(e)) [147]. The high yield rate of CH_4 (158 ± 4 μmol·h^{-1}·cm^{-2}), low Tafel slope (103 mV·dec^{-1}), and remarkable stability were realized during SA-Zn/MNC-catalyzed CO_2RR (Figs. 9(f)–9(h)). By DFT calculations, the mechanism of CH_4 production on SA-Zn/MNC was studied as shown in Figs. 9(i) and 9(j). Firstly, CO_2 molecules were activated to form *OCHO species, in which the O and H atoms bonded with Zn and C, respectively. Then, the generation of *CHO, *OCH_2, *OCH_3, and *$OHCH_3$ can subsequently arise, where the O atom bonded to Zn. The CH_4 was finally released, while the adsorption of H on *OH led to forming a H_2O molecule. Besides electrochemical CO_2RR, the photocatalysis of CO_2 has been extensively reported. Rare-earth erbium has been selected to fabricate CO_2RR photocatalysts. For example, Wang and co-workers discovered that single-atom Er anchored on carbon nitride nanotubes (Er_1/CNNT) can realize high catalytic efficiency towards solar-driven CO_2 reduction in the pure-water system, displaying CO production rate of 47.1 μmol·g^{-1}·h^{-1} and CH_4 generation rate of 2.5 μmol·g^{-1}·h^{-1} [148]. Combining experimental results and DFT calculations, it was unveiled that Er_1/CNNT was efficient and robust for the CO production, where the introduction of Er atoms can obviously enhance its photocatalytic performance. Ye et al. reported that atomically dispersed Co in the porphyrin-based MOF was able to catalyze CO_2RR, during which the evolution rates of CO and CH_4 reached 200.6 and 36.76 μmol·g^{-1}·h^{-1}, respectively [149]. With the aid of single-atom Co, CO_2 can be easily captured and then reduced into CO and CH_4 products under visible-light illumination. During CO_2RR, the photogenerated electrons migrated from porphyrin to Co centers, supplying long-lived electrons to the adsorption of CO_2 molecules on single-atom Co sites. Theoretical studies predicted that HCOOH was favorably produced on Pd/g-C_3N_4, with a rate-limiting barrier of 0.66 eV for photocatalytic CO_2RR [150]. The stabilization of single-atom Pd on g-C_3N_4 can obviously increase the visible-light absorption, and further facilitate the CO_2 photoreduction.

3.2.1.2 NO removal

As a major factor of photochemical smog, NO gas is produced from industrial and vehicular gaseous emission, which has malign influence on both human health and atmospheric environment [151]. At the atomic level, some studies have focused on the removal of NO, which is of importance for promoting the development of an environmentally friendly society. After light irradiation, NO molecules can be transformed into nitrates over SACs. Fujiwara and Pratsinis discovered that NO was easily adsorbed on isolated Pd centers, and further converted into NO_3^- under artificial solar light (100 mW·cm^{-2}) [152]. From the diffuse reflectance infrared Fourier transform spectroscopy (DRIFTS) spectra of NO adsorption, it can be concluded that both single-atom Pd and Pd clusters coexisted in 1 wt.% Pd/TiO_2, while there were only isolated Pd atoms in

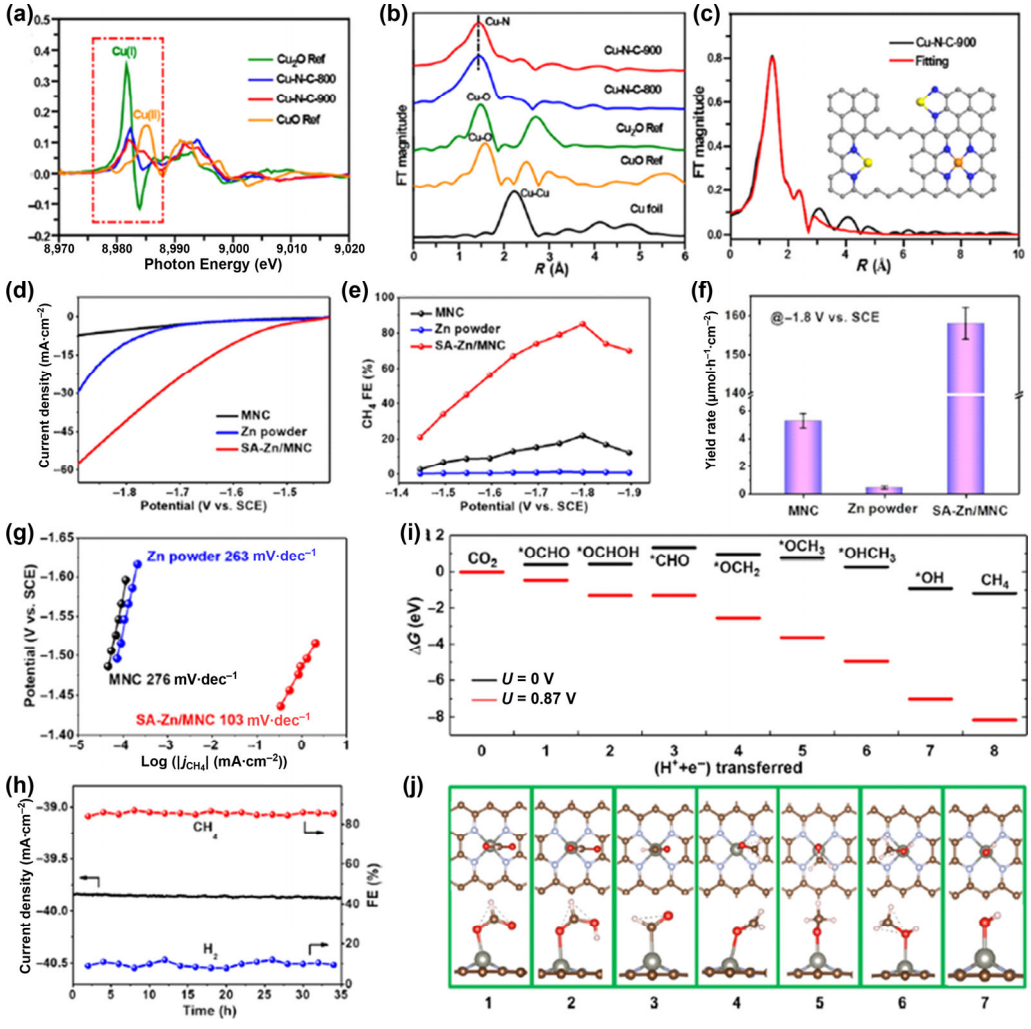

Figure 9 (a) and (b) The first derivatives of XANES region and the FT-EXAFS spectra of Cu-K edge for Cu_2O, CuO, Cu-N-C-800 and Cu-N-C-900 samples. (c) EXAFS *R*-space and corresponding fitting curves of Cu-N-C-900. Inset: illustration for the Cu-N_2 and Cu-N_4 coordination structures. Gray, blue, yellow and orange spheres represent C, N, Cu(I) and Cu(II) elements, respectively. (d) Polarization curves for MNC, Zn powder, and SA-Zn/MNC. (e) Faradaic efficiencies of CH_4 at different applied potentials. (f) and (g) Yield rates and Tafel plots for electrochemical CO_2 reduction to CH_4. (h) Stability of SA-Zn/MNC for electrochemical CO_2 reduction at –1.8 V vs. SCE. (i) Free energy diagrams for electrochemical CO_2 reduction to CH_4 on Zn-N_4-graphene. (j) The most stable structure of each step. The red and pink balls represent O and H atoms, respectively. (a)–(c) Reproduced with permission from Ref. [145], © American Chemical Society 2020. (d)–(j) Reproduced with permission from Ref. [147], © American Chemical Society 2020.

0.1 wt.% Pd/TiO_2 (Fig. 10(a)). After NO removal, the peak of NO adsorption on single-atom Pd kept unchanged, while that on TiO_2 and Pd clusters vanished (Fig. 10(b)). The coverage of TiO_2 and Pd clusters by NO_3^- led to the deactivation, which was responsible for the disappearance of NO adsorption peaks on both TiO_2 and Pd clusters. Before and after NO removal, the Pd subnano-clusters remained unchanged in Pd/TiO_2 (Figs. 10(c) and 10(d)). Single-atom Pt anchored by g-C_3N_4 (Pt-SA-CN) has been demonstrated to be favorable for the light-driven NO removal [153]. Among Pt-SA-CN samples, the as-synthesized $Pt_{0.2}$-SA-CN catalyst displayed the highest photocurrent intensity and NO conversion under visible light, facilitating the oxidation of NO to NO_3^- (Figs. 10(e) and 10(f)). Theoretical calculations found that single-atom Cu anchored by g-C_3N_4 (Cu@g-C_3N_4) was capable of catalyzing the NO electrochemical reduction, with a low limiting potential of 0.371 V vs. RHE [154]. The NO molecules adsorbed on Cu@g-C_3N_4 can be subsequently reduced to ammonia: $NO(g) + 5H^+ + 5e^- \rightarrow NH_3(g) + H_2O(l)$. As for the fixation of more toxic gases, theoretical studies on SACs have been reported. For instance, the strong interaction between isolated metal (Fe, Co) atoms and single vacancy graphene can contribute to the high adsorption activity for toxic gases (CO, NO, NO_2, SO_2, SO_3, H_2S, etc.) [155, 156].

3.2.2 *Pollutant degradation*

In recent years, water pollutants including heavy metals, dyes, pesticides and other organic compounds have greatly threaten human health and even influenced earth's ecosystems, which should be degraded through effective approaches (such as adsorption and photo/electrocatalysis methods) [29, 157, 158]. In order to realize the rapid degradation of contaminations, many studies focus on the exploration of efficient catalytic systems in aqueous environments, where SACs have exhibited great advantages for water remediation [31]. Gates and co-workers investigated a series of single-atom adsorbents to eliminate mercury, and found that atomically dispersed Co-N_3 sites on the single vacancy graphene showed high activity and selectivity for mercury adsorption [29]. This work laid a good foundation to develop high-efficiency SACs for the removal of elemental mercury. Moreover, the emission of organic contaminations is commonly regarded as a major water pollution source, which can be mitigated with the aid of atomically dispersed metal-based catalysts as demonstrated by numerous experiments and theoretical calculations. Owing to surface plasmon resonance (SPR) effect, silver was chosen to construct atomically dispersed Ag-based photocatalysts for degrading

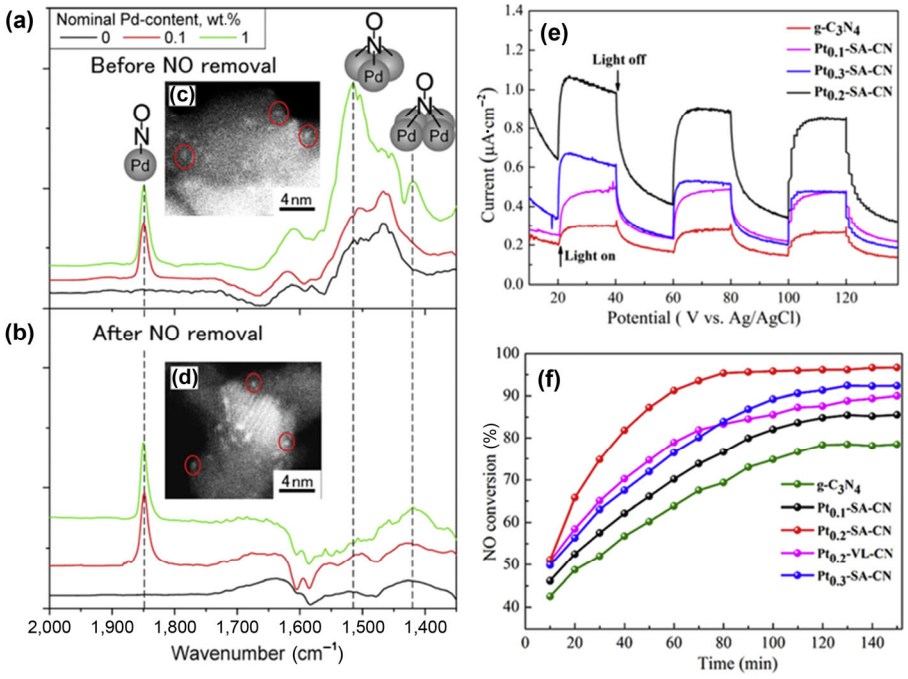

Figure 10 DRIFT spectra of NO (1,000 ppm) adsorption (after 20 min) on Pd/TiO_2 with 0 (black), 0.1 (red) and 1 (green) wt.% Pd before (a) and after NO removal (b). The insets show STEM images of TiO_2 with 1 wt.% Pd before (c) and after NO removal (d). (e) Photocurrent response curves of as-prepared g-C_3N_4, $Pt_{0.1}$-SA-CN, $Pt_{0.2}$-SA-CN and $Pt_{0.3}$-SA-CN catalysts with or without visible-light irradiation. (f) Variations of NO conversion efficiency with irradiation time. (a)–(d) Reproduced with permission from Ref. [152], © Elsevier B.V. 2017. (e) and (f) Reproduced with permission from Ref. [153], © Elsevier B.V. 2017.

contaminants, such as single Ag atoms anchored on the g-C_3N_4 support. Wang et al. reported that single-atom Ag on mesoporous g-C_3N_4 (Ag/mpg-C_3N_4) can be applied in the removal of bisphenol A (BPA) [158]. With 1 mM peroxymonosulfate (PMS), the Ag/mpg-C_3N_4 catalyst with 0.1 g·L^{-1} can realize the BPA degradation efficiency of 100% under visible light for 1 h. During the whole degradation process, sulfate and superoxide radicals as well as photogenerated holes were viewed as main reactive species. Similarly, Liu and co-workers fabricated a single-atom Ag decorated g-C_3N_4 catalyst (AgTCM/UCN), which displayed enhanced degradation activity of sulfamethazine with the addition of PMS [159]. For atomically dispersed Ag on g-C_3N_4, the effective separation of PMS, SPR effect of Ag, and high surface area of g-C_3N_4 were responsible for the high activities of photodegradation reactions. Single Fe atoms anchored on g-C_3N_4 have also been fabricated for the degradation of organic contaminants. In 2018, Guo and co-workers synthesized single-atom Fe on g-C_3N_4 (FeN_x/g-C_3N_4) with a high Fe loading of 18.2 wt.% through one-step pyrolysis (Fig. 11(a)) [160]. The FeN_x/g-C_3N_4 photocatalyst exhibited superior degradation efficiency for methylene blue (MB), methyl orange (MO), rhodamine B (RhB), and phenol, which can be attributed to the formation of Fe(II)-N_x active centers. Moreover, isolated Fe atoms embedded in porous carbon were found to exhibit remarkable removal efficiency for organic water pollutants. Yao and co-workers synthesized an atomically dispersed Fe-based photocatalyst (Fe@COF), where single Fe atoms were confined into the porous carbon from covalent organic framework [161]. In the presence of PMS, the high-density Fe-N_x sites in Fe@COF can efficiently activate PMS to produce singlet oxygen ($^1O_2$), and further contribute to the remarkable photodegradation efficiency (88.6%–100%) of typical organics including malachite green, methyl violet, methylene blue, methyl orange, neutral red, and rhodamine B. Derived from Fe-doped ZIFs, single-atom Fe on N-doped porous carbon (Fe_{SA}-N-C) was synthesized by Zhou and co-workers [162]. In the Fe_{SA}-N-C catalyst, it was observed that atomically dispersed Fe instead of Fe clusters/nanoparticles and N atoms were homogeneously distributed over the whole carbon matrix (Fig. 11(b)). Experimental results showed that Fe_{SA}-N-C displayed high activity and reusability for BPA degradation, where the Fe-N_x moieties were regarded as main active sites for activating PMS. The rate constant (k) of Fe_{SA}-N-C can reach 0.240 min^{-1}, much higher than that of Fe_{NP}-NC (~ 0.0296 min^{-1}). Notedly, high-valent iron-oxo species were generated as major reactive species during the BPA degradation process. In the case of BPA photo-degradation, atomically dispersed Co-N-C catalysts have been fabricated. For instance, an atomic Co-N-C-900 photocatalyst has been confirmed to favor the removal of BPA [163]. The carbon matrix of Co-N-C samples can be characterized by Raman spectroscopy spectra (Fig. 11(c)), and the N_2 adsorption-desorption isotherms indicated that Co-N-C-900 possessed a mesoporous structure, whose BET surface area and total pore volume reached ~ 379.2 $m^2·g^{-1}$ and 0.788 $cm^3·g^{-1}$, respectively (Fig. 11(d)). Combining XRD with XPS, it was revealed that Co species were highly dispersed in Co-N-C-900 (Fig. 11(e)). In the presence of PMS, Co-N-C-900 displayed enhanced degradation performance for the BPA pollutant with a rate constant of 2.81 min^{-1}. In the photocatalytic system, it was also demonstrated that the rapid BPA degradation on Co-N_x was realized via $^1O_2$ reactive species. By means of radical and non-radical reactions, the PMS/Co-N-C system was also applied for the removal of other water contaminants including benzotriazole, diatrizoate, 5-benzoyl-4-hydroxy-2-ethoxybenzenesulfonic acid, and 2,4-dichlorophenol (2,4-DCP) [164]. Besides photo-degradation, electrochemical degradation of organic pollutants has also been developed. It was found that single-atom Co on sulfide graphene (Co-SG) can electrochemically degrade 2,4-dichlorobenzoic acid (2,4-DCBA) [157]. With the catalysis of Co-SG, the concentration of organic pollutants significantly decreased within 30 min, and a high conversion rate of 2,4-DCBA was achieved (Fig. 11(f)). The resulting Cl^- from 2,4-DCBA can be moved to the anodic compartment (Fig. 11(g)). At the cathodic compartment, O_2 molecules were reduced to

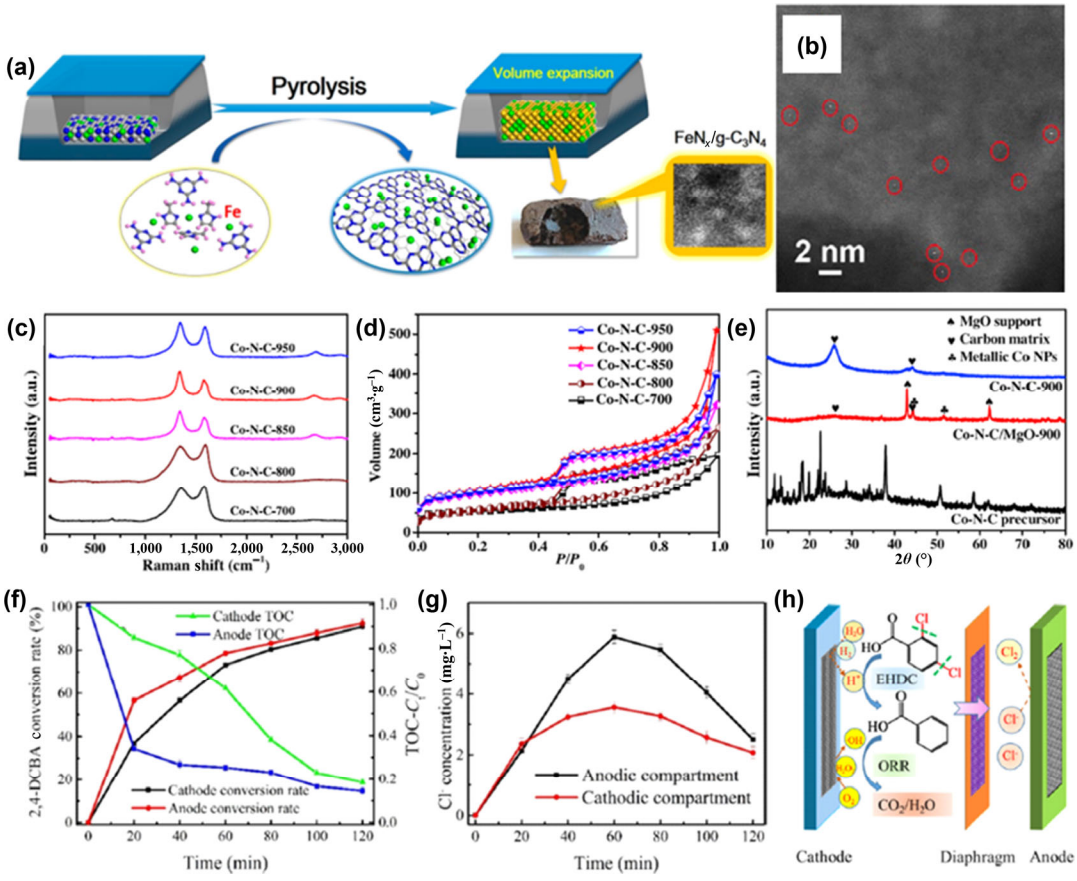

Figure 11 (a) Pyrolytic synthesis of FeN_x/g-C_3N_4 catalysts. (b) HAADF-STEM image of Fe_{SA}-N-C-20. (c) and (d) Raman spectra and N_2 adsorption/desorption isotherms of Co-N-C samples obtained at different calcination temperatures. (e) XRD patterns for Co-N-C precursor, Co-N-C/MgO-900 and Co-N-C-900. (f) Total organic carbon (TOC) concentration ratio and conversion rate of 2, 4-DCBA over time. (g) Change in the Cl^- concentration with time in different polar compartments. (h) Schematic illustration of electrocatalytic reductive dechlorination and degradation of 2, 4-DCBA on Co-SG. (a) Reproduced with permission from Ref. [160], © American Chemical Society 2018. (b) Reproduced with permission from Ref. [162], © Elsevier B.V. 2020. (c)–(e) Reproduced with permission from Ref. [163], © Elsevier B.V. 2019. (f)–(h) Reproduced with permission from Ref. [157], © American Chemical Society 2020.

generate H_2O_2, thereby forming hydroxyl radicals (•OH). The formed ·OH can facilitate the conversion of 2,4-DCBA to benzoic acid (BA) via the hydrodechlorination reaction, while the Cl^- from 2,4-DCBA in anodic compartment was oxidized into Cl_2 (Fig. 11(h)).

Additionally, it is known that volatile organic compounds (VOCs: formaldehyde, benzene, toluene, etc.) can cause great damage to human health, which are usually detected in the indoor air. In the past decade, various strategies have been carried out to remove VOCs, such as thermal catalysis and photocatalysis. According to recent literatures, it has been widely reported that SACs are capable of facilitating the removal of volatile toluene. Experimental results showed that 90% conversion for toluene oxidation was achieved over single-atom Ag modified Mn_2O_3 nanowires at 205 °C, which was quickly reduced to 30% for 2.5 h [165]. The addition of CeO_2 can significantly improve the catalytic stability owing to enhanced oxygen activation capability. It was found that the formed CeO_2-Ag/Mn_2O_3 system (0.63 wt.% CeO_2-0.06 wt.% Ag/Mn_2O_3) displayed only 10% decay of toluene conversion within 50 h, where both Ag and CeO_2 were highly decentralized over the whole Mn_2O_3 surface as observed from Fig. 12. This study indicated that atomically dispersed Ag-based materials would be promising to catalyze the oxidation of VOCs, as the alternatives for precious metal catalysts. In addition, it has been demonstrated that single-atom Pt on MnO_2 was active and stable for toluene oxidation, showing 100% conversion of 0.42 ppm toluene at room temperature [166]. For Pt/MnO_2, the average valence of Mn was determined to be 3.33, indicative of abundant oxygen

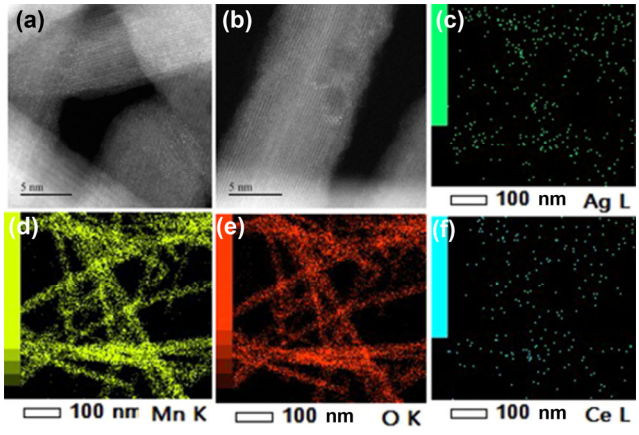

Figure 12 (a)–(f) STEM and EDX images of 0.63 wt.% CeO_2-0.06 wt.% Ag/Mn_2O_3. Reproduced with permission from Ref. [165], © Elsevier B.V. 2019.

vacancies on the surface of MnO_2 (Fig. 13(a)). The elongated Mn-O bonds existed in the Pt/MnO_2 catalyst, implying that the active O atoms were generated (Figs. 13(b) and 13(c)). With the addition of isolated Pt atoms, the surface oxygen species of Pt/MnO_2 can be activated, generating hydroxyl radicals (·OH) and further exhibiting superior performance for the oxidative removal of indoor toluene. Moreover, isolated Pt atoms supported on TiO_2 were constructed for the toluene removal. For example, Zhang and co-workers found that the introduction of single Pt atoms can help to enhance the photocatalytic activity of pristine TiO_2 for toluene oxidation

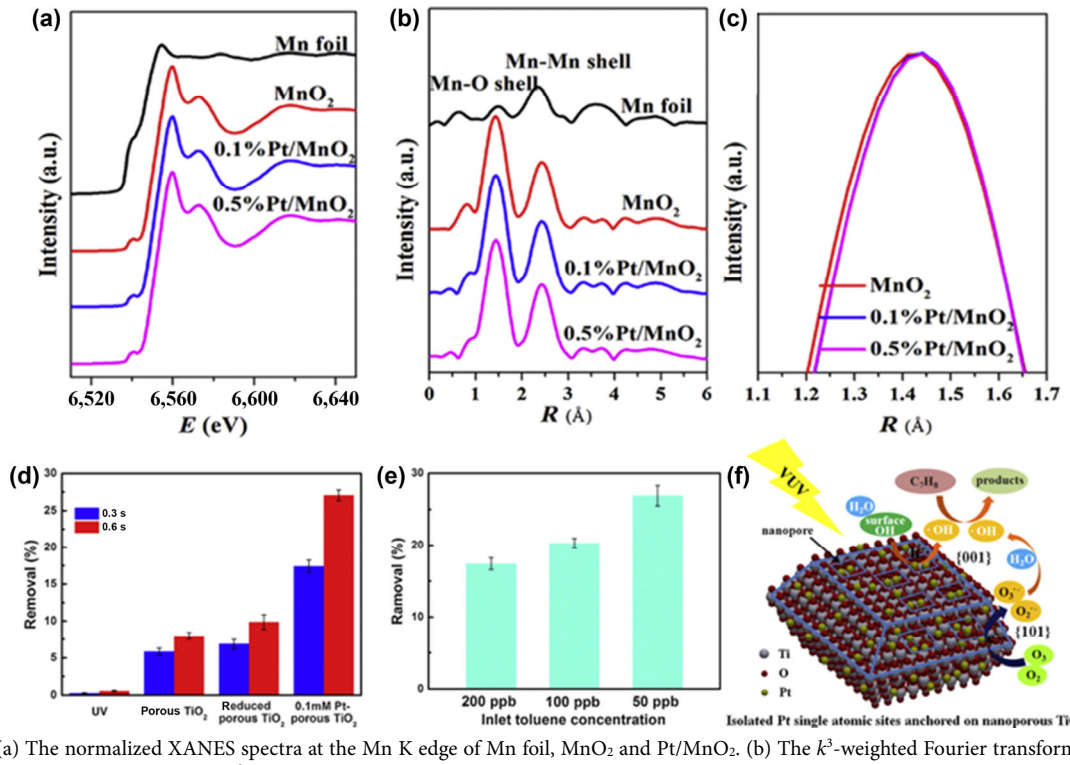

Figure 13 (a) The normalized XANES spectra at the Mn K edge of Mn foil, MnO_2 and Pt/MnO_2. (b) The k^3-weighted Fourier transform spectra of Mn from EXAFS. (c) Magnification of the k^3-weighted Fourier transform spectra of Mn from EXAFS. (d) UV photocatalytic degradation of toluene by the as-prepared samples. (e) UV photocatalytic activity of the as-prepared sample for low concentration toluene. (f) Schematic photocatalytic mechanism for isolated Pt single atomic sites anchored on nanoporous TiO_2 film under VUV irradiation. (a)–(c) Reproduced with permission from Ref. [166], © Elsevier B.V. 2019. (d)–(f) Reproduced with permission from Ref. [167], © Elsevier B.V. 2019.

[167]. Under ultraviolet (UV) light, single-atom Pt decorated porous TiO_2 exhibited photodegradation rates of 17.42% and 27.06% at the residence time of 0.3 and 0.6 s, respectively, for toluene removal (Fig. 13(d)). When the inlet toluene concentration decreased from 200 to 50 ppb, the rate of toluene removal was improved from 17.42% to 26.9% at the residence time of 0.3 s (Fig. 13(e)). Under vacuum ultraviolet (VUV) light, the photodegradation rate of toluene on single-site Pt reached 45.88% at the residence time of 0.3 s. During the VUV photodegradation process, the detailed mechanism was illustrated in Fig. 13(f). By VUV irradiation, both O_3 and O_2 reacted with the trapped photogenerated electrons to generate $O_3^{\bullet-}$ and $O_2^{\bullet-}$, which further reacted with H_2O to form ·OH, thus speeding up the toluene removal over single-atom Pt decorated TiO_2. Using molten salt approach, 0.2 wt.% single-atom Pt supported on TiO_2 (0.2 wt.% Pt/TiO_2) was successfully constructed by Deng and co-workers, where isolated Pt atoms and nanoparticles co-existed [168]. During toluene oxidation process, 12 organics can be produced as shown in Fig. 14(a). It was revealed that the catalytic performance of 0.2 wt.% Pt/TiO_2 was influenced by adding H_2O, CO_2, and SO_2 (Fig. 14(b)). The existence of H_2O suppressed the toluene oxidation, but cannot lead to the poisoning of 0.2 wt.% Pt/TiO_2. Both CO_2 and SO_2 can poison the 0.2 wt.% Pt/TiO_2 catalyst, especially for SO_2 molecules. In the presence of SO_2, the sulfite and sulfate species were formed and further poisoned active sites, which caused that the catalytic performance on 0.2 wt.% Pt/TiO_2 became very poor. The catalytic performance for environmental remediation on various SACs is summarized in Table 2.

3.3 Energy conversion

3.3.1 ORR for PEM fuel cells

Proton exchange membrane fuel cell (PEMFC) has been known as a very promising electrochemical energy conversion technology that can directly convert the hydrogen/oxygen chemical energy into electricity, owing to its simple design, environmental friendliness, high energy density, and conversion efficiency. In typical PEMFCs, ORR at the cathode involves multistep electron transfers and suffers from sluggish kinetics, which significantly lowers the overall cell performances [169]. Therefore, developing high-efficiency electrocatalysts for PEMFCs is urgent in practical applications. To date, Pt-based nanocatalysts have shown remarkable ORR performance, however, the exorbitant cost and scarcity of Pt greatly limit their practical utilization in PEMFCs. Therefore, tremendous efforts have been devoted to downsizing Pt nanoparticles into clusters or even single atoms. In 2017, Liu and co-workers fabricated single-atom Pt on N-doped carbon (Pt_1-N/BP), which favored $4e^-$ ORR in acidic media [170]. It was clearly observed from HAADF-STEM images that isolated Pt atoms were well decentralized over the whole carbon-based substrate for Pt_1-N/BP. Pt nanoparticles were also observed in the Pt_1/BP sample. The doped N in Pt_1-N/BP effectively prevented Pt atoms from aggregating, enhancing the ORR performance. In the acidic Pt_1-N/BP-based fuel cell, a power density of 680 mW·cm^{-2} was achieved, and the current retention of 74% was kept at 0.5 V vs. RHE after 200 h. By theoretical calculations, it was further revealed that the excellent ORR activity and stability of Pt_1-N/BP in acidic fuel cells mainly resulted from the pyridinic-nitrogen-coordinated Pt centers. After then, they also reported that single Pt atoms embedded in carbon defects ($Pt_{1.1}/BP_{defect}$) were highly active and stable for acidic ORR, where Pt-C_4 moieties were viewed as main active sites [171]. From the HAADF-STEM image of $Pt_{1.1}/BP_{defect}$, it was observed that isolated Pt atoms existed in the carbon defects rather than intact carbon surface. Using $Pt_{1.1}/BP_{defect}$ as the cathode catalyst, a proof-of-concept PEMFC was assembled, realizing a maximum power density of 520 mW·cm^{-2}. Shui

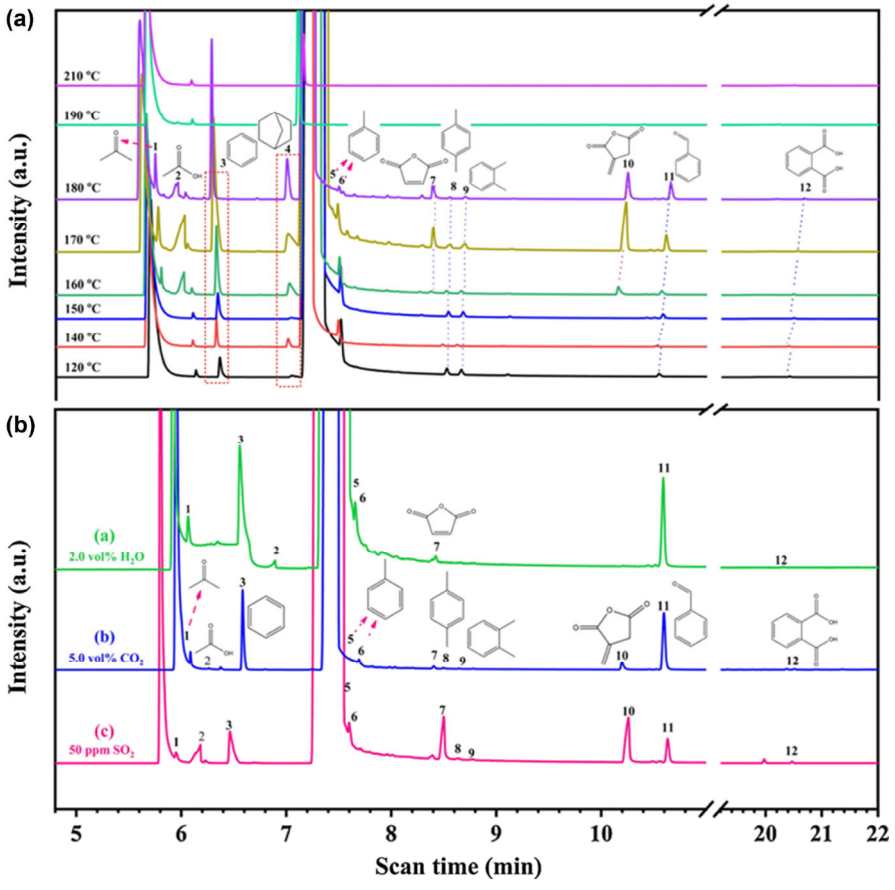

Figure 14 (a) Possible reaction intermediate products detected by GC-MS during the toluene oxidation process over 0.2 wt.% Pt/TiO_2 at different temperature. (b) Possible reaction intermediate products detected by GC-MS during the toluene oxidation process over 0.2 wt.% Pt/TiO_2 in the presence of H_2O, CO_2, and SO_2. Reproduced with permission from Ref. [168], © Elsevier B.V. 2020.

Table 2 Environmental remediation performance on SACs

Environmental remediation	SACs	Faradaic efficiency /Degradation efficiency (%)	Ref.
Electrocatalytic CO_2RR	Fe-N/CNT	95.47 (CO)	[141]
Electrocatalytic CO_2RR	Ni/CNTs	98 (CO)	[143]
Electrocatalytic CO_2RR	Ag_2/G	93.4 (CO)	[144]
Electrocatalytic CO_2RR	SA-Zn/MNC	85 (CH_4)	[147]
Electrocatalytic CO_2RR	Cu-SA/NPC	36.7 (CH_3COCH_3)	[146]
NO photoreduction	Pt-SA-CN	96.2 (NO_3^-)	[153]
Bisphenol A photodegradation	Ag/mpg-C_3N_4	100	[158]
Methylene blue photodegradation	FeN_x/g-C_3N_4	98.9	[160]
Orange II photodegradation	Fe@COF	100	[161]
Electrochemical degradation of 2,4-dichlorobenzoic acid	Co-SG	91.1	[157]
Toluene combustion	Ag/Mn_2O_3	90	[165]
Toluene degradation (at room temperature)	Pt/MnO_2	100	[166]

and co-workers reported that N-coordinated Ir SAC (Ir_1-N/C) exhibited superior electrocatalytic performance for the acidic ORR and PEMFC [172]. In 0.1 M $HClO_4$, Ir_1-N/C delivered high onset potential (E_{onset}, 0.923 V vs. RHE) and half-wave potential ($E_{1/2}$, 0.831 V vs. RHE), as well as small Tafel slope (48 mV·dec^{-1}), which was comparable to the commercial Pt/C (E_{onset}: 0.952 V vs. RHE; $E_{1/2}$: 0.862 V vs. RHE; Tafel slope: 58 mV·dec^{-1}). Moreover, the ORR activity of Ir_1-N/C was much higher than that of Ir/C nanoparticles (E_{onset}: 0.817 V vs. RHE; $E_{1/2}$: 0.824 V vs. RHE; Tafel slope: 112 mV·dec^{-1}). The KSCN poisoning experiment revealed that atomically dispersed Ir was responsible for the high ORR activity. Moreover, the Ir_1-N/C catalyst was stable in acid, which displayed the current density retention of 97% after a 10,000-second ORR test. The excellent ORR performance of Ir_1-N/C was further validated in an assembled H_2-O_2 PEMFC, where there was a peak power density of 870 mW·cm^{-2}.

Some nonprecious-metal-based SACs have been demonstrated to be favorable for acidic ORR and promising in practical PEMFCs, especially for atomically dispersed M-N-C catalysts [173–176]. Over the last few years, atomic Fe-N-C electrocatalysts have been viewed as the potential substitutes of Pt in fuel cells, some of which displayed high activity and selectivity toward 4e$^-$ ORR. In order to fabricate more high-performance Fe-N-C catalysts in PEMFCs, researchers mainly focused on the exploration of active sites for acidic ORR. Based on the

experimental and theoretical data, it was proposed that the single Fe atoms bound to N can help to enhance the electrochemical performance of acidic ORR, and Fe-N_x-C moieties (including Fe-N_4-C, Fe-N_2-C, etc.) were generally accepted as acid-resistant active centers for ORR. Under the aid of advanced atomic-scale characterizations and DFT calculations, the structural properties of Fe-N_x-C centers were further studied. It was found that the change of Fe 3d-electron density will have an effect on the σ-type bonding between the single-atom Fe and the orbitals of oxygenated intermediates (*O_2, *OOH, *O, and *OH), thereby influencing the catalytic activity of Fe-N_x-C. By changing the 3d electron density of Fe, the ORR activity of Fe-N_x-C can be optimally regulated. Specifically, it was widely acknowledged that the Fe-N_4 sites can be viewed as the origin of high ORR activity in acid. For example, Li and co-workers fabricated a SA-Fe-N-1.5-800 catalyst via supramolecular route for ORR, where main Fe-N_4/C sites existed (Fig. 15) [173]. In 0.5 M H_2SO_4, the SA-Fe-N-1.5-800 catalyst exhibited high onset and half-wave potentials (E_{onset}, 0.941 V vs. RHE; $E_{1/2}$, 0.812 V vs. RHE), small Tafel slope (62 mV·dec^{-1}), and remarkable durability. The excellent ORR performance on SA-Fe-N was attributed to the formation of Fe-N_4 active centers, which has been verified by XAS characterization and theoretical simulations.

In terms of proposed Fe-N_4 sites, the type of N was still controversial to date. In 2002, Tang et al. reported that the Fe-pyrrolic-N_4 structure remained after the pyrolysis of Fe-containing macrocycles, which was experimentally demonstrated to be electroactive for ORR in 0.5 M H_2SO_4 [177]. Moreover, Fe-pyridinic-N_4 structure has been extensively proposed for the acidic ORR and PEMFC. Impressively, Zitolo et al. disclosed an explicit structure of FeN_4C_{12}, who specially determined the arrangement of carbon atoms around Fe-N_4 [174]. For porphyrin-like FeN_4C_{12} moieties, the pyridinic-N bridged micropores/slits, while the C_4-pyrrole-N ring was more inclined to bridge the edges of graphene.

In addition to Fe-N-C electrocatalysts, other atomically dispersed transition metal-based catalysts (such as Co-N-C, Mn-N-C, etc.) have been fabricated in PEMFCs. For instance, Wu and co-workers adopted surfactant-assisted MOF strategy to fabricate a core-shell single-atom Co-N-C catalyst (Co-N-C@F127), displaying the half-wave potential of 0.84 V vs. RHE in 0.5 M H_2SO_4 [175]. In the Co-N-C@F127-based PEMFC, high open-circuit voltage of 0.92 V vs. RHE and power density of 0.87 W·cm^{-2} can be achieved. Using DFT calculations, CoN_{2+2} (a Co-N_4 moiety bridging on two adjoining armchair graphitic edge) site was proposed as the origin of high ORR activity on Co-N-C@F127. For the specific structure of active sites, the calculated results showed that both CoN_4 (a Co-N_4 moiety embedded in an intact graphitic layer) and CoN_{2+2} in Co-N-C@F127 were viewed as the most possible active centers for acidic ORR (Fig. 16(a)). From the free energy diagram of ORR, it was revealed that the CoN_{2+2} site was more thermodynamically favorable for 4e$^-$ ORR as compared to CoN_4 (Fig. 16(b)). In the terms of *OOH dissociation step, the atomic details on CoN_{2+2} has been depicted. During the dissociation process, OOH was firstly adsorbed on the surface of single-atom Co center, which can simultaneously adsorb the dissociated O and OH species in the final state. Atomically dispersed Cu-based catalysts have also been studied in the acidic ORR. For instance, single Cu atoms coordinated by S and N showed excellent acidic ORR activity [178]. In the whole ORR process, the Cu-S_1N_3 moiety was proposed as an active center, which would provide vital guidance for fabricating more SACs in practical PEMFCs.

Currently, dual-metal SACs have been constructed for practical PEMFCs, some of which exhibited impressive ORR performances in acidic media. Combining DFT calculations with advance *in situ*/*ex situ* characterizations, it was concluded that the superior electrocatalytic performance of dual-metal SACs can be assigned to the synergy of bimetallic centers. As reported by Wang et al., the as-synthesized MOF-derived (Fe, Co)/N-C catalyst exhibited remarkable ORR activity and stability under acidic condition, and had promising perspectives in PEMFCs [179]. With the aid of atomic-scale characterizations (HAADF-STEM, Mössbauer spectra, and XAS analysis), it was disclosed that dual-metal Fe-Co/N sites were atomically dispersed in (Fe, Co)/N-C. The dual metal sites can boost the activation of O–O bond and thereby realize the facilitated ORR

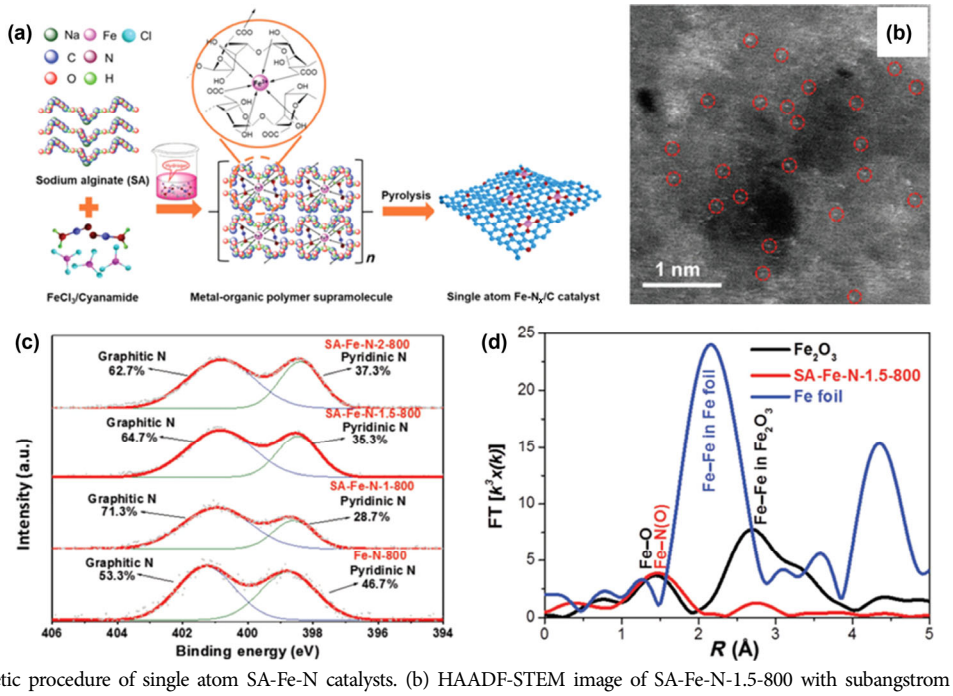

Figure 15 (a) Synthetic procedure of single atom SA-Fe-N catalysts. (b) HAADF-STEM image of SA-Fe-N-1.5-800 with subangstrom resolution. (c) High-resolution N 1s XPS spectra of SA-Fe-N-800 and Fe-N-800 samples. (d) k^3-weighted FT-EXAFS spectra of SA-Fe-N-1.5-800, Fe foil, and Fe_2O_3 samples. Reproduced with permission from Ref. [173], © WILEY-VCH Verlag GmbH & Co. KGaA, Weinheim 2018.

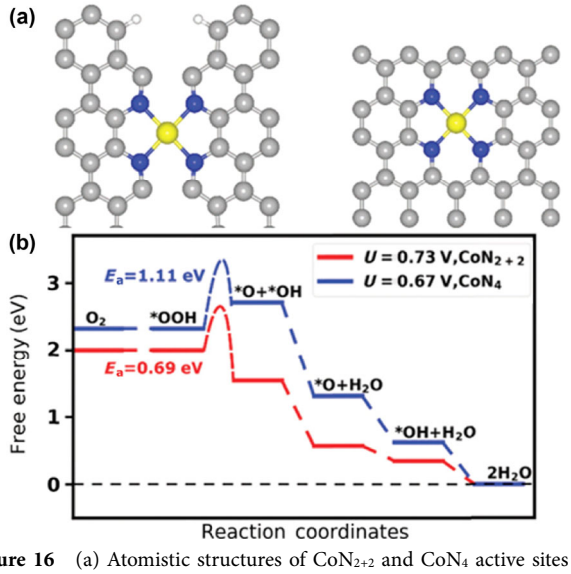

Figure 16 (a) Atomistic structures of CoN_{2+2} and CoN_4 active sites for the Co-N-C catalysts. (b) Calculated free energy evolution diagram for $4e^-$ ORR pathway on the CoN_{2+2} site under a limiting electrode potential of U = 0.73 V vs. RHE and on CoN_4 site under a limiting electrode potential of U = 0.67 V vs. RHE. Reproduced with permission from Ref. [175], © The Royal Society of Chemistry 2018.

process as demonstrated by DFT calculations. As a result, (Fe, Co)/N-C delivered high onset and half-wave potentials (E_{onset}, 1.06 V vs. RHE; $E_{1/2}$, 0.863 V vs. RHE), small Tafel slope (66 mV·dec^{-1}), and robust stability in 0.1 M $HClO_4$. Superior cell performance and long-term durability were also achieved in (Fe, Co)/N-C-based H_2/O_2 and H_2/air PEMFCs. Moreover, it was reported that the synergistic effects between both Co and Zn sites can lead to enhanced ORR performance. Sun and co-workers synthesized atomically dispersed Zn-Co dual sites on N-doped carbon (Zn/CoN-C) by high-temperature pyrolysis, using chitosan as C and N sources as well as zinc chloride and cobalt acetate as metal precursors [180]. It can be observed by HAADF-STEM that there were small bright dual spots in Zn/CoN-C, which can be attributed to the Zn/Co diatomic pairs (Figs. 17(a) and 17(b)). Furthermore, the Zn-Co distance was determined to be 0.22 ± 0.04 nm for Zn/CoN-C (Fig. 17(c)), in which $ZnCoN_6$ structure was proposed as the dominant active center for acidic ORR (Fig. 17(d)). Based on DFT calculations, it was revealed that the O–O bond length was significantly increased to 0.143 nm after the O_2 adsorption on $ZnCoN_6$, indicating that the $ZnCoN_6$ center can facilitate the O–O dissociation and improve the ORR activity (Fig. 17(e)). The Zn/CoN-C electrocatalyst with high ORR activity and stability has been demonstrated to afford outstanding fuel cell

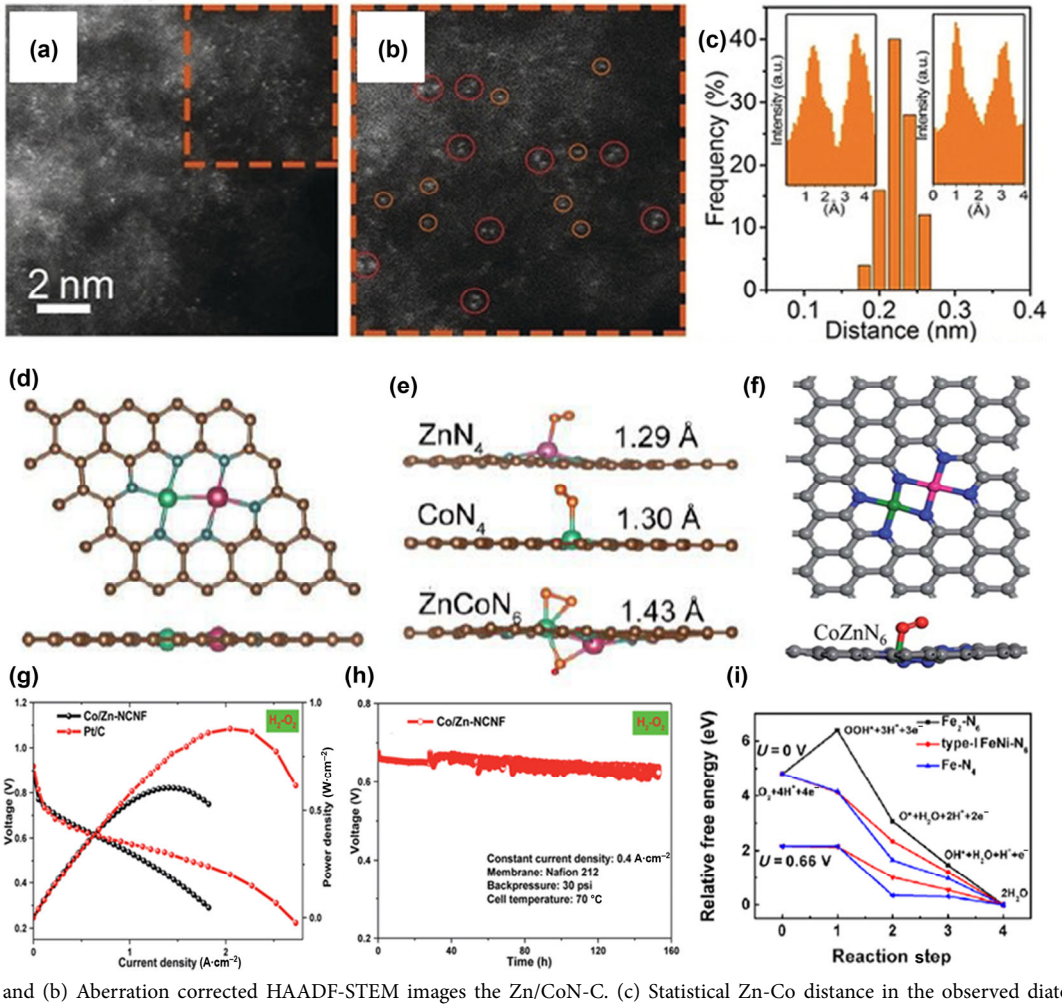

Figure 17 (a) and (b) Aberration corrected HAADF-STEM images the Zn/CoN-C. (c) Statistical Zn-Co distance in the observed diatomic pairs of Zn/CoN-C. (d) Relative position of Zn, Co and N for the Zn/CoN-C. (e) Optimized geometry of O_2 adsorption configuration on the ZnN_4, CoN_4 and $ZnCoN_6$ systems. Brown, blue, yellow, green, purple and red balls represent C, N, O, Zn, Co and H atoms, respectively. (f) Computational models of Co/Zn-NCNF and the corresponding optimized geometry of O_2 adsorption configuration on $CoZnN_6$. Brown, blue, red, green, and pink balls are C, N, O, Co, and Zn atoms, respectively. (g) Polarization curves of the Co/Zn-NCNF-based and commercial Pt/C-based H_2-O_2 PEMFCs. (h) 150 h stability test at a constant current density of 400 mA·cm^{-2}. (i) Free energy diagrams for the ORR on FeNi-N_6 (type I), Fe-N_4, and Fe_2-N_6. (a)–(e) Reproduced with permission from Ref. [180], © Wiley-VCH Verlag GmbH &Co. KGaA, Weinheim 2019. (f)–(h) Reproduced with permission from Ref. [181], © The Royal Society of Chemistry 2020. (i) Reproduced with permission from Ref. [182], © American Chemical Society 2020.

performance under acidic condition. Using Zn/CoN-C as the cathodic catalyst, the acidic H_2/O_2 fuel cell with a peak power density of 705 mW·cm^{-2} (at 0.5 V vs. RHE) was achieved. In another case, Yang and co-workers fabricated atomic Zn/Co dual sites on N-doped carbon nanofibers (Co/Zn-NCNF), where a novel $N_2CoN_2ZnN_2$ configuration was proposed as active centers for acidic ORR (Fig. 17(f)) [181]. In 0.1 M $HClO_4$, there was the half-wave potential of 0.797 V vs. RHE, Tafel slope of 82 mV·dec^{-1}, and good stability for ORR. As an efficient ORR electrocatalyst, Co/Zn-NCNF was used to assemble an acidic H_2-O_2 fuel cell, in which there was the open circuit voltage of 0.884 V vs. RHE and peak power density of 603 mW·cm^{-2}, and the stable voltage value of fuel cell was kept over 150 h (Figs. 17(g) and 17(h)). Recently, dual-metal Fe-Ni supported on N-doped carbon was reported in PEMFCs, where FeNi-N_6 (each Fe/Ni atom coordinated with four N atoms) was viewed as the origin of high ORR activity in acid as revealed by XAS analysis and DFT calculations [182]. As shown in Fig. 17(i), it can be concluded from free energy diagrams that FeNi-N_6 displayed higher activity than Fe-N_4 and Fe_2-N_6 during the whole ORR process. Experimentally, for acidic ORR, the FeNi-N_6 center delivered higher peak potential and half-wave potential as compared to Fe-N_4 and Ni-N_4. With the catalysis of FeNi-N_6, a superior PEMFC with maximum power density of ~ 216 mW·m^{-2} was realized. The electrocatalytic performance for acidic ORR on various SACs is presented in Table 3.

Table 3 Acidic ORR performance on SACs

SACs	Electrolyte	E_{onset} (V vs. RHE)	$E_{1/2}$ (V vs. RHE)	Ref.
Pt_1-N/BP	0.1 M $HClO_4$	—	0.76	[170]
Ru-N/G	0.1 M $HClO_4$	0.89	0.75	[183]
Ir_1-N/C	0.1 M $HClO_4$	0.923	0.831	[172]
Ir-NG-750	0.5 M H_2SO_4	0.846	0.77	[184]
SA-Fe-N	0.5 M H_2SO_4	0.941	0.812	[173]
Co-N-C@F127	0.5 M H_2SO_4	0.93	0.84	[175]
20Co-NC-1100	0.5 M H_2SO_4	0.93	0.80	[83]
CoNC700	0.1 M $HClO_4$	0.96	0.85	[185]
Co@NG-750	0.5 M H_2SO_4	0.79	0.69	[186]
S-Cu-ISA/SNC	0.5 M H_2SO_4	—	0.74	[178]
20Mn-NC-second	0.5 M H_2SO_4	—	0.80	[187]
(Fe, Co)/N-C	0.1 M $HClO_4$	1.06	0.863	[179]
Zn/CoN-C	0.1 M $HClO_4$	0.97	0.796	[180]
Co/Zn-NCNF	0.1 M $HClO_4$	0.997	0.797	[181]

3.3.2 *OER for PEM electrolyzers*

It is well known that water electrolyzers have played a vitally important role in energy conversion and storage, where oxygen evolution reaction (OER) significantly limited the whole water splitting process due to its sluggish reaction kinetics. Searching for excellent OER catalysts is crucial since most OER electrocatalysts were restricted to alkaline electrolytes [188, 189]. Under acidic condition, most metal-based catalysts often suffered from high overpotentials and poor durability, which cannot meet the practical application in PEM electrolyzers. Owing to the prominent advantages of PEM electrolyzers (such as load flexibility, fast dynamic response, etc.), the exploration of high-performance electrocatalysts has currently gained extensive attention for acidic OER, and some atomically dispersed metal-based materials have been developed as acidic OER catalysts. PGM catalysts such as IrO_x and RuO_x were proven to be highly active for PEM electrolyzers, however, their scarcity and exorbitant price largely limited the large-scale productions in practical PEM electrolyzers. Cai and co-workers adopted a double protecting approach to atomically disperse Ir on Fe nanoparticles and further encapsulate the IrFe nanoparticles into N-doped carbon nanotube (Ir-SA@Fe@NCNT, Fig. 18(a)) [190]. With the catalysis of Ir-SA@Fe@NCNT, there were desirable HER and OER overpotentials of 26 and 250 mV (at 10 mA·cm^{-2}), respectively, in 0.5 M H_2SO_4. The OER overpotential on Ir-SA@Fe@NCNT was lower than that on the corresponding Ir-NP@Fe@NCNT nanoparticle catalyst. Impressively, only applied voltage of 1.51 V vs. RHE was required to achieve 10 mA·cm^{-2} in the whole water splitting system, and Ir-SA@ Fe@NCNT was very stable. It was further revealed by DFT calculations that the superior OER performance of Ir-SA@Fe@NCNT in acid can be ascribed to Fe-Ir structure. This work provided great possibility for fabricating efficient and robust catalysts in PEM electrolyzers. The fabrication of single-atom Ir sites was also reported by Guan's group, which can realize low HER and OER overpotentials under the acidic condition [184].

Downsizing Ru nanoparticles into single atoms has been experimentally carried out, which was viewed as an efficient and feasible measure to facilitate the reaction kinetics of acidic OER. As reported by Yao and co-workers, single Ru_1-N_4 sites on carbon support (Ru-N-C) were demonstrated to be active and stable for acidic OER [191]. In 0.5 M H_2SO_4, the Ru-N-C catalyst exhibited superior OER performance with high mass activity (3,571 A·g_{metal}^{-1}), turnover frequency (3,348 h^{-1}) and stability, as well as low overpotential at 10 mA·cm^{-2} (267 mV). By DFT calculations, it was unveiled that the theoretical OER overpotential on O-Ru_1-N_4 (0.59 V vs. RHE) was lower than that on *ex situ* Ru_1-N_4 (0.83 V vs. RHE) and HO-Ru_1-N_4 (0.71 V vs. RHE), implying that oxygen species were pre-adsorbed by the single Ru_1-N_4 sites at OER working potentials (Fig. 18(b)). The acidic OER mechanism on Ru-N-C was proposed in Fig. 18(c). The single oxygen atom was firstly adsorbed on single-atom Ru to generate O-Ru_1-N_4 site, which further reacted with H_2O through nucleophilic attack and subsequent deprotonation to produce OOH* species. Followed by further proton coupled electron transfer, O_2 products were finally released. Wu et al. found that single Ru atoms supported on PtCu alloys (Ru_1-Pt_3Cu) were highly active and stable for acidic OER, showing a desirable overpotential of 220 mV at 10 mA·cm^{-2} [192]. The excellent OER performance in acid was assigned to the compressive strain of Pt_{skin} shells, which can optimally regulate the electronic structure of Ru centers and facilitate the OER kinetics.

As a naturally abundant element, iron has been chosen to fabricate Fe SACs for acidic OER. In 2018, Hou and co-workers developed a Fe-N coordinated carbon nanofiber supported on electrochemically exfoliated graphene (FeN_x/NF/EG), which favored the acidic OER [193]. In comparison to EG, the NF/EG and FeN_x/NF/EG samples improved significantly OER activities, implying that both N-doped carbon and Fe-N_x had a positive effect on the electrocatalytic performance of FeN_x/NF/EG (Fig. 18(d)). From Fig. 18(e), it was found that FeN_x/NF/EG possessed a remarkable OER overpotential of ~ 294 mV at 10 mA·cm^{-2} in 0.5 M H_2SO_4, which was lower than that of commercial Ir/C/EG (~ 320 mV at 10 mA·cm^{-2}). With the catalysis of FeN_x/NF/EG, a Tafel slope of 129 mV·dec^{-1} was obtained. The high stability of FeN_x/NF/EG for acidic OER has been verified by chronopotentiometric response curve at 20 mA·cm^{-2}. Specifically, the Fe-N_4 sites of FeN_x/NF/EG accounted for excellent acidic OER performance, which was well revealed by a combination of the XAS analysis, KSCN poisoning experiment

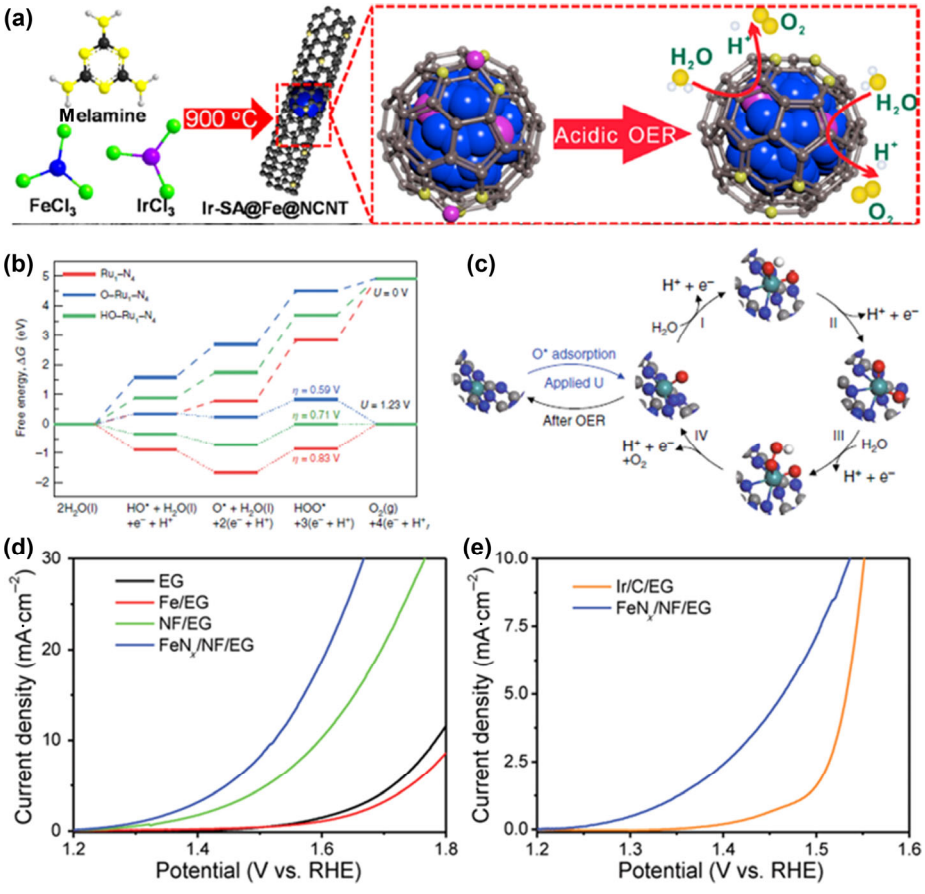

Figure 18 (a) Synthesis schematic of Ir-SA@Fe@NCNT electrocatalyst. (b) Free energy diagram for OER on Ru_1-N_4, O-Ru_1-N_4, and HO-Ru_1-N_4. (c) Schematic of the whole OER mechanism on Ru-N-C catalyst in the acidic electrolyte. Gray, blue, red, white, and light green balls represent C, N, O, H, and Ru atoms, respectively. All potentials are normalized to RHE. (d) OER polarization curves of EG, Fe/EG, NF/EG, and FeN_xNF/EG in 0.5 M H_2SO_4. (e) OER polarization curves of FeN_x/NF/EG and Ir/C/EG in 0.5 M H_2SO_4. (a) Reproduced with permission from Ref. [190], © American Chemical Society 2020. (b) and (c) Reproduced with permission from Ref. [191], © Cao, L. L. et al. 2019. (d) and (e) Reproduced with permission from Ref. [193], © WILEY-VCH Verlag GmbH & Co. KGaA, Weinheim 2018.

and DFT calculations. Beside iron, the molybdenum element is also used to fabricate high-performance OER electrocatalysts. Single-atom Mo (0.99 wt.%) decorated metallic Co_9S_8 (Mo-Co_9S_8@C) was constructed by Sun and co-workers, capable of catalyzing both HER and OER in a wide pH range (acidic, alkaline, and neutral media) [194]. In acid, the Mo-Co_9S_8@C catalyst exhibited the OER overpotential of 370 mV (at 10 mA·cm^{-2}) and Tafel slope of 90.3 mV·dec^{-1}, whose electrocatalytic activity kept unsignificant decay for 24 h. Using DFT calculations, it can be revealed that there was a four-step electron transfer process with multiple intermediates for acidic OER, and the synergy of isolated Mo atoms and Co-containing species was responsible for a low overpotential in the Mo-Co_9S_8@C-catalyzed water oxidation system (Fig. 19). The superior HER performance of Mo-Co_9S_8@C with low overpotential (98 mV at 10 mA·cm^{-2}), small Tafel slope (34.6 mV·dec^{-1}), and high stability was also achieved in the acid medium. For the proof-of-concept catalytic utilization, an AA battery (1.5 V vs. RHE) was demonstrated to be able to drive the Mo-Co_9S_8@C-catalyzed water splitting in acidic media, indicating the great perspectives of Mo-Co_9S_8@C in PEM electrolyzers. The electrocatalytic performance for acidic OER on various SACs is displayed in Table 4.

3.3.3 *NRR for ammonia electrosynthesis*

As an important raw material of fertilizers and energy carrier, ammonia (NH_3) is essential to sustain life on earth. In recent years, the electrochemical reduction of naturally abundant nitrogen into ammonia (NRR) has drawn extensive attention, in which low NH_3 yield and Faradaic efficiency exist. Among the reported NRR electrocatalysts, SACs have exhibited promising perspectives due to their maximized atom utilization and unsaturated coordination configuration [28, 33, 195]. At the atomic scale, carbon-based materials are generally considered as the best substrate to anchor isolated metal atoms, which can improve catalytic efficiency and stability of the SACs. By theoretical calculations, single Ru atoms immobilized on 2D carbon-based substrates (C_2N, triazine-C_3N_4, and γ-graphynes) favored fast intermediate adsorption and charge transfer along associative mechanism (including distal, alternating, and enzymatic pathways) for electrochemical NRR, where there was Ru-N or Ru-C coordination over the whole carbon nanopores [196]. For the proposed Ru@C_2N, Ru@T-C_3N_4, and Ru@γ-graphynes, there were similar limiting potentials but different potential-limiting steps (the generation of *N_2H, *NH_3, and *$NHNH_2$ on Ru@C_2N, Ru@T-C_3N_4, and Ru@γ-graphynes), and it was deduced that the Ru@T-C_3N_4 electrocatalyst was more energetically favorable for NRR, with theoretically high N_2 adsorption energy and low overpotential. Using first principles calculations, Wang and co-workers investigated the NRR performance and mechanism of single metal atoms (Cu, Pd, Pt, and Mo) on N-doped carbon, and found that the coordination of a single Mo atoms with a nitrogen and two carbon atoms (Mo-N_1C_2) can favorably catalyze NRR by an enzymatic pathway, giving a low theoretical overpotential of 0.24 V vs. RHE [197]. Li and co-workers theoretically predicted that the atomic Fe-N_3 moieties of Fe/N-doped graphene catalysts can serve as active sites for NRR, whose high spin polarization

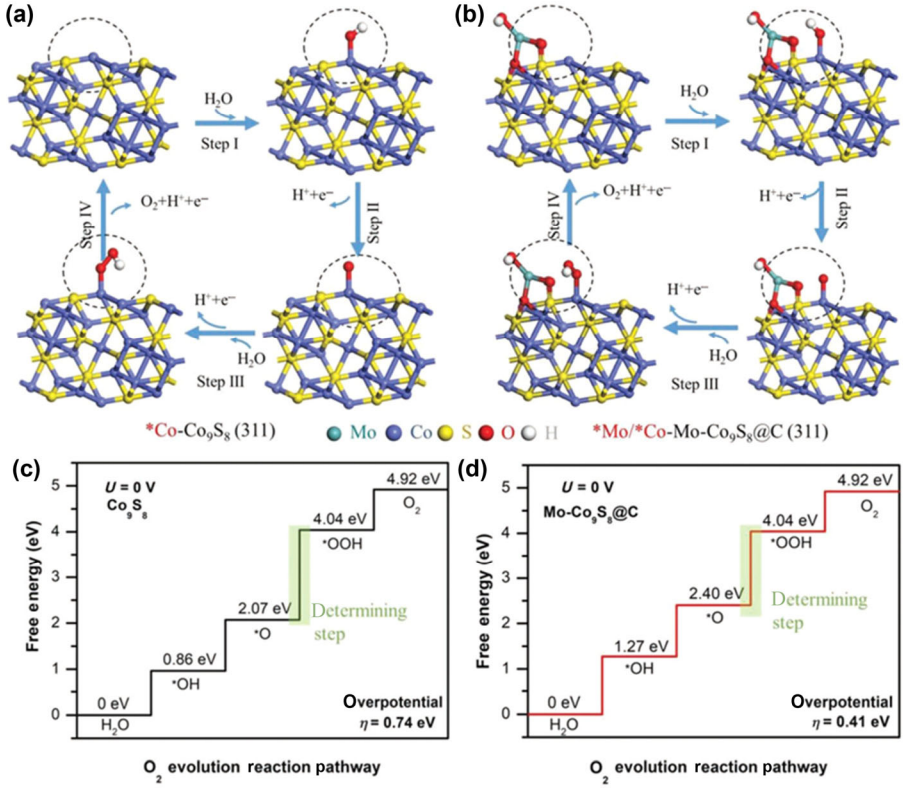

Figure 19 (a) and (b) DFT calculated free energy diagrams of the elementary electrochemical steps for proposed the 4e⁻ mechanism of acidic OER on pure Co_9S_8 and Mo-Co_9S_8@C. (c) and (d) Gibbs free energy diagrams for four steps of acidic OER on Co_9S_8 and Mo-Co_9S_8@C. Reproduced with permission from Ref. [194], © WILEY-VCH Verlag GmbH & Co. KGaA, Weinheim 2019.

Table 4 Acidic OER performance on SACs

SACs	Electrolyte	η (mV @ 10 mA·cm^{-2})	Tafel slope (mV·dec^{-1})	Ref.
Ir-SA@Fe@NCNT	0.5 M H_2SO_4	250	58.2	[190]
Ir-NG-750	0.5 M H_2SO_4	371	104	[184]
Ru-N-C	0.5 M H_2SO_4	267	52.6	[191]
Ru_1-Pt_3Cu	0.1 M $HClO_4$	220	—	[192]
FeN_x/NF/EG	0.5 M H_2SO_4	294	129	[193]
Mo-Co_9S_8@C	0.5 M H_2SO_4	370	90.3	[194]

was instructive for lowering the N–N bond breaking barrier, thereby realizing rapid adsorption of nitrogen and subsequent intermediate adsorption on the catalyst surface [198]. Defective BCN monolayer can be used as a promising support material to immobilize single metal atoms. Tang et al. studied single-atom Mo supported on BCN monolayer (Mo@BCN) by first principles calculations, and found that the Mo@BCN catalyst was highly active and stable for NRR [199]. With the theoretical overpotential of 0.42 V vs. RHE, an enzyme mechanism on Mo@BCN was realized. Noteworthily, theoretical studies revealed that the electronic structure of single sites can be adjusted by the introduction of second transition metals (M = Fe, Co, Ni, Cu, Zn, Mn, etc.) into M-N-C-based SACs, which may be conducive to enhancing catalytic performances in electrochemical reactions. It was found by Liu et al. that the Mn doping into atomic Fe-N-C catalysts improved obviously NRR activity and NH_3 selectivity, realizing a theoretical overpotential of 0.21 V vs. RHE via distal pathway [200]. In the as-designed Fe/Mn-N-C catalysts, both single Fe and Mn atoms can cooperatively catalyze the NRR to produce NH_3 as revealed by DFT calculations. Moreover, non-carbon-based materials have been developed to fabricate atomically dispersed metal-based catalysts, such as N-doped black phosphorus (BP) and MoS_2. It was found that single Mo atoms supported on N-doped BP were favorable for NRR, where Mo_1N_3 sites showed high activity and selectivity toward NH_3, with an ultralow theoretical overpotential of 0.02 V vs. RHE through distal pathway [201]. Zhao et al. studied systematically the potential of atomic transition metals embedded in MoS_2 nanosheets in electrochemical NRR, and the calculated result showed that the embedded metal atoms with different electronic properties greatly influenced the NRR activity of MoS_2 nanosheets [202]. Based on DFT calculations, it can be concluded that single Mo atoms embedded in MoS_2 nanosheet with an S-vacancy (Mo/MoS_2) exhibited outstanding NRR performance. In the Mo/MoS_2-catalyzed NRR, an onset potential of 0.53 V vs. RHE and the formation of *N_2H species as a potential-limiting step were uncovered.

Inspired by a series of theoretical explorations, great experimental progress of SACs for electrochemical NRR has been made [203]. For instance, atomically dispersed Au-based catalysts were demonstrated to be active and stable in a three-electrode NRR system. Wu and co-workers synthesized single-atom Au supported on carbon nitride (Au_1/C_3N_4) for NRR in acidic electrolyte [204]. It was disclosed by DFT calculations that the charge transfer from Au center to g-C_3N_4 may lead to d-orbital position of the Au atoms toward Fermi level, strengthening interaction between Au and NRR intermediates and thereby contributing to a superior NRR performance on Au_1/C_3N_4. As a result, the Au_1/C_3N_4 electrocatalyst showed NH_3 Faradaic efficiency of 11.1% and yield rate of 1,305 μg·h^{-1}·mg$_{cat}^{-1}$ (at –0.1 V vs. RHE) in 5 mM H_2SO_4. The NRR activity was

about 22.5 times higher than that of Au nanoparticles on carbon nitride. Oschatz and co-workers reported that atomically dispersed Au anchored by N-doped porous carbon (AuSAs-NDPC) displayed high NRR activity and NH_3 selectivity, with Faradaic efficiency of 12.3% and yield rate of 2.32 $\mu g \cdot h^{-1} \cdot cm^{-2}$ (at −0.2 V vs. RHE) in 0.1 M HCl [205]. For the AuNPs-NDPCs nanoparticle catalyst, only 5.7% Faradaic efficiency (−0.2 V vs. RHE) was realized for NRR. The superior NRR performance on AuSAs-NDPC can be attributed to the unique characteristics of NDPC, whose ample N species and high porosity can provide favorable channels for mass transport and stabilize isolated Au atoms to form more active sites for NRR. In another case, atomically dispersed Ru on N-doped carbon (Ru SAs/N-C) was fabricated for NRR [206]. In 0.05 M H_2SO_4, the Ru SAs/N-C electrocatalyst delivered a record-high NH_3 yield of 120.9 $\mu g \cdot h^{-1} \cdot mg_{cat}^{-1}$, along with Faradaic efficiency of 29.6%, 2.1-fold higher than that on Ru NPs/N-C. Under potentiostatic test, the NH_3 yield rate of less than 7% decayed after 12 h, indicating good durability of Ru SAs/N-C. Theoretical calculations revealed that Ru SAs/N-C was favorable for N_2 adsorption, and lower free energy (ΔG) values of N_2 dissociation were realized on Ru-N_3 and Ru-N_4 than that on Ru (101). By annealing Ru-confined UiO-66, Sun and co-workers fabricated a Ru@ZrO_2/NC catalyst for NRR, in which the isolated Ru atoms were highly dispersed on ZrO_2 and the sizes of ~ 88% Ru species ranged from 0.1 to 0.2 nm (Figs. 20(a)–20(c)) [207]. It can be concluded that the addition of ZrO_2 effectively suppressed HER and facilitated NH_3 production. Compared to Ru nanoparticles, Ru@ZrO_2/NC showed better NRR performance. As shown in Figs. 20(d)–20(f), the Ru@ZrO_2/NC catalyst displayed enhanced NH_3 Faradaic efficiency (~ 21% at −0.11 V vs. RHE), yield rate (3,665 $\mu g \cdot h^{-1} \cdot mg_{cat}^{-1}$ at −0.21 V vs. RHE), and partial current density in 0.1 M HCl. DFT calculations indicated that single Ru sites with O vacancies were highly active for NRR, where the O vacancies in ZrO_2 can help to improve the catalytic efficiency of single-atom Ru. Moreover, the yield rate and Faradaic efficiency of NH_3 were hardly degraded over the continuous NRR test of 60 h, suggesting a good cycling stability of Ru@ZrO_2/NC in acidic media (Fig. 20(g)). In addition, single Ru atoms supported on pure siliceous zeolite (Ru SAs/S-1) reported by Jiang et al. exhibited high catalytic activity and stability for NRR, which can pave a door for synthesizing other atomic metal-based catalysts in zeolite frameworks [208]. By DFT calculations, the NRR mechanism on Ru SAs/S-1 was revealed (Fig. 20(h)). It was indicated that N_2 was linearly adsorbed on the surface of single Ru sites (step A to B), while H_2 was adsorbed in zeolite channel (step B to C). Then, the adsorbed H_2(zeolites) reacted with N_2*, leading to the dissociation of N≡N triple bond (step C to D). Nextly, the other two H_2(zeolites) molecules further reacted with N_2* to release two NH_3 molecules, and the Ru SAs/S-1 catalyst with single Ru sites was finally recovered (step D to I).

In addition to atomically dispersed Au- and Ru-based catalysts, nonprecious transition metal-based SACs have been

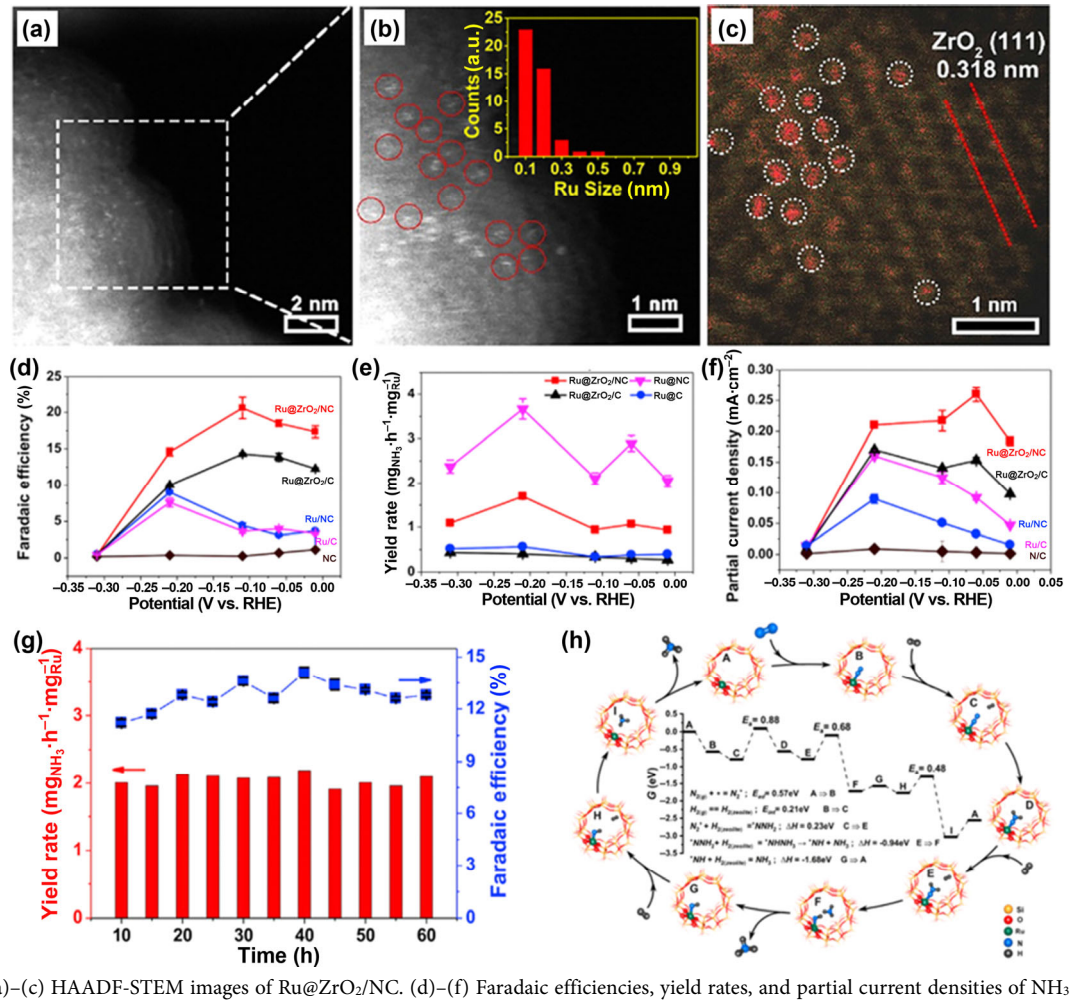

Figure 20 (a)–(c) HAADF-STEM images of Ru@ZrO_2/NC. (d)–(f) Faradaic efficiencies, yield rates, and partial current densities of NH_3 over Ru@NC, Ru@C, Ru@ZrO_2/NC, and Ru@ZrO_2/C at various applied potentials. (g) Long-term durability test at −0.21 V vs. RHE over Ru@ZrO_2/NC at ~ 10 °C. (h) DFT-calculated reaction profile of ammonia synthesis. (a)–(g) Reproduced with permission from Ref. [207], © Elsevier B.V. 2018. (h) Reproduced with permission from Ref. [208], © American Chemical Society 2019.

prepared as NRR electrocatalysts. Yan and co-workers synthesized atomically dispersed Fe on N-doped carbon (Fe_{SA}-N-C) for NRR [209]. The Fe_{SA}-N-C catalyst realized a Faradaic efficiency of 56.55% in 0.1 M KOH, which was not changed significantly during continuous NRR cycling. Similarly, Liu and co-workers also fabricated isolated Fe sites anchored on N-doped carbon (ISAS-Fe/NC), which were highly favorable for NRR in the neutral medium [210]. With the catalysis of ISAS-Fe/NC, there was NH_3 yield rate of (62.9 ± 2.7) $\mu g \cdot h^{-1} \cdot mg_{cat}^{-1}$ and Faradaic efficiency of (18.6 ± 0.8)% at –0.4 V vs. RHE. Within 24 h, negligible NRR activity of ISAS-Fe/NC degraded. The excellent performance of ISAS-Fe/NC can be attributed to the formation of abundant Fe-N_4 sites as revealed by EXAFS analysis and theoretical calculations. In addition, a new Fe-SnO_2 electrocatalyst was constructed for nitrogen reduction and oxidation [211]. In the Fe-SnO_2 catalyst, there were two characteristic distances of 0.334 and 0.264 nm on (110) and (101) lattice planes, respectively (Fig. 21(a)). The thickness of ~ 3 nm was discovered in Fe-SnO_2 from AFM images (Fig. 21(b)), and it was clearly observed that the local defects of Fe-SnO_2 occurred after the introduction of single-atom Fe (Fig. 21(c)). For acidic NRR, Fe-SnO_2 exhibited NH_3 yield of 82.7 $\mu g \cdot h^{-1} \cdot mg_{cat}^{-1}$ and Faradaic efficiency of 20.4% at –0.3 V vs. RHE. It was found that isolated Fe sites anchored by oxygen vacancies can effectively lower the energy barrier of N≡N cleavage and further improve the NRR performance. Moreover, Pennycook et al. reported that single-atom Cu on porous N-doped carbon (NC-Cu SA) can effectively catalyze NRR to produce ammonia, with high yield rate and Faradaic efficiency in acidic and alkaline media [212]. In 0.1 M KOH, NC-Cu SA was highly active for NRR, where NH_3 yield rate and corresponding Faradaic efficiency can reach (53.3 ± 1.86) $\mu g \cdot h^{-1} \cdot mg_{cat}^{-1}$ and 13.8%, respectively, at –0.35 V vs. RHE (Figs. 21(d) and 21(e)). Compared with NC-Cu SA, the NC-Cu nanoparticle catalyst exhibited lower NRR activity with NH_3 yield rate of 26.8 $\mu g \cdot h^{-1} \cdot mg_{cat}^{-1}$ and Faradaic efficiency of 4.7%. It was proven that the NH_3 release originated from the electrochemical reduction of N_2, and NH_3 yield rate and Faradaic efficiency on NC-Cu SA did not essentially degrade after 8 cycles (Figs. 21(f) and 21(g)). In 0.1 M HCl, NH_4^+ yield rate of (49.3 ± 0.70) $\mu g \cdot h^{-1} \cdot mg_{cat}^{-1}$ and Faradaic efficiency of 11.7% (at –0.3 V vs. RHE) were achieved on NC-Cu SA, which was stable during the NRR operation of 8 cycles (Figs. 21(h) and 21(i)). It was further unveiled by DFT calculations that the superior NRR performance on Cu SAC was derived from Cu-N_2 sites. Importantly, it has been confirmed that Mo was located at the top of volcano diagram for NRR, which motivated researchers to search for Mo SACs as excellent NRR catalysts. Various atomically dispersed Mo-based electrocatalysts have been prepared to date, which exhibited high activity, selectivity and stability for NRR. As reported by Xin and co-workers, single-atom Mo supported on N-doped porous carbon (SA-Mo/NPC) exhibited superior NRR performance, realizing NH_3 yield rate of (34.0 ± 3.6) $\mu g \cdot h^{-1} \cdot mg_{cat}^{-1}$ and Faradaic efficiency of (14.6 ± 1.6)% in 0.1 M KOH [213]. During the NRR process, the current density and NH_3 Faradaic efficiency had not significant decay (at –0.3 V vs. RHE) within 50,000 s,

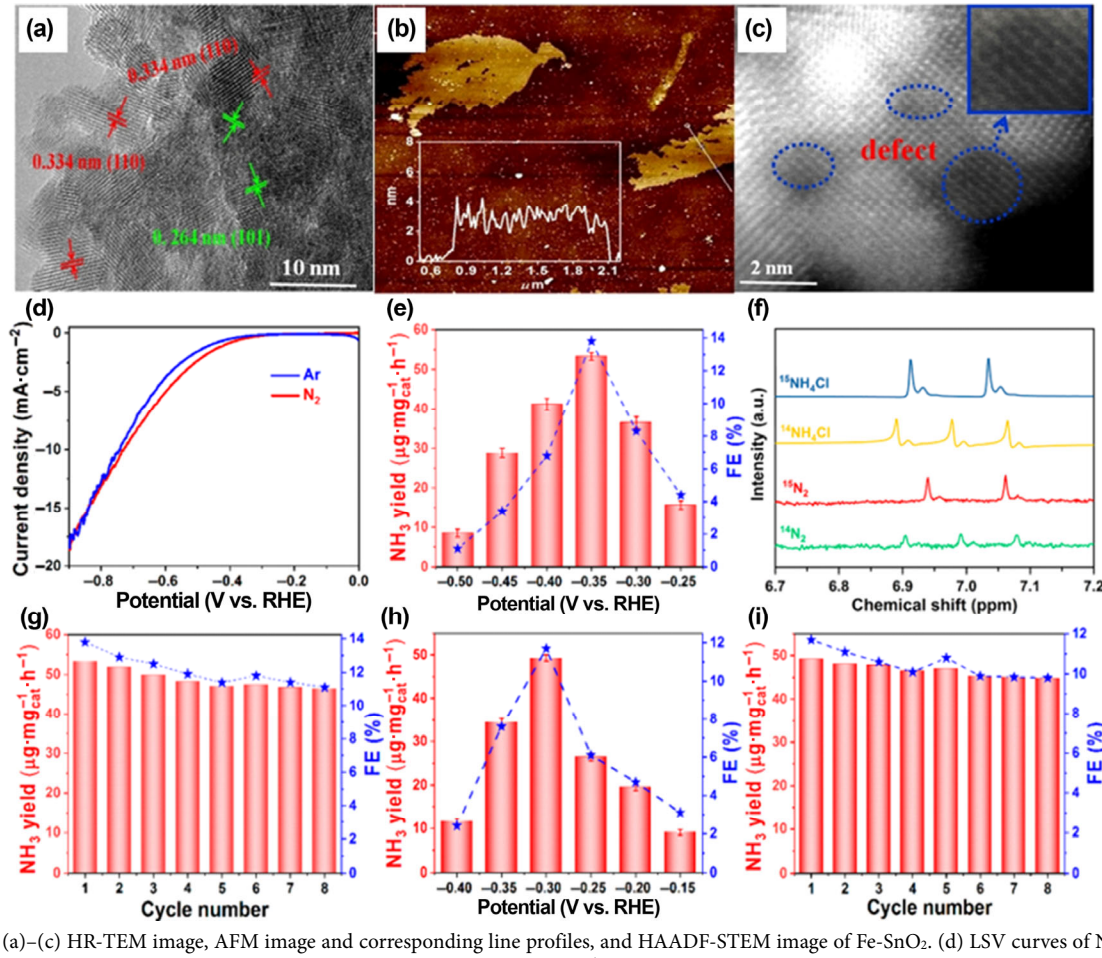

Figure 21 (a)–(c) HR-TEM image, AFM image and corresponding line profiles, and HAADF-STEM image of Fe-SnO_2. (d) LSV curves of NC-Cu SA in 0.1M KOH. (e)–(g) NH_3 yield rate and Faradaic efficiency at different potentials, ^1H NMR spectra of the electrode after 12 h of electrochemical reduction using $^{15}N_2$ as the feed gas, and NH_3 yield rates with increasing cycle numbers in 0.1 M KOH for NC-Cu SA. (h) and (i) NH_3 yield rate and Faradaic efficiency at different potentials, and NH_3 yield rates with increasing cycle numbers in 0.1 M HCl. (a)–(c) Reproduced with permission from Ref. [211], © WILEY-VCH Verlag GmbH & Co. KGaA, Weinheim 2020. (d)–(i) Reproduced with permission from Ref. [212], © American Chemical Society 2019.

indicating good stability of SA-Mo/NPC. Moreover, the superior NRR activity and durability of SA-Mo/NPC were also demonstrated in 0.1 M HCl. The outstanding NRR performances in both acid and alkali can be attributed to the abundant active sites and hierarchical porosity of SA-Mo/NPC. The electrocatalytic NRR performance on various SACs is provided in Table 5.

Table 5 Electrocatalytic NRR performance on SACs

SACs	Electrolyte	Faradaic efficiency (%)	Ammonia yield rate ($\mu g \cdot h^{-1} \cdot mg_{cat}^{-1}$)	Ref.
Au_1/C_3N_4	5 mM H_2SO_4	11.1	1305	[204]
AuSAs-NDPC	0.1 M HCl	12.3	2.32	[205]
Ru SAs/N-C	0.05 M H_2SO_4	29.6	120.9	[206]
Ru@ZrO_2/NC	0.1 M HCl	21	3665	[207]
Fe_{SA}-N-C	0.1 M KOH	56.55	7.48	[209]
ISAS-Fe/NC	0.1 M PBS	18.6 ± 0.8	62.9 ± 2.7	[210]
Fe-SnO_2	0.05 M H_2SO_4	20.4	82.7	[211]
NC-Cu SA	0.1 M KOH	13.8	53.3 ± 1.86	[212]
NC-Cu SA	0.1 M HCl	11.7	49.3 ± 0.70	[212]
SA-Mo/NPC	0.1 M KOH	14.6 ± 1.6	34.0 ± 3.6	[213]

3.4 Biomedicine

3.4.1 *Cancer therapy*

High mortality and therapeutic difficulty of cancer have motivated scientists to devote tremendous efforts to enhance the safety and efficacy of clinical cancer therapy, which has always been a research hotspot [25, 40]. By now, several types of SACs with enzyme-mimicking activities have been emerged as effective biomimetic catalysts to prevent damage and even kill cancer cells, and atomic enzyme catalysis has played an extremely crucial role in cancer therapy [214–217]. In the enzyme-mimicking reaction, SACs can catalyze O_2, H_2O_2, or H_2O to generate reactive oxygen species (ROS) including superoxide ion $O_2^{\bullet-}$, singlet oxygen $^1O_2$ and hydroxyl radical •OH, further leading to the cancer-cell apoptosis or necrosis [218]. It was reported that artificial single-atom Fe-based enzymes can be well applied in the biomedical field, some of which have exhibited preeminent catalytic captivity for treating cancer. Zhang and co-workers engineered an atomically dispersed Fe-N-C catalyst with oxidase-like activity, whose microstructure was sheet-like as reflected by SEM and bright-field STEM (BF-STEM) images [215]. In the Fe-N-C catalyst, Fe, N, and C elements were uniformly distributed, and it can be speculated that the Fe centers existed in the form of single atoms by complexing with aromatic N (Fig. 22(a)). During catalytic process, O_2 was activated by Fe-N-C to produce $^1O_2$, $O_2^{\bullet-}$, and H_2O_2 species, which can help to kill ~ 88% proliferative lung cancer cells (Fig. 22(b)). Moreover, easy separation and recycling merits of Fe-N-C have also been demonstrated, indicative of the promising prospect of artificial Fe-N-C-based enzymes in future clinical disease treatment. Shi and co-workers found that pegylated single-atom Fe catalysts (PSAF NCs) can effectively

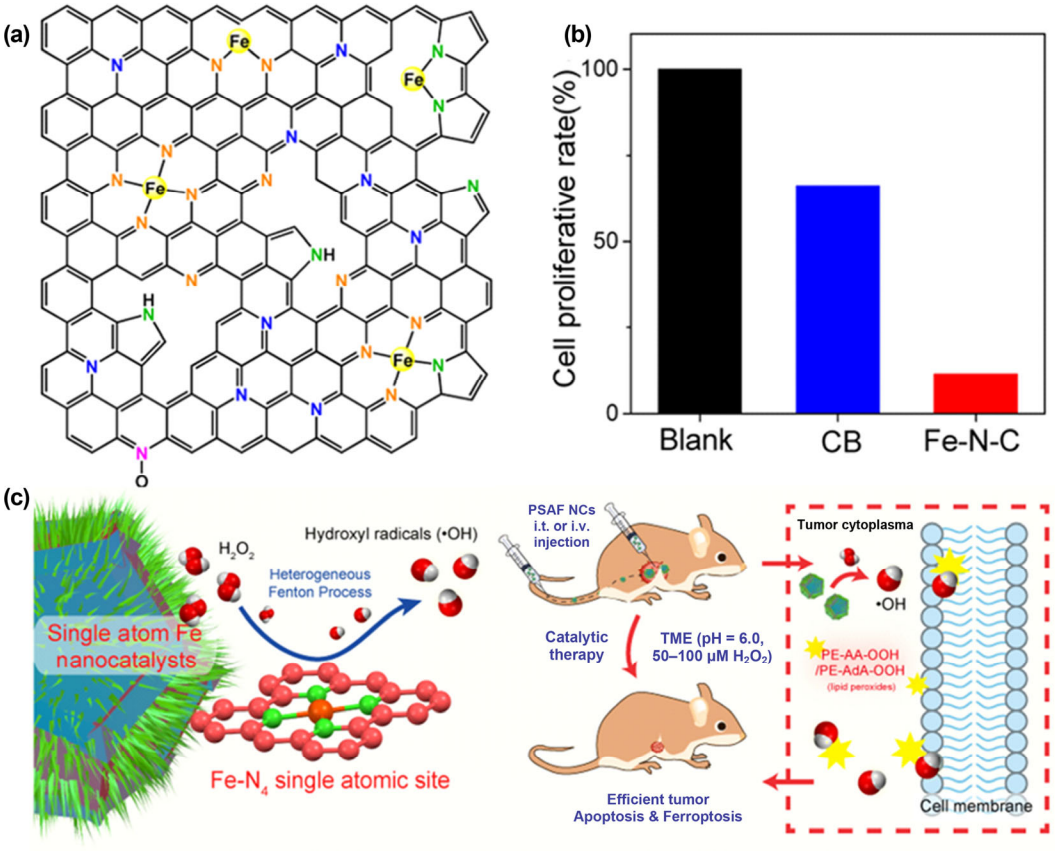

Figure 22 (a) Possible chemical structure of Fe-N-C. (b) Proliferation rate of carbon black (CB)- and Fe-N-C-incubated lung cancer cells determined by cell counting. (c) Schematic illustration of tumor therapy as catalyzed by PSAF NCs. (a) and (b) Reproduced with permission from Ref. [215], © American Chemical Society 2018. (c) Reproduced with permission from Ref. [216], © American Chemical Society 2019.

catalyze H_2O_2 to generate a large quantity of toxic •OH species under acidic tumor microenvironment, further leading to apoptosis and ferroptosis of malignant tumor cells (Fig. 22(c)) [216]. During *in vivo* catalytic therapeutics process, tumor cells were significantly suppressed after the intravenous and intratumoral administration of 20 mg·kg^{-1} PSAF NCs, while liver and kidney were not damaged. Aided by PSAF NCs, tumor growth inhibition can be realized, and there was no obvious weight attenuation in all controlled mice, suggesting the superior biocompatibility of PSAF NCs *in vivo*. Zhou et al. investigated the catalytic performance of single-atom Fe in a porphyrin-like MOF (P-MOF) for cancer treatment, and they found that P-MOF can facilitate the $^1O_2$ generation in tumors under near infrared (NIR) irradiation, further achieving cancer photodynamic and photothermal therapy, as well as photoacoustic imaging (PAI) [217]. From multispectral photoacoustic tomography (MSOT) images of the tumor, there were weak signals after injecting phosphate buffer solution (PBS), while it can be observed that the injection of P-MOF can apparently elevate the PAI signal (Figs. 23(a) and 23(b)). Furthermore, the mice showed no apparent weight loss after 20-day therapy of P-MOF, by which tumor size was sharply reduced as compared to Fe-porphyrin and PBS post-treatment (Figs. 23(c) and 23(d)). Aided by P-MOF, organ integrity and cell apoptosis were achieved, which proved excellent catalytic activity and biocompatibility of P-MOF *in vivo*. By these studies of atomically dispersed Fe-based catalysts, new vista of SACs as artificial enzymes *in vivo* has been opened up, which would be conducive to improving the therapeutic efficacy of cancer at the atomic level.

Beside enzyme-mimicking Fe-based SACs, other atomically dispersed metal-based catalysts have been specifically designed for cancer treatment. As reported by Shi and co-workers, single-atom Cu supported on hollow N-doped carbon sphere (Cu-HNCS) was elaborately fabricated with an enhanced suppression effect of tumor growth [218]. In the Cu-HNCS catalyst, Cu species were atomically dispersed with +1 – +2 valence (Figs. 24(a) and 24(b)), and the Cu-N coordination existed (Figs. 24(c)–24(e)). Furthermore, it was demonstrated that Cu-N_4 sites were most likely to occur in the Cu-N structure (Fig. 24(f)). With the catalysis of Cu-HNCS, O_2 and H_2O_2 were concurrently activated to form the corresponding ROS ($O_2^{\bullet-}$ and •OH) in the acidic tumor microenvironment, thereby achieving a satisfactory therapeutic efficacy through the oxidation of intracellular biomolecules. When Cu-HNCS

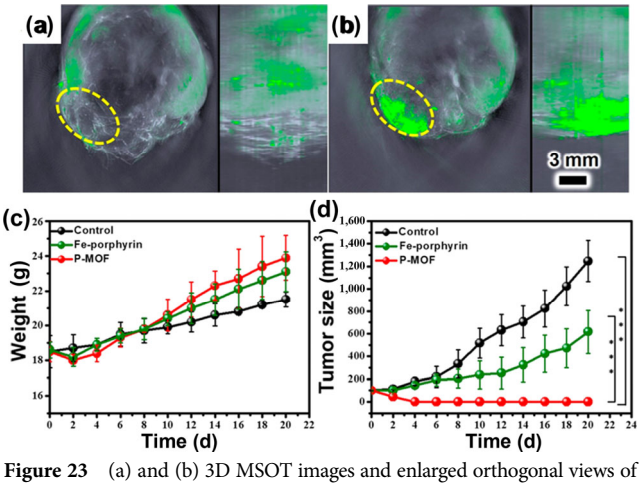

Figure 23 (a) and (b) 3D MSOT images and enlarged orthogonal views of tumor after the injection of PBS and P-MOF under 808 nm laser irradiation. (c) Body weights of various mice groups after the therapy. (d) Tumor growth curves under different treatments. Reproduced with permission from Ref. [217], © American Chemical Society 2019.

was injected into the mice, the Cu-HNCS sol was *in situ* turned into gel in the tumor region (Fig. 24(g)), which exhibited prominent biocompatibility and tumor suppression efficacy as shown in Figs. 24(h)–24(j). For over 48 days, all mice injected by Cu-HNCS survived, which further proved the great potential of Cu-HNCS in biomedicine (Fig. 24(k)). Additionally, DFT calculations were used to affirm that Cu-N_4 moieties as active sites can effectively combat tumor growth and enhance the survival rates, due to their low energy barrier and negative Gibbs free energy for such enzyme-mimicking reaction.

3.4.2 *Biosensing technology*

The concentration of analytes can be converted into electrical signal for detection by biosensing technology, which possesses the characteristics of simplicity, sensitivity and specificity, and has a broad application prospect in many fields (e.g., food detection, pharmaceutical analysis, etc.). With the help of biosensing technology, the activity of single-atom nanozymes in biochemical reactions can be well evaluated [12, 25]. Based on the color change in chemical reactions, colorimetric biosensors can be aided by SACs to detect multiple analytes [219, 220]. Dong and co-workers found that carbon nanoframe-confined FeN_5 active centers (FeN_5 SA/CNF) exhibited high oxidase-like activity, which can be used for biosensing ascorbic acid (AA) [221]. The FeN_5 SA/CNF catalyst showed higher oxidase-like activity than the nanoparticle catalysts such as CeO_2, Fe_3O_4, MnO_2, CuO, Au, Pd, and Pt. With the catalysis of FeN_5 SA/CNF, 3,3′,5,5′-tetramethylbenzidine (TMB) as a colorimetric substrate can be facilitated to produce the blue oxidized TMB (oxTMB), which would be suppressed in the presence of AA. The visible bule color gradually faded as AA concentration increased, and AA was determined in a liner range of 0.1–10 μM with a detection limit of 0.07 μM. Soon after, Huang and co-workers synthesized successfully Fe-N/C catalysts with single Fe-N_x sites through an one-step pyrolysis of Fe-Zn ZIFs precursors, which showed superior oxidase-like activity, stability and reproducibility [222]. The hydrolysis of ascorbic acid 2-phosphate (AAP) can be catalyzed by alkaline phosphatase (ALP) to generate AA, and the produced AA can inhibit the TMB chromogenic reaction on Fe-N/C. On this basis, the ALP activity was evaluated in the Fe-N/C-based colorimetric biosensor, ranging from 0.05 to100 U·L^{-1} with a low limit of detection (LOD) of 0.02 U·L^{-1}. Zhu and co-workers also fabricated Fe-N-C SACs with oxidase-like activity, which can be applied in the colorimetric biosensor to detect acetylcholinesterase (AChE) activity and organophosphorus compounds (OPs) [219]. The hydrolysis of acetylthiocholine (ATCh) can be catalyzed by AChE to produce thiocholine (TCh), further inhibiting the oxidase-like activity of Fe-N-C SACs. In the Fe-N-C SACs-based biosensor, the AChE activity was evaluated from 0.1 to 25 mU·mL^{-1} with a LOD of 0.014 mU·mL^{-1}. Moreover, the AChE activity gradually declined with increasing OPs, and the analysis of OPs concentration was achieved in the range of 0.1–10 μg·mL^{-1} with a LOD of 0.97 ng·mL^{-1}. In addition, single-atom Fe on N-doped carbons anchored on carbon nanotube (CNT/FeNC) has been reported to show excellent peroxidase-like activity in acidic media, which can be applied in a series of paper-based bioassays for detecting H_2O_2, glucose, and AA [223]. Based on TMB oxidation, the ultrasensitive colorimetric biosensing of H_2O_2, glucose and AA can be realized by CNT/FeNC coated paper (SDCP)-based bioassays. In SDCP-based bioassays, H_2O_2 was determined from 0.1 to 100 × 10^{-6} M with a LOD of 0.03 × 10^{-6} M, and glucose was detected from 0.1 to 10 × 10^{-3} M with a LOD of 0.02 × 10^{-3} M, as well as AA can be detected in the range of

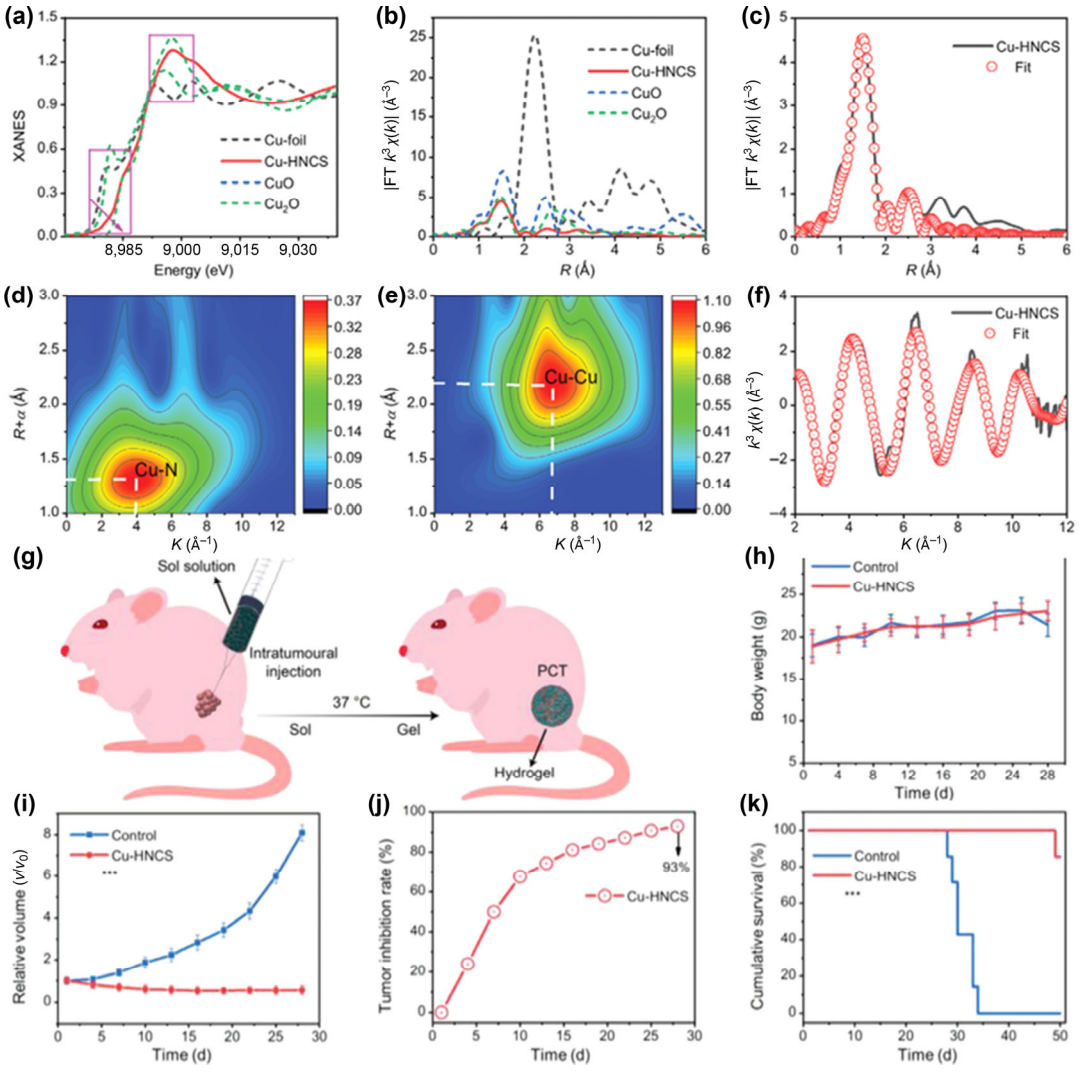

Figure 24 (a) and (b) XANES spectra and Fourier transform at Cu K-edge for Cu-HNCS and reference sample. (c) EXAFS fitting result of Cu-HNCS in *R* space. (d) and (e) Wavelet transform of Cu-HNCS and Cu foil, respectively. (f) EXAFS fitting result of Cu-HNCS at *k* space. (g) Schematics of intratumoral administrations and formation of an injectable Cu-HNCS hydrogel. (h)–(k) Body-weight, tumor proliferation, relative tumor inhibition rates, and survival curves of mice treated with blank hydrogels and Cu-HNCS hydrogels. Reproduced with permission from Ref. [218], © WILEY-VCH Verlag GmbH & Co. KGaA, Weinheim 2020.

0.1 to 10 × 10^{-6} M with a LOD of 0.03 × 10^{-6} M. Noteworthily, a Fe-N-C single-atom nanozyme (Fe-N-C SAN) synthesized by Lin et al. exhibited a ultra-high peroxidase-like activity of a specific activity of 57.76 U·mg^{-1} (far higher than that of 5.143 U·mg^{-1} on Fe_3O_4 nanoparticles) and strong stability, which can be used as a promising substitute to natural horseradish peroxidase (HRP) [220]. In the presence of BChE, butyrylcholine (BCh) was hydrolyzed into TCh, which would suppress the TMB oxidation reaction catalyzed by Fe-N-C SAN. By using Fe-N-C SAN-based colorimetric biosensing, butyrylcholinesterase (BChE) activity can be sensitively determined in a linear range of 0.1–10 U·L^{-1} with the LOD of 0.054 U·L^{-1}. Furthermore, a BChE activity assay can be attained in the paper bioassay integrated with a smartphone, ranging from 2 to 40 U·L^{-1} with a LOD of 1.7 U·L^{-1}. Recently, using a salt-template approach, Zhu et al. fabricated high-concentration single Cu atoms (~ 5.1 wt.%) on carbon nanosheets (Cu-N-C) with excellent peroxidase-like activity [224]. By combining the artificial Cu-N-C enzyme, natural choline oxidase (ChOx) and AChE, a novel three-enzyme-based cascade system was successfully constructed for the colorimetric biosensing of acetylcholine (ACh) and organophosphorus pesticides (OP). In such colorimetric method, the hydrolysis of ACh was catalyzed by AChE to generate choline, which was then oxidized into betaine and H_2O_2 with the aid of ChOx. Subsequently, the produced H_2O_2 can be reacted with colorless TMB via Cu-N-C enzyme, presenting a visible blue color. For the ACh detection, it was disclosed that the concentration of ACh ranged from 10 to 8,000 μM with the LOD of 1.24 μM. The AChE activity declined with the addition of OP, and there was a wide range of 1–300 ng·mL^{-1} and a LOD of 0.60 ng·mL^{-1} for the colorimetric determination of OP. In these SACs-based colorimetric biosensing reported previously, it can be concluded that single-atom enzymes have currently played a vitally important role in biosensors, and an integration of the sensitive biosensing with immunoassay would be considerable to detect more analytes in future biomedicine.

On the basis of electrochemical response changes, electrochemical biosensors have also been extensively applied to quantitatively determine multiple analytes, where electrochemical signals such as output potential and current can be amplified with the aid of SACs [40, 225]. As reported by Zheng and co-workers, a single Fe site enzyme (Fe-N-C SAE) was synthesized for the electrochemical biosensing of Hg^{2+} (Fig. 25(a)) [226]. As a superior electrochemical sensor, Fe-N-C SAE-functionalized solution-gated graphene transistor (SGGT) has been developed,

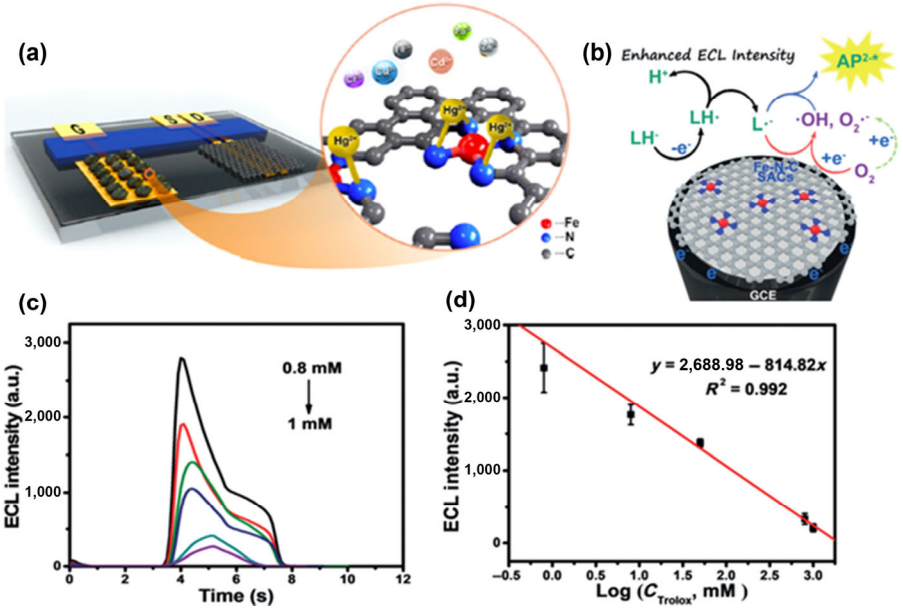

Figure 25 (a) Schematic diagram of a solution-gated graphene transistor (SGGT) based on the Fe-N-C SAE&Cs/Au-modified gate electrode for the detection of Hg^{2+}. (b) The mechanism of luminol-O_2 ECL systems with Fe-N-C SACs as coreactant accelerator. (c) The varied ECL signal with Trolox concentration in the range of 0.8 μM–1.0 mM. (d) The linear relationship between the Trolox concentration and ECL peak intensity. (a) Reproduced with permission from Ref. [226], © American Chemical Society 2020. (b)–(d) Reproduced with permission from Ref. [228], © Wiley-VCH Verlag GmbH & Co. KGaA, Weinheim 2019.

which can be used for the real-time detection of Hg^{2+}. There was a specific recognition between N atoms of Fe-N-C SAE and Hg^{2+} due to the chelation, and the output current signal was strengthened as Hg^{2+} concentration increased in the Fe-N-C SAE-functionalized SGGT. As a result, Hg^{2+} was determined in a linear range of 30 μM–3 nM, with a low detection limit of 1 nM. Using a Co single-atom catalyst (Co-SAC), Hou et al. realized an *in vivo* electrochemical biosensing [227]. Benefitting from the high activity of Co-SAC in H_2O_2 oxidation, an online Co-SAC-based biosensor was constructed to continuously monitor the glucose of rat brain. In the *in vivo* monitoring, glucose was finally determined from 5 μM to 1 mM. Moreover, the application of SACs in electrochemiluminescence (ECL) sensors has been recently reported. For instance, Zhu and co-workers found that single-atom Fe catalysts (Fe-N-C SACs) were able to efficiently catalyze O_2 into abundant ROS, and the produced ROS amplified significantly luminol ECL emission by reacting with the luminol anion radical (Fig. 25(b)) [228]. Using Fe-N-C SACs, a ECL sensor can be constructed for the analysis of Trolox concentration. As shown in Figs. 25(c) and 25(d), Trolox was detected in a linear range of 0.8 μM–1 mM, and there was a squared correlation coefficient (R^2) of 0.992 between Trolox concentration and ECL intensity. The biosensing performance on various SACs is listed in Table 6.

Table 6 Biosensing performance on SACs

SACs	Biosensing targets	Liner range	Detection limit	Ref.
FeN_5 SA/CNF	Ascorbic acid concentration	0.1–10 μM	0.07 μM	[221]
Fe-N/C	Alkaline phosphatase activity	0.05–100 $U{\cdot}L^{-1}$	0.02 $U{\cdot}L^{-1}$	[222]
Fe-N-C	Acetylcholinesterase activity	0.1–25 $mU{\cdot}mL^{-1}$	0.014 $mU{\cdot}mL^{-1}$	[219]
Fe-N-C	Organophosphorus compounds concentration	0.1–10 $\mu g{\cdot}mL^{-1}$	0.97 $ng{\cdot}mL^{-1}$	[219]
CNT/FeNC	H_2O_2 concentration	0.1–100 × 10^{-6} M	0.03 × 10^{-6} M	[223]
CNT/FeNC	Glucose concentration	0.1–10 × 10^{-3} M	0.02 × 10^{-3} M	[223]
CNT/FeNC	Ascorbic acid concentration	0.1–10 × 10^{-6} M	0.03 × 10^{-6} M	[223]
Fe-N-C SAN	Butyrylcholinesterase activity	0.1–10 $U{\cdot}L^{-1}$	0.054 $U{\cdot}L^{-1}$	[220]
Cu-N-C	Acetylcholine concentration	10–8,000 μM	1.24 μM	[224]
Cu-N-C	Acetylcholinesterase activity	1–300 $ng{\cdot}mL^{-1}$	0.60 $ng{\cdot}mL^{-1}$	[224]
Fe-N-C SAE	Hg^{2+} concentration	30 μM–3 nM	1 nM	[226]
Co-SAC	Glucose concentration	5 μM–1 mM	—	[227]
Fe-N-C SACs	Trolox concentration	0.8 μM–1 mM	0.8 μM	[228]

4 Summary and outlook

In summary, SACs are occupying an important status in many fields due to their unique properties (such as maximized atom utilization, unsaturated coordination environment, and well-defined/tunable electronic structure). This review highlights the recent advances on SACs, including their fabrication, characterizations, and versatile applications in the organic synthesis, environmental remediation, energy conversion, and biomedicine. The fabrication of SACs can be presented under the framework of bottom-up and top-down approaches. Different synthesis strategies are briefly introduced: wet chemistry, atomic-layer deposition, electrodeposition, high-energy ball milling, high-temperature pyrolysis, and gas-phase migration methods. At the atomic level, effective characterization techniques have been developed to identify the atomic structures of active sites, which are conducive to establishing the relation of structure- activity, and further designing more high-performance SACs in practical applications. With the aid of SACs, some representative reactions can be effectively boosted, favoring the applications in organic synthesis, environmental

remediation, energy conversion, and biomedicine. Based on the experimental and theoretical studies of SACs, it can be concluded that the optimal modulation of chemical compositions, morphologies, and structures can lead to enhanced catalytic performances toward target reactions. For SACs, the selection of different metal precursors and hard/soft templates, doping of heteroatoms, and construction of dual/multi-metal sites have been demonstrated to be crucial factors affecting the catalytic performances.

The characteristic geometric and electronic structures have promoted the development of SACs in different catalytic reactions. Nevertheless, SACs are still faced with several challenges in practical applications. To meet the future commercial/industrial/clinal requirements, maximizing the catalytic performance of SACs is vitally important. In this regard, we can adopt appropriate strategies to enhance the activity, selectivity, and stability of SACs. (1) The activity of SACs can be improved by increasing the density of active sites and intrinsic kinetic activity of each active sites. In the fabrication of SACs, the aggregation of metal atoms has been regarded as a major problem, distinctly lowering the density of single active sites. The optimal control of synthetic conditions and choice of support materials can help to effectively suppress the aggregation. In addition, increasing the metal loading is a key solution to enhance the active site density of SACs. More importantly, the intrinsic activity of each active sites has been demonstrated to have a great effect on the activity of SACs, which needs to be enhanced. Especially, the coordination structure of metal centers should be regulated to improve the intrinsic activity of single active sites, which can be influenced by coordination numbers, coordination atoms, and heteroatom dopants (B, S, P, etc.). The property of different support materials also needs to be further investigated, which is capable of affecting the chemical state and coordination structure of metal centers, thus altering the catalytic activity of SACs. Befitting from the synergistic effects, the design of dual/multi-metal sites may lead to enhanced activity. (2) For the selectivity of SACs, two or more pathways of the reaction are usually involved in industrial applications. Thus, the synthesis of high-selectivity SACs is imperative toward certain reaction, which can be achieved by altering metal types, or tuning the coordination environment of metal centers. In a specific coordination structure of catalytic sites, the change of metal element may help to improve the selectivity of SACs towards target reactions. Moreover, different coordination numbers and atoms (such as N, O, S, C, P) with metal can lead to diverse reaction pathways, which indicates that the detailed structures of active sites should be further systematically studied. (3) For the stability of SACs, the inactivation/collapse/aggregation/leaching phenomenon of SACs has been still a severe problem to be solved in the practical reaction process. It is well known that increasing the interaction of metal atoms and supports is an effective method to enhance the stability of SACs. To achieve this, we can select appropriate metals and supports. For example, improving the graphitization degree of carbon-based supports can be adopted for some electrochemical reactions due to possible carbon electrooxidation.

Additionally, the comprehensive understanding of reaction mechanisms on SACs is lacked, especially for the biomedical application. Nowadays, the catalytic processes on SACs are mainly analyzed by *ex situ* characterization methods, while some *in situ*/*operando* TEM, XPS, and XAS characterization tools have emerged to monitor the dynamic changes of intermediates, which are conducive to the understanding of structure-activity relationship and reaction mechanisms. Despite great potentials, the current *in situ*/*operando* characterizations are still in the early stage of developments, and sometimes cannot meet the practical requirements. Hence, further exploration of advanced *in situ* characterization and computational modeling methods should be considerable. Notedly, the applications of SACs are limited under practical conditions. To broaden the practical applicability, it is highly desirable to design some multifunctional SACs, which may be inspired by the advanced computational methods.

Acknowledgements

This work was supported by the National Natural Science Foundation of China (No. 22075099) and Natural Science Foundation of Jilin Province (No. 20180101291JC).

Conflict of Interest

The authors declare no conflict of interest.

References

[1] Aslam, U.; Rao, V. G.; Chavez, S.; Linic, S. Catalytic conversion of solar to chemical energy on plasmonic metal nanostructures. *Nat. Catal.* **2018**, *1*, 656–665.

[2] Yousefi, N.; Lu, X. L.; Elimelech, M.; Tufenkji, N. Environmental performance of graphene-based 3D macrostructures. *Nat. Nanotechnol.* **2019**, *14*, 107–119.

[3] Yang, B. W.; Chen, Y.; Shi, J. L. Nanocatalytic medicine. *Adv. Mater.* **2019**, *31*, 1901778.

[4] Jiang, D. W.; Ni, D. L.; Rosenkrans, Z. T.; Huang, P.; Yan, X. Y.; Cai, W. B. Nanozyme: New horizons for responsive biomedical applications. *Chem. Soc. Rev.* **2019**, *48*, 3683–3704.

[5] Huang, C. H.; Dong, J. C.; Sun, W. M.; Xue, Z. J.; Ma, J.; Zheng, L. R.; Liu, C.; Li, X.; Zhou, K.; Qiao, X. Z. et al. Coordination mode engineering in stacked-nanosheet metal–organic frameworks to enhance catalytic reactivity and structural robustness. *Nat. Commun.* **2019**, *10*, 2779.

[6] Sudarsanam, P.; Zhong, R. Y.; van den Bosch, S.; Coman, S. M.; Parvulescu, V. I.; Sels, B. F. Functionalised heterogeneous catalysts for sustainable biomass valorisation. *Chem. Soc. Rev.* **2018**, *47*, 8349–8402.

[7] Huang, Y. Y.; Ren, J. S.; Qu, X. G. Nanozymes: Classification, catalytic mechanisms, activity regulation, and applications. *Chem. Rev.* **2019**, *119*, 4357–4412.

[8] Zhang, Y.; Wang, F. M.; Liu, C. Q.; Wang, Z. Z.; Kang, L. H.; Huang, Y. Y.; Dong, K.; Ren, J. S.; Qu, X. G. Nanozyme decorated metal–organic frameworks for enhanced photodynamic therapy. *ACS Nano* **2018**, *12*, 651–661.

[9] Zhang, C.; Ni, D. L.; Liu, Y. Y.; Yao, H. L.; Bu, W. B.; Shi, J. L. Magnesium silicide nanoparticles as a deoxygenation agent for cancer starvation therapy. *Nat. Nanotechnol.* **2017**, *12*, 378–386.

[10] Huo, M. F.; Wang, L. Y.; Chen, Y.; Shi, J. L. Tumor-selective catalytic nanomedicine by nanocatalyst delivery. *Nat. Commun.* **2017**, *8*, 357.

[11] Zhang, C.; Bu, W. B.; Ni, D. L.; Zhang, S. J.; Li, Q.; Yao, Z. W.; Zhang, J. W.; Yao, H. L.; Wang, Z.; Shi, J. L. Synthesis of iron nanometallic glasses and their application in cancer therapy by a localized fenton reaction. *Angew. Chem., Int. Ed.* **2016**, *55*, 2101–2106.

[12] Jiao, L.; Yan, H. Y.; Wu, Y.; Gu, W. L.; Zhu, C. Z.; Du, D.; Lin, Y. H. When nanozymes meet single-atom catalysis. *Angew. Chem., Int. Ed.* **2020**, *59*, 2565–2576.

[13] Yang, X. F.; Wang, A. Q.; Qiao, B. T.; Li, J.; Liu, J. Y.; Zhang, T. Single-atom catalysts: A new frontier in heterogeneous catalysis. *Acc. Chem. Res.* **2013**, *46*, 1740–1748.

[14] Jiao, L.; Jiang, H. L. Metal-organic-framework-based single-atom catalysts for energy applications. *Chem* **2019**, *5*, 786–804.

[15] Maschmeyer, T.; Rey, F.; Sankar, G.; Thomas, J. M. Heterogeneous catalysts obtained by grafting metallocene complexes onto mesoporous silica. *Nature* **1995**, *378*, 159–162.

[16] Qiao, B. T.; Wang, A. Q.; Yang, X. F.; Allard, L. F.; Jiang, Z.; Cui, Y.

T.; Liu, J. Y.; Li, J.; Zhang, T. Single-atom catalysis of CO oxidation using Pt_1/FeO_x. *Nat. Chem.* **2011**, *3*, 634–641.
[17] Chen, Z. W.; Chen, L. X.; Yang, C. C.; Jiang, Q. Atomic (single, double, and triple atoms) catalysis: Frontiers, opportunities, and challenges. *J. Mater. Chem. A* **2019**, *7*, 3492–3515.
[18] Liu, J. Y. Catalysis by supported single metal atoms. *ACS Catal.* **2017**, *7*, 34–59.
[19] Li, C. Single Co atom catalyst stabilized in C/N containing matrix. *Chin. J. Catal.* **2016**, *37*, 1443–1445.
[20] Wang, B. W.; Wang, X. X.; Zou, J. X.; Yan, Y. C.; Xie, S. H.; Hu, G. Z.; Li, Y. G.; Dong, A. G. Simple-cubic carbon frameworks with atomically dispersed iron dopants toward high-efficiency oxygen reduction. *Nano Lett.* **2017**, *17*, 2003–2009.
[21] Xiong, Y.; Wang, S. B.; Chen, W. X.; Zhang, J.; Li, Q. H.; Hu, H. S.; Zheng, L. R.; Yan, W. S.; Gu, L.; Wang, D. S. et al. Construction of dual-active-site copper catalyst containing both $Cu\text{-}N_3$ and $Cu\text{-}N_4$ sites. *Small* **2021**, *17*, 2006834.
[22] Zhang, L. L.; Ren, Y. J.; Liu, W. G.; Wang, A. Q.; Zhang, T. Single-atom catalyst: A rising star for green synthesis of fine chemicals. *Natl. Sci. Rev.* **2018**, *5*, 653–672.
[23] Gawande, M. B.; Fornasiero, P.; Zbořil, R. Carbon-based single-atom catalysts for advanced applications. *ACS Catal.* **2020**, *10*, 2231–2259.
[24] Zhang, H. B.; Lu, X. F.; Wu, Z. P.; Lou, X. W. D. Emerging multifunctional single-atom catalysts/nanozymes. *ACS Cent. Sci.* **2020**, *6*, 1288–1301.
[25] Xiang, H. J.; Feng, W.; Chen, Y. Single-atom catalysts in catalytic biomedicine. *Adv. Mater.* **2020**, *32*, 1905994.
[26] Li, Y.; Wang, H. H.; Priest, C.; Li, S. W.; Xu, P.; Wu, G. Advanced electrocatalysis for energy and environmental sustainability via water and nitrogen reactions. *Adv. Mater.* **2020**, *33*, 2000381.
[27] Yan, H.; Su, C. L.; He, J.; Chen, W. Single-atom catalysts and their applications in organic chemistry. *J. Mater. Chem. A* **2018**, *6*, 8793–8814.
[28] Liu, J. Y. Single-atom catalysis for a sustainable and greener future. *Curr. Opin. Green Sust. Chem.* **2020**, *22*, 54–64.
[29] Gao, Z. Y.; Xu, S. P.; Li, L. L.; Yan, G.; Yang, W. J.; Wu, C. C.; Gates, I. D. On the adsorption of elemental mercury on single-atom TM (TM = V, Cr, Mn, Co) decorated graphene substrates. *Appl. Surf. Sci.* **2020**, *516*, 146037.
[30] Wang, Q. S.; Zhang, D. F.; Chen, Y.; Fu, W. F.; Lv, X. J. Single-atom catalysts for photocatalytic reactions. *ACS Sustainable Chem. Eng.* **2019**, *7*, 6430–6443.
[31] Yilmaz, G.; Peh, S. B.; Zhao, D.; Ho, G. W. Atomic- and molecular-level design of functional metal–organic frameworks (MOFs) and derivatives for energy and environmental applications. *Adv. Sci.* **2019**, *6*, 1901129.
[32] Sultan, S.; Tiwari, J. N.; Singh, A. N.; Zhumagali, S.; Ha, M.; Myung, C. W.; Thangavel, P.; Kim, K. S. Single atoms and clusters based nanomaterials for hydrogen evolution, oxygen evolution reactions, and full water splitting. *Adv. Energy Mater.* **2019**, *9*, 1900624.
[33] Yan, X.; Liu, D. L.; Cao, H. H.; Hou, F.; Liang, J.; Dou, S. X. Nitrogen reduction to ammonia on atomic-scale active sites under mild conditions. *Small Methods* **2019**, *3*, 1800501.
[34] Zhang, W. M.; Liu, Y. Q.; Zhang, L. P.; Chen, J. Recent advances in isolated single-atom catalysts for zinc air batteries: A focus review. *Nanomaterials* **2019**, *9*, 1402.
[35] Bai, L.; Duan, Z. Y.; Wen, X. D.; Si, R.; Guan, J. Q. Atomically dispersed manganese-based catalysts for efficient catalysis of oxygen reduction reaction. *Appl. Catal. B* **2019**, *257*, 117930.
[36] Bai, L.; Duan, Z. Y.; Wen, X. D.; Si, R.; Zhang, Q. Q.; Guan, J. Q. Highly dispersed ruthenium-based multifunctional electrocatalyst. *ACS Catal.* **2019**, *9*, 9897–9904.
[37] Lei, Y. P.; Wang, Y. C.; Liu, Y.; Song, C. Y.; Li, Q.; Wang, D. S.; Li, Y. D. Designing atomic active centers for hydrogen evolution electrocatalysts. *Angew. Chem., Int. Ed.* **2020**, *59*, 20794–20812.
[38] Sun, T. T.; Xu, L. B.; Wang, D. S.; Li, Y. D. Metal organic frameworks derived single atom catalysts for electrocatalytic energy conversion. *Nano Res.* **2019**, *12*, 2067–2080.
[39] Wu, W. J.; Liu, Y.; Liu, D.; Chen, W. X.; Song, Z. Y.; Wang, X. M.; Zheng, Y.; M. Lu, N.; Wang, C. X.; Mao, J. J. et al. Single copper sites dispersed on hierarchically porous carbon for improving oxygen reduction reaction towards zinc-air battery. *Nano Res.* **2021**, *14*, 998–1003.
[40] Zhang, X. L.; Li, G. L.; Chen, G.; Wu, D.; Zhou, X. X.; Wu, Y. N. Single-atom nanozymes: A rising star for biosensing and biomedicine. *Coord. Chem. Rev.* **2020**, *418*, 213376.
[41] Thomas, J. M. The concept, reality and utility of single-site heterogeneous catalysts (SSHCs). *Phys. Chem. Chem. Phys.* **2014**, *16*, 7647–7661.
[42] Li, Z. J.; Wang, D. H.; Wu, Y. E.; Li, Y. D. Recent advances in the precise control of isolated single-site catalysts by chemical methods. *Natl. Sci. Rev.* **2018**, *5*, 673–689.
[43] Kaiser, S. K.; Chen, Z. P.; Faust Akl, D.; Mitchell, S.; Pérez-Ramírez, J. Single-atom catalysts across the periodic table. *Chem. Rev.* **2020**, *120*, 11703–11809.
[44] Zhang, H. B.; Liu, G. G.; Shi, L.; Ye, J. H. Single-atom catalysts: Emerging multifunctional materials in heterogeneous catalysis. *Adv. Energy Mater.* **2018**, *8*, 1701343.
[45] Zhu, C. Z.; Fu, S. F.; Shi, Q. R.; Du, D.; Lin, Y. H. Single-atom electrocatalysts. *Angew. Chem., Int. Ed.* **2017**, *56*, 13944–13960.
[46] Moliner, M.; Gabay, J. E.; Kliewer, C. E.; Carr, R. T.; Guzman, J.; Casty, G. L.; Serna, P.; Corma, A. Reversible transformation of Pt nanoparticles into single atoms inside high-silica chabazite zeolite. *J. Am. Chem. Soc.* **2016**, *138*, 15743–15750.
[47] Wei, H. H.; Wu, H. B.; Huang, K.; Ge, B. H.; Ma, J. Y.; Lang, J. L.; Zu, D.; Lei, M.; Yao, Y. G.; Guo, W. et al. Ultralow-temperature photochemical synthesis of atomically dispersed Pt catalysts for the hydrogen evolution reaction. *Chem. Sci.* **2019**, *10*, 2830–2836.
[48] Wei, H. H.; Huang, K.; Wang, D.; Zhang, R. Y.; Ge, B. H.; Ma, J. Y.; Wen, B.; Zhang, S.; Li, Q. Y.; Lei, M. et al. Iced photochemical reduction to synthesize atomically dispersed metals by suppressing nanocrystal growth. *Nat. Commun.* **2017**, *8*, 1490.
[49] Lu, J. L.; Elam, J. W.; Stair, P. C. Synthesis and stabilization of supported metal catalysts by atomic layer deposition. *Acc. Chem. Res.* **2013**, *46*, 1806–1815.
[50] Detavernier, C.; Dendooven, J.; Pulinthanathu Sree, S.; Ludwig, K. F.; Martens, J. A. Tailoring nanoporous materials by atomic layer deposition. *Chem. Soc. Rev.* **2011**, *40*, 5242–5253.
[51] Kyriakou, G.; Boucher, M. B.; Jewell, A. D.; Lewis, E. A.; Lawton, T. J.; Baber, A. E.; Tierney, H. L.; Flytzani-Stephanopoulos, M.; Sykes, E. C. H. Isolated metal atom geometries as a strategy for selective heterogeneous hydrogenations. *Science* **2012**, *335*, 1209–1212.
[52] Lucci, F. R.; Darby, M. T.; Mattera, M. F. G.; Ivimey, C. J.; Therrien, A. J.; Michaelides, A.; Stamatakis, M.; Sykes, E. C. H. Controlling hydrogen activation, spillover, and desorption with Pd–Au single-atom alloys. *J. Phys. Chem. Lett.* **2016**, *7*, 480–485.
[53] Marcinkowski, M. D.; Darby, M. T.; Liu, J. L.; Wimble, J. M.; Lucci, F. R.; Lee, S.; Michaelides, A.; Flytzani-Stephanopoulos, M.; Stamatakis, M.; Sykes, E. C. H. Pt/Cu single-atom alloys as coke-resistant catalysts for efficient C–H activation. *Nat. Chem.* **2018**, *10*, 325–332.
[54] Lucci, F. R.; Liu, J. L.; Marcinkowski, M. D.; Yang, M.; Allard, L. F.; Flytzani-Stephanopoulos, M.; Sykes, E. C. H. Selective hydrogenation of 1,3-butadiene on platinum–copper alloys at the single-atom limit. *Nat. Commun.* **2015**, *6*, 8550.
[55] Hannagan, R. T.; Giannakakis, G.; Flytzani-Stephanopoulos, M.; Sykes, E. C. H. Single-atom alloy catalysis. *Chem. Rev.* **2020**, *120*, 12044–12088.
[56] Ge, J. J.; Li, Z. J.; Hong, X.; Li, Y. D. Surface atomic regulation of core–shell noble metal catalysts. *Chem.–Eur. J.* **2019**, *25*, 5113–5127.
[57] Zhou, M.; Dick, J. E.; Bard, A. J. Electrodeposition of isolated platinum atoms and clusters on bismuth—characterization and electrocatalysis. *J. Am. Chem. Soc.* **2017**, *139*, 17677–17682.
[58] Zhang, J. F.; Liu, J. Y.; Xi, L. F.; Yu, Y. F.; Chen, N.; Sun, S. H.; Wang, W. C.; Lange, K. M.; Zhang, B. Single-atom Au/NiFe layered double hydroxide electrocatalyst: Probing the origin of activity for oxygen evolution reaction. *J. Am. Chem. Soc.* **2018**, *140*, 3876–3879.
[59] Xuan, N. N.; Chen, J. H.; Shi, J. J.; Yue, Y. W.; Zhuang, P. Y.; Ba, K.; Sun, Y. Y.; Shen, J. F.; Liu, Y. Y.; Ge, B. H. et al. Single-atom electroplating on two dimensional materials. *Chem. Mater.* **2019**, *31*, 429–435.

[60] Wang, D. W.; Li, Q.; Han, C.; Xing, Z. C.; Yang, X. R. Single-atom ruthenium based catalyst for enhanced hydrogen evolution. *Appl. Catal. B* **2019**, *249*, 91–97.
[61] Qi, K.; Cui, X. Q.; Gu, L.; Yu, S. S.; Fan, X. F.; Luo, M. C.; Xu, S.; Li, N. B.; Zheng, L. R.; Zhang, Q. H. et al. Single-atom cobalt array bound to distorted 1T MoS_2 with ensemble effect for hydrogen evolution catalysis. *Nat. Commun.* **2019**, *10*, 5231.
[62] Jiang, K.; Liu, B. Y.; Luo, M.; Ning, S. C.; Peng, M.; Zhao, Y.; Lu, Y. R.; Chan, T. S.; de Groot, F. M. F.; Tan, Y. W. Single platinum atoms embedded in nanoporous cobalt selenide as electrocatalyst for accelerating hydrogen evolution reaction. *Nat. Commun.* **2019**, *10*, 1743.
[63] Zhao, D.; Zhuang, Z. W.; Cao, X.; Zhang, C.; Peng, Q.; Chen, C.; Li, Y. D. Atomic site electrocatalysts for water splitting, oxygen reduction and selective oxidation. *Chem. Soc. Rev.* **2020**, *49*, 2215–2264.
[64] Guo, X. G.; Fang, G. Z.; Li, G.; Ma, H.; Fan, H. J.; Yu, L.; Ma, C.; Wu, X.; Deng, D. H.; Wei, M. M. et al. Direct, nonoxidative conversion of methane to ethylene, aromatics, and hydrogen. *Science* **2014**, *344*, 616–619.
[65] Deng, D. H.; Chen, X. Q.; Yu, L.; Wu, X.; Liu, Q. F.; Liu, Y.; Yang, H. X.; Tian, H. F.; Hu, Y. F.; Du, P. P. et al. A single iron site confined in a graphene matrix for the catalytic oxidation of benzene at room temperature. *Sci. Adv.* **2015**, *1*, e1500462.
[66] Chen, X. Q.; Yu, L.; Wang, S.; Deng, D. H.; Bao, X. H. Highly active and stable single iron site confined in graphene nanosheets for oxygen reduction reaction. *Nano Energy* **2017**, *32*, 353–358.
[67] Wu, Y. E.; Wang, D. S.; Li, Y. D. Understanding of the major reactions in solution synthesis of functional nanomaterials. *Sci. China Mater.* **2016**, *59*, 938–996.
[68] Wu, Y. E.; Wang, D. S.; Zhou, G.; Yu, R.; Chen, C.; Li, Y. D. Sophisticated construction of Au islands on Pt–Ni: An ideal trimetallic nanoframe catalyst. *J. Am. Chem. Soc.* **2014**, *136*, 11594–11597.
[69] Zhang, M. L.; Wang, Y. G.; Chen, W. X.; Dong, J. C.; Zheng, L. R.; Luo, J.; Wan, J. W.; Tian, S. B.; Cheong, W. C.; Wang, D. S. et al. Metal (hydr)oxides@polymer core–shell strategy to metal single-atom materials. *J. Am. Chem. Soc.* **2017**, *139*, 10976–10979.
[70] Yin, P. Q.; Yao, T.; Wu, Y. E.; Zheng, L. R.; Lin, Y.; Liu, W.; Ju, H. X.; Zhu, J. F.; Hong, X.; Deng, Z. X. et al. Single cobalt atoms with precise N-coordination as superior oxygen reduction reaction catalysts. *Angew. Chem., Int. Ed.* **2016**, *55*, 10800–10805.
[71] Wang, X.; Chen, W. X.; Zhang, L.; Yao, T.; Liu, W.; Lin, Y.; Ju, H. X.; Dong, J. C.; Zheng, L. R.; Yan, W. S. et al. Uncoordinated amine groups of metal–organic frameworks to anchor single Ru sites as chemoselective catalysts toward the hydrogenation of quinoline. *J. Am. Chem. Soc.* **2017**, *139*, 9419–9422.
[72] Ji, S. F.; Chen, Y. J.; Fu, Q.; Chen, Y. F.; Dong, J. C.; Chen, W. X.; Li, Z.; Wang, Y.; Gu, L.; He, W. et al. Confined pyrolysis within metal–organic frameworks to form uniform Ru_3 clusters for efficient oxidation of alcohols. *J. Am. Chem. Soc.* **2017**, *139*, 9795–9798.
[73] Cheng, Y.; Zhao, S. Y.; Johannessen, B.; Veder, J. P.; Saunders, M.; Rowles, M. R.; Cheng, M.; Liu, C.; Chisholm, M. F.; De Marco, R. et al. Single-atom catalysts: Atomically dispersed transition metals on carbon nanotubes with ultrahigh loading for selective electrochemical carbon dioxide reduction. *Adv. Mater.* **2018**, *30*, 1870088.
[74] Zhang, B. X.; Zhang, J. L.; Shi, J. B.; Tan, D. X.; Liu, L. F.; Zhang, F. Y.; Lu, C.; Su, Z. Z.; Tan, X. N.; Cheng, X. Y. et al. Manganese acting as a high-performance heterogeneous electrocatalyst in carbon dioxide reduction. *Nat. Commun.* **2019**, *10*, 2980.
[75] Zhu, C. Z.; Shi, Q. R.; Xu, B. Z.; Fu, S. F.; Wan, G.; Yang, C.; Yao, S. Y.; Song, J. H.; Zhou, H.; Du, D. et al. Hierarchically porous M–N–C (M = Co and Fe) single-atom electrocatalysts with robust MN_x active moieties enable enhanced ORR performance. *Adv. Energy Mater.* **2018**, *8*, 1801956.
[76] Han, Y. H.; Wang, Y. G.; Xu, R. R.; Chen, W. X.; Zheng, L. R.; Han, A. J.; Zhu, Y. Q.; Zhang, J.; Zhang, H. B.; Luo, J. et al. Electronic structure engineering to boost oxygen reduction activity by controlling the coordination of the central metal. *Energy Environ. Sci.* **2018**, *11*, 2348–2352.
[77] Yang, L.; Shi, L.; Wang, D.; Lv, Y. L.; Cao, D. P. Single-atom cobalt electrocatalysts for foldable solid-state Zn-air battery. *Nano Energy* **2018**, *50*, 691–698.
[78] Wei, S. J.; Li, A.; Liu, J. C.; Li, Z.; Chen, W. X.; Gong, Y.; Zhang, Q. H.; Cheong, W. C.; Wang, Y.; Zheng, L. R. et al. Direct observation of noble metal nanoparticles transforming to thermally stable single atoms. *Nat. Nanotechnol.* **2018**, *13*, 856–861.
[79] Zhao, C.; Xiong, C.; Liu, X. K.; Qiao, M.; Li, Z. J.; Yuan, T. W.; Wang, J.; Qu, Y. T.; Wang, X. Q.; Zhou, F. Y. et al. Unraveling the enzyme-like activity of heterogeneous single atom catalyst. *Chem. Commun.* **2019**, *55*, 2285–2288.
[80] MacLaren, I.; Ramasse, Q. M. Aberration-corrected scanning transmission electron microscopy for atomic-resolution studies of functional oxides. *Int. Mater. Rev.* **2014**, *59*, 115–131.
[81] Liu, J. Y. Aberration-corrected scanning transmission electron microscopy in single-atom catalysis: Probing the catalytically active centers. *Chin. J. Catal.* **2017**, *38*, 1460–1472.
[82] Oxley, M. P.; Lupini, A. R.; Pennycook, S. J. Ultra-high resolution electron microscopy. *Rep. Prog. Phys.* **2016**, *80*, 026101.
[83] Wang, X. X.; Cullen, D. A.; Pan, Y. T.; Hwang, S.; Wang, M. Y.; Feng, Z. X.; Wang, J. Y.; Engelhard, M. H.; Zhang, H. G.; He, Y. H. et al. Nitrogen-coordinated single cobalt atom catalysts for oxygen reduction in proton exchange membrane fuel cells. *Adv. Mater.* **2018**, *30*, 1706758.
[84] Liu, M. M.; Wang, L. L.; Zhao, K. N.; Shi, S. S.; Shao, Q. S.; Zhang, L.; Sun, X. L.; Zhao, Y. F.; Zhang, J. J. Atomically dispersed metal catalysts for the oxygen reduction reaction: Synthesis, characterization, reaction mechanisms and electrochemical energy applications. *Energy Environ. Sci.* **2019**, *12*, 2890–2923.
[85] Zhang, W. P.; Xu, S. T.; Han, X. W.; Bao, X. H. *In situ* solid-state NMR for heterogeneous catalysis: A joint experimental and theoretical approach. *Chem. Soc. Rev.* **2012**, *41*, 192–210.
[86] Liu, W. G.; Zhang, L. L.; Liu, X.; Liu, X. Y.; Yang, X. F.; Miao, S.; Wang, W. T.; Wang, A. Q.; Zhang, T. Discriminating catalytically active FeN_x species of atomically dispersed Fe–N–C catalyst for selective oxidation of the C–H bond. *J. Am. Chem. Soc.* **2017**, *139*, 10790–10798.
[87] Wang, X. Q.; Chen, Z.; Zhao, X. Y.; Yao, T.; Chen, W. X.; You, R.; Zhao, C. M.; Wu, G.; Wang, J.; Huang, W. X. et al. Regulation of coordination number over single Co sites: Triggering the efficient electroreduction of CO_2. *Angew. Chem., Int. Ed.* **2018**, *57*, 1944–1948.
[88] Li, Q. H.; Chen, W. X.; Xiao, H.; Gong, Y.; Li, Z.; Zheng, L. R.; Zheng, X. S.; Yan, W. S.; Cheong, W. C.; Shen, R. A. et al. Fe isolated single atoms on S, N codoped carbon by copolymer pyrolysis strategy for highly efficient oxygen reduction reaction. *Adv. Mater.* **2018**, *30*, 1800588.
[89] Thirumalai, H.; Kitchin, J. R. Investigating the reactivity of single atom alloys using density functional theory. *Top. Catal.* **2018**, *61*, 462–474.
[90] Duchesne, P. N.; Li, Z. Y.; Deming, C. P.; Fung, V.; Zhao, X. J.; Yuan, J.; Regier, T.; Aldalbahi, A.; Almarhoon, Z.; Chen, S. W. et al. Golden single-atomic-site platinum electrocatalysts. *Nat. Mater.* **2018**, *17*, 1033–1039.
[91] Peng, B. S.; Liu, H. T.; Liu, Z. Y.; Duan, X. F.; Huang, Y. Toward rational design of single-atom catalysts. *J. Phys. Chem. Lett.* **2021**, *12*, 2837–2847.
[92] Xi, J. B.; Jung, H. S.; Xu, Y.; Xiao, F.; Bae, J. W.; Wang, S. Synthesis strategies, catalytic applications, and performance regulation of single-atom catalysts. *Adv. Funct. Mater.* **2021**, *31*, 2008318.
[93] Thomas, J. M.; Johnson, B. F. G.; Raja, R.; Sankar, G.; Midgley, P. A. High-performance nanocatalysts for single-step hydrogenations. *Acc. Chem. Res.* **2003**, *36*, 20–30.
[94] Yan, H.; Zhao, X. X.; Guo, N.; Lyu, Z.; Du, Y. H.; Xi, S. B.; Guo, R.; Chen, C.; Chen, Z. X.; Liu, W. et al. Atomic engineering of high-density isolated Co atoms on graphene with proximal-atom controlled reaction selectivity. *Nat. Commun.* **2018**, *9*, 3197.
[95] Wei, H. S.; Liu, X. Y.; Wang, A. Q.; Zhang, L. L.; Qiao, B. T.; Yang, X. F.; Huang, Y. Q.; Miao, S.; Liu, J. Y.; Zhang, T. FeO_x-supported platinum single-atom and pseudo-single-atom catalysts for chemoselective hydrogenation of functionalized nitroarenes. *Nat. Commun.* **2014**, *5*, 5634.
[96] Zhang, B.; Asakura, H.; Zhang, J.; Zhang, J. G.; De, S.; Yan, N. Stabilizing a $platinum_1$ single-atom catalyst on supported phosphomolybdic acid without compromising hydrogenation activity. *Angew. Chem., Int. Ed.* **2016**, *55*, 8319–8323.

[97] Wei, H. S.; Ren, Y. J.; Wang, A. Q.; Liu, X. Y.; Liu, X.; Zhang, L. L.; Miao, S.; Li, L.; Liu, J. Y.; Wang, J. H. et al. Remarkable effect of alkalis on the chemoselective hydrogenation of functionalized nitroarenes over high-loading Pt/FeO_x catalysts. *Chem. Sci.* **2017**, *8*, 5126–5131.

[98] Yan, X. L.; Duan, P.; Zhang, F. W.; Li, H.; Zhang, H. X.; Zhao, M.; Zhang, X. M.; Xu, B. S.; Pennycook, S. J.; Guo, J. J. Stable single-atom platinum catalyst trapped in carbon onion graphitic shells for improved chemoselective hydrogenation of nitroarenes. *Carbon* **2019**, *143*, 378–384.

[99] Sun, X. H.; Olivos-Suarez, A. I.; Osadchii, D.; Romero, M. J. V.; Kapteijn, F.; Gascon, J. Single cobalt sites in mesoporous N-doped carbon matrix for selective catalytic hydrogenation of nitroarenes. *J. Catal.* **2018**, *357*, 20–28.

[100] Merino, E. Synthesis of azobenzenes: The coloured pieces of molecular materials. *Chem. Soc. Rev.* **2011**, *40*, 3835–3853.

[101] Westerhaus, F. A.; Jagadeesh, R. V.; Wienhöfer, G.; Pohl, M. M.; Radnik, J.; Surkus, A. E.; Rabeah, J.; Junge, K.; Junge, H.; Nielsen, M. et al. Heterogenized cobalt oxide catalysts for nitroarene reduction by pyrolysis of molecularly defined complexes. *Nat. Chem.* **2013**, *5*, 537–543.

[102] Liu, W. G.; Zhang, L. L.; Yan, W. S.; Liu, X. Y.; Yang, X. F.; Miao, S.; Wang, W. T.; Wang, A. Q.; Zhang, T. Single-atom dispersed Co–N–C catalyst: Structure identification and performance for hydrogenative coupling of nitroarenes. *Chem. Sci.* **2016**, *7*, 5758–5764.

[103] Wang, L.; Guan, E. J.; Zhang, J.; Yang, J. H.; Zhu, Y. H.; Han, Y.; Yang, M.; Cen, C.; Fu, G.; Gates, B. C. et al. Single-site catalyst promoters accelerate metal-catalyzed nitroarene hydrogenation. *Nat. Commun.* **2018**, *9*, 1362.

[104] Makosch, M.; Sá, J.; Kartusch, C.; Richner, G.; van Bokhoven, J. A.; Hungerbühler, K. Hydrogenation of nitrobenzene over Au/MeO_x catalysts—A matter of the support. *ChemCatChem* **2012**, *4*, 59–63.

[105] Yan, H.; Cheng, H.; Yi, H.; Lin, Y.; Yao, T.; Wang, C. L.; Li, J. J.; Wei, S. Q.; Lu, J. L. Single-atom Pd_1/graphene catalyst achieved by atomic layer deposition: Remarkable performance in selective hydrogenation of 1,3-butadiene. *J. Am. Chem. Soc.* **2015**, *137*, 10484–10487.

[106] Vilé, G.; Albani, D.; Nachtegaal, M.; Chen, Z. P.; Dontsova, D.; Antonietti, M.; López, N.; Pérez-Ramírez, J. A stable single-site palladium catalyst for hydrogenations. *Angew. Chem., Int. Ed.* **2015**, *54*, 11265–11269.

[107] Liu, P. X.; Zhao, Y.; Qin, R. X.; Mo, S. G.; Chen, G. X.; Gu, L.; Chevrier, D. M.; Zhang, P.; Guo, Q.; Zang, D. D. et al. Photochemical route for synthesizing atomically dispersed palladium catalysts. *Science* **2016**, *352*, 797–800.

[108] Wang, J.; Zhao, X. C.; Lei, N.; Li, L.; Zhang, L. L.; Xu, S. T.; Miao, S.; Pan, X. L.; Wang, A. Q.; Zhang, T. Hydrogenolysis of glycerol to 1,3-propanediol under low hydrogen pressure over WO_x-supported single/pseudo-single atom Pt catalyst. *ChemSusChem* **2016**, *9*, 784–790.

[109] Zhao, X. C.; Wang, J.; Yang, M.; Lei, N.; Li, L.; Hou, B. L.; Miao, S.; Pan, X. L.; Wang, A. Q.; Zhang, T. Selective hydrogenolysis of glycerol to 1,3-propanediol: Manipulating the frustrated lewis pairs by introducing gold to Pt/WO_x. *ChemSusChem* **2017**, *10*, 819–824.

[110] Stephan, D. W. Frustrated lewis pairs: From concept to catalysis. *Acc. Chem. Res.* **2015**, *48*, 306–316.

[111] Qin, R. X.; Zhou, L. Y.; Liu, P. X.; Gong, Y.; Liu, K. L.; Xu, C. F.; Zhao, Y.; Gu, L.; Fu, G.; Zheng, N. F. Alkali ions secure hydrides for catalytic hydrogenation. *Nat. Catal.* **2020**, *3*, 703–709.

[112] Liu, G. L.; Robertson, A. W.; Li, M. M. J.; Kuo, W. C. H.; Darby, M. T.; Muhieddine, M. H.; Lin, Y. C.; Suenaga, K.; Stamatakis, M.; Warner, J. H. et al. MoS_2 monolayer catalyst doped with isolated Co atoms for the hydrodeoxygenation reaction. *Nat. Chem.* **2017**, *9*, 810–816.

[113] Zhang, J.; Zheng, C. Y.; Zhang, M. L.; Qiu, Y. J.; Xu, Q.; Cheong, W. C.; Chen, W. X.; Zheng, L. R.; Gu, L.; Hu, Z. P. et al. Controlling N-doping type in carbon to boost single-atom site Cu catalyzed transfer hydrogenation of quinoline. *Nano Res.* **2020**, *13*, 3082–3087.

[114] Bao, X. H. Preface: Catalysis—key to a sustainable future. *Natl. Sci. Rev.* **2015**, *2*, 137.

[115] Hackett, S. F. J.; Brydson, R. M.; Gass, M. H.; Harvey, I.; Newman, A. D.; Wilson, K.; Lee, A. F. High-activity, single-site mesoporous Pd/Al_2O_3 catalysts for selective aerobic oxidation of allylic alcohols. *Angew. Chem., Int. Ed.* **2007**, *46*, 8593–8596.

[116] Xie, S. H.; Tsunoyama, H.; Kurashige, W.; Negishi, Y.; Tsukuda, T. Enhancement in aerobic alcohol oxidation catalysis of Au_{25} clusters by single Pd atom doping. *ACS Catal.* **2012**, *2*, 1519–1523.

[117] Li, T. B.; Liu, F.; Tang, Y.; Li, L.; Miao, S.; Su, Y.; Zhang, J. Y.; Huang, J. H.; Sun, H.; Haruta, M. et al. Maximizing the number of interfacial sites in single-atom catalysts for the highly selective, solvent-free oxidation of primary alcohols. *Angew. Chem., Int. Ed.* **2018**, *57*, 7795–7799.

[118] Xie, J. H.; Yin, K. H.; Serov, A.; Artyushkova, K.; Pham, H. N.; Sang, X. H.; Unocic, R. R.; Atanassov, P.; Datye, A. K.; Davis, R. J. Selective aerobic oxidation of alcohols over atomically-dispersed non-precious metal catalysts. *ChemSusChem* **2017**, *10*, 359–362.

[119] Li, M.; Wu, S. J.; Yang, X. Y.; Hu, J.; Peng, L.; Bai, L.; Huo, Q. S.; Guan, J. Q. Highly efficient single atom cobalt catalyst for selective oxidation of alcohols. *Appl. Catal. A* **2017**, *543*, 61–66.

[120] Huang, K. T.; Fu, H. Q.; Shi, W.; Wang, H. J.; Cao, Y. H.; Yang, G. X.; Peng, F.; Wang, Q.; Liu, Z. G.; Zhang, B. S. et al. Competitive adsorption on single-atom catalysts: Mechanistic insights into the aerobic oxidation of alcohols over Co-N-C. *J. Catal.* **2019**, *377*, 283–292.

[121] Hu, P. P.; Huang, Z. W.; Amghouz, Z.; Makkee, M.; Xu, F.; Kapteijn, F.; Dikhtiarenko, A.; Chen, Y. X.; Gu, X.; Tang, X. Electronic metal–support interactions in single-atom catalysts. *Angew. Chem., Int. Ed.* **2014**, *53*, 3418–3421.

[122] He, W. L.; Yang, X. L.; Zhao, M.; Wu, C. D. Suspending ionic single-atom catalysts in porphyrinic frameworks for highly efficient aerobic oxidation at room temperature. *J. Catal.* **2018**, *358*, 43–49.

[123] Song, G. Y.; Wang, F.; Li, X. W. C–C, C–O and C–N bond formation via rhodium(III)-catalyzed oxidative C–H activation. *Chem. Soc. Rev.* **2012**, *41*, 3651–3678.

[124] Xiong, Y.; Sun, W. M.; Han, Y. H.; Xin, P. Y.; Zheng, X. S.; Yan, W. S.; Dong, J. C.; Zhang, J.; Wang, D. S.; Li, Y. D. Cobalt single atom site catalysts with ultrahigh metal loading for enhanced aerobic oxidation of ethylbenzene. *Nano Res.*, in press, DOI: 10.1007/s12274-020-3244-4.

[125] Lee, M.; Ko, S.; Chang, S. Highly selective and practical hydrolytic oxidation of organosilanes to silanols catalyzed by a ruthenium complex. *J. Am. Chem. Soc.* **2000**, *122*, 12011–12012.

[126] Mitsudome, T.; Arita, S.; Mori, H.; Mizugaki, T.; Jitsukawa, K.; Kaneda, K. Supported silver-nanoparticle-catalyzed highly efficient aqueous oxidation of phenylsilanes to silanols. *Angew. Chem., Int. Ed.* **2008**, *47*, 7938–7940.

[127] Chandrasekhar, V.; Boomishankar, R.; Nagendran, S. Recent developments in the synthesis and structure of organosilanols. *Chem. Rev.* **2004**, *104*, 5847–5910.

[128] Chen, Z.; Zhang, Q.; Chen, W. X.; Dong, J. C.; Yao, H. R.; Zhang, X. B.; Tong, X. J.; Wang, D. S.; Peng, Q.; Chen, C. et al. Single-site Au^I catalyst for silane oxidation with water. *Adv. Mater.* **2018**, *30*, 1704720.

[129] Sharma, R. K.; Dutta, S.; Sharma, S.; Zboril, R.; Varma, R. S.; Gawande, M. B. Fe_3O_4 (iron oxide)-supported nanocatalysts: Synthesis, characterization and applications in coupling reactions. *Green Chem.* **2016**, *18*, 3184–3209.

[130] Fu, N. H.; Liang, X.; Li, Z.; Chen, W. X.; Wang, Y.; Zheng, L. R.; Zhang, Q. H.; Chen, C.; Wang, D. S.; Peng, Q. et al. Fabricating Pd isolated single atom sites on C_3N_4/rGO for heterogenization of homogeneous catalysis. *Nano Res.* **2020**, *13*, 947–951.

[131] Zhang, X. Y.; Sun, Z. C.; Wang, B.; Tang, Y.; Nguyen, L.; Li, Y. T.; Tao, F. F. C–C coupling on single-atom-based heterogeneous catalyst. *J. Am. Chem. Soc.* **2018**, *140*, 954–962.

[132] Chen, Z. P.; Vorobyeva, E.; Mitchell, S.; Fako, E.; Ortuño, M. A.; López, N.; Collins, S. M.; Midgley, P. A.; Richard, S.; Vilé, G. et al. A heterogeneous single-atom palladium catalyst surpassing homogeneous systems for Suzuki coupling. *Nat. Nanotechnol.* **2018**, *13*, 702–707.

[133] Liu, Y. Q.; Zhou, Y.; Li, J.; Wang, Q.; Qin, Q.; Zhang, W.; Asakura, H.; Yan, N.; Wang, J. Direct aerobic oxidative homocoupling of benzene to biphenyl over functional porous organic polymer

supported atomically dispersed palladium catalyst. *Appl. Catal. B* **2017**, *209*, 679–688.
[134] Zhang, L. L.; Wang, A. Q.; Miller, J. T.; Liu, X. Y.; Yang, X. F.; Wang, W. T.; Li, L.; Huang, Y. Q.; Mou, C. Y.; Zhang, T. Efficient and durable Au alloyed Pd single-atom catalyst for the ullmann reaction of aryl chlorides in water. *ACS Catal.* **2014**, *4*, 1546–1553.
[135] Zhang, L. L.; Wang, A. Q.; Wang, W. T.; Huang, Y. Q.; Liu, X. Y.; Miao, S.; Liu, J. Y.; Zhang, T. Co–N–C catalyst for C–C coupling Reactions: On the catalytic performance and active sites. *ACS Catal.* **2015**, *5*, 6563–6572.
[136] Chen, Y. J.; Ji, S. F.; Chen, C.; Peng, Q.; Wang, D. S.; Li, Y. D. Single-atom catalysts: Synthetic strategies and electrochemical applications. *Joule* **2018**, *2*, 1242–1264.
[137] Cheng, Y.; Yang, S. Z.; Jiang, S. P.; Wang, S. Y. Supported single atoms as new class of catalysts for electrochemical reduction of carbon dioxide. *Small Methods* **2019**, *3*, 1800440.
[138] Wang, B.; Cai, H. R.; Shen, S. H. Single metal atom photocatalysis. *Small Methods* **2019**, *3*, 1800447.
[139] Wang, Y. C.; Liu, Y.; Liu, W.; Wu, J.; Li, Q.; Feng, Q. G.; Chen, Z. Y.; Xiong, X.; Wang, D. S.; Lei, Y. P. Regulating the coordination structure of metal single atoms for efficient electrocatalytic CO_2 reduction. *Energy Environ. Sci.* **2020**, *13*, 4609–4624.
[140] Zeng, L.; Xue, C. Single metal atom decorated photocatalysts: Progress and challenges. *Nano Res.* **2021**, *14*, 934–944.
[141] Tuo, J. Q.; Lin, Y. X.; Zhu, Y. H.; Jiang, H. L.; Li, Y. H.; Cheng, L.; Pang, R. C.; Shen, J. H.; Song, L.; Li, C. Z. Local structure tuning in Fe-N-C catalysts through support effect for boosting CO_2 electroreduction. *Appl. Catal. B* **2020**, *272*, 118960.
[142] Pan, F. P.; Zhang, H. G.; Liu, K. X.; Cullen, D.; More, K.; Wang, M. Y.; Feng, Z. X.; Wang, G.; Wu, G.; Li, Y. Unveiling active sites of CO_2 reduction on nitrogen-coordinated and atomically dispersed iron and cobalt catalysts. *ACS Catal.* **2018**, *8*, 3116–3122.
[143] Hou, Y.; Liang, Y. L.; Shi, P. C.; Huang, Y. B.; Cao, R. Atomically dispersed Ni species on N-doped carbon nanotubes for electroreduction of CO_2 with nearly 100% CO selectivity. *Appl. Catal. B* **2020**, *271*, 118929.
[144] Li, Y. F.; Chen, C.; Cao, R.; Pan, Z. W; He, H.; Zhou, K. B. Dual-atom Ag_2/graphene catalyst for efficient electroreduction of CO_2 to CO. *Appl. Catal. B* **2020**, *268*, 118747.
[145] Guan, A. X.; Chen, Z.; Quan, Y. L.; Peng, C.; Wang, Z. Q.; Sham, T. K.; Yang, C.; Ji, Y. L.; Qian, L. P.; Xu, X. et al. Boosting CO_2 electroreduction to CH_4 via tuning neighboring single-copper sites. *ACS Energy Lett.* **2020**, *5*, 1044–1053.
[146] Zhao, K.; Nie, X. W.; Wang, H. Z.; Chen, S.; Quan, X.; Yu, H. T.; Choi, W.; Zhang, G. H.; Kim, B.; Chen, J. G. Selective electroreduction of CO_2 to acetone by single copper atoms anchored on N-doped porous carbon. *Nat. Commun.* **2020**, *11*, 2455.
[147] Han, L. L.; Song, S. J.; Liu, M. J.; Yao, S. Y.; Liang, Z. X.; Cheng, H.; Ren, Z. H.; Liu, W.; Lin, R. Q.; Qi, G. C. et al. Stable and efficient single-atom Zn catalyst for CO_2 reduction to CH_4. *J. Am. Chem. Soc.* **2020**, *142*, 12563–12567.
[148] Ji, S. F.; Qu, Y.; Wang, T.; Chen, Y. J.; Wang, G. F.; Li, X.; Dong, J. C.; Chen, Q. Y.; Zhang, W. Y.; Zhang, Z. D. et al. Rare-earth single erbium atoms for enhanced photocatalytic CO_2 reduction. *Angew. Chem., Int. Ed.* **2020**, *59*, 10651–10657.
[149] Zhang, H. B.; Wei, J.; Dong, J. C.; Liu, G. G.; Shi, L.; An, P. F.; Zhao, G. X.; Kong, J. T.; Wang, X. J.; Meng, X. G. et al. Efficient visible-light-driven carbon dioxide reduction by a single-atom implanted metal–organic framework. *Angew. Chem., Int. Ed.* **2016**, *55*, 14310–14314.
[150] Gao, G. P.; Jiao, Y.; Waclawik, E. R.; Du, A. J. Single atom (Pd/Pt) supported on graphitic carbon nitride as an efficient photocatalyst for visible-light reduction of carbon dioxide. *J. Am. Chem. Soc.* **2016**, *138*, 6292–6297.
[151] Chao, C. Y. H. Comparison between indoor and outdoor air contaminant levels in residential buildings from passive sampler study. *Build. Environ.* **2001**, *36*, 999–1007.
[152] Fujiwara, K.; Pratsinis, S. E. Single Pd atoms on TiO_2 dominate photocatalytic NO_x removal. *Appl. Catal. B* **2018**, *226*, 127–134.
[153] Ou, M.; Wan, S. P.; Zhong, Q.; Zhang, S. L.; Wang, Y. N. Single Pt atoms deposition on g-C_3N_4 nanosheets for photocatalytic H_2 evolution or NO oxidation under visible light. *Int. J. Hydrogen Energy* **2017**, *42*, 27043–27054.
[154] Wu, Q.; Wei, W.; Lv, X. S.; Wang, Y. Y.; Huang, B. B.; Dai, Y. Cu@g-C_3N_4: An efficient single-atom electrocatalyst for NO electrochemical reduction with suppressed hydrogen evolution. *J. Phys. Chem. C* **2019**, *123*, 31043–31049.
[155] Tang, Y. A.; Chen, W. G.; Li, C. G.; Pan, L. J.; Dai, X. Q.; Ma, D. W. Adsorption behavior of Co anchored on graphene sheets toward NO, SO_2, NH_3, CO and HCN molecules. *Appl. Surf. Sci.* **2015**, *342*, 191–199.
[156] Gao, Z. Y.; Yang, W. J.; Ding, X. L.; Lv, G.; Yan, W. P. Support effects in single atom iron catalysts on adsorption characteristics of toxic gases (NO_2, NH_3, SO_3 and H_2S). *Appl. Surf. Sci.* **2018**, *436*, 585–595.
[157] Li, N.; Song, X. Z.; Wang, L.; Geng, X. L.; Wang, H.; Tang, H. Y.; Bian, Z. Y. Single-atom cobalt catalysts for electrocatalytic hydrodechlorination and oxygen reduction reaction for the degradation of chlorinated organic compounds. *ACS Appl. Mater. Interfaces* **2020**, *12*, 24019–24029.
[158] Wang, Y. B.; Zhao, X.; Cao, D.; Wang, Y.; Zhu, Y. F. Peroxymonosulfate enhanced visible light photocatalytic degradation bisphenol A by single-atom dispersed Ag mesoporous g-C_3N_4 hybrid. *Appl. Catal. B* **2017**, *211*, 79–88.
[159] Wang, F. L.; Wang, Y. F.; Li, Y. Y.; Cui, X. H.; Zhang, Q. X.; Xie, Z. J.; Liu, H. J.; Feng, Y. P.; Lv, W. Y.; Liu, G. G. The facile synthesis of a single atom-dispersed silver-modified ultrathin g-C_3N_4 hybrid for the enhanced visible-light photocatalytic degradation of sulfamethazine with peroxymonosulfate. *Dalton Trans.* **2018**, *47*, 6924–6933.
[160] An, S. F.; Zhang, G. H.; Wang, T. W.; Zhang, W. N.; Li, K. Y.; Song, C. S.; Miller, J. T.; Miao, S.; Wang, J. H.; Guo, X. W. High-density ultra-small clusters and single-atom fe sites embedded in graphitic carbon nitride (g-C_3N_4) for highly efficient catalytic advanced Oxidation processes. *ACS Nano* **2018**, *12*, 9441–9450.
[161] Yao, Y. J.; Yin, H. Y.; Gao, M. X.; Hu, Y.; Hu, H. H.; Yu, M. J.; Wang, S. B. Electronic structure modulation of covalent organic frameworks by single-atom Fe doping for enhanced oxidation of aqueous contaminants. *Chem. Eng. Sci.* **2019**, *209*, 115211.
[162] Li, Y.; Yang, T.; Qiu, S. H.; Lin, W. Q.; Yan, J. T.; Fan, S. S.; Zhou, Q. Uniform N-coordinated single-atomic iron sites dispersed in porous carbon framework to activate PMS for efficient BPA degradation via high-valent iron-oxo species. *Chem. Eng. J.* **2020**, *389*, 124382.
[163] Chen, M. T.; Wang, N.; Zhu, L. H. Single-atom dispersed Co–N–C: A novel adsorption-catalysis bifunctional material for rapid removing bisphenol A. *Catal. Today* **2020**, *348*, 187–193.
[164] Xu, H. D.; Jiang, N.; Wang, D.; Wang, L. H.; Song, Y. F.; Chen, Z. Q.; Ma, J.; Zhang, T. Improving PMS oxidation of organic pollutants by single cobalt atom catalyst through hybrid radical and non-radical pathways. *Appl. Catal. B* **2020**, *263*, 118350.
[165] Zhang, Y.; Liu, Y. X.; Xie, S. H.; Huang, H. B.; Guo, G. S.; Dai, H. X.; Deng, J. G. Supported ceria-modified silver catalysts with high activity and stability for toluene removal. *Environ. Int.* **2019**, *128*, 335–342.
[166] Zhang, H. Y.; Sui, S. H.; Zheng, X. M.; Cao, R. R.; Zhang, P. Y. One-pot synthesis of atomically dispersed Pt on MnO_2 for efficient catalytic decomposition of toluene at low temperatures. *Appl. Catal. B* **2019**, *257*, 117878.
[167] Xu, T. Z.; Zheng, H.; Zhang, P. Y. Isolated Pt single atomic sites anchored on nanoporous TiO_2 film for highly efficient photocatalytic degradation of low concentration toluene. *J. Hazard. Mater.* **2020**, *388*, 121746.
[168] Wang, Z. W.; Yang, H. G.; Liu, R.; Xie, S. H.; Liu, Y. X.; Dai, H. X.; Huang, H. B.; Deng, J. G. Probing toluene catalytic removal mechanism over supported Pt nano- and single-atom-catalyst. *J. Hazard. Mater.* **2020**, *392*, 122258.
[169] Wen, X. D.; Zhang, Q. Q.; Guan, J. Q. Applications of metal–organic framework-derived materials in fuel cells and metal-air batteries. *Coord. Chem. Rev.* **2020**, *409*, 213214.
[170] Liu, J.; Jiao, M. G.; Lu, L. L.; Barkholtz, H. M.; Li, Y. P.; Wang, Y.; Jiang, L. H.; Wu, Z. J.; Liu, D. J.; Zhuang, L. et al. High performance platinum single atom electrocatalyst for oxygen reduction reaction. *Nat. Commun.* **2017**, *8*, 15938.

[171] Liu, J.; Jiao, M. G.; Mei, B. B.; Tong, Y. X.; Li, Y. P.; Ruan, M. B.; Song, P.; Sun, G. Q.; Jiang, L. H.; Wang, Y. et al. Carbon-supported divacancy-anchored platinum single-atom electrocatalysts with superhigh Pt utilization for the oxygen reduction reaction. *Angew. Chem., Int. Ed.* **2019**, *58*, 1163–1167.

[172] Liu, Q. T.; Li, Y. C.; Zheng, L. R.; Shang, J. X.; Liu, X. F.; Yu, R. H.; Shui, J. L. Sequential synthesis and active-site coordination principle of precious metal single-atom catalysts for oxygen reduction reaction and PEM fuel cells. *Adv. Energy Mater.* **2020**, *10*, 2000689.

[173] Miao, Z. P.; Wang, X. M.; Tsai, M. C.; Jin, Q. Q.; Liang, J. S.; Ma, F.; Wang, T. Y.; Zheng, S. J.; Hwang, B. J.; Huang, Y. H. et al. Atomically dispersed Fe-N_x/C electrocatalyst boosts oxygen catalysis via a new metal-organic polymer supramolecule strategy. *Adv. Energy Mater.* **2018**, *8*, 1801226.

[174] Zitolo, A.; Goellner, V.; Armel, V.; Sougrati, M. T.; Mineva, T.; Stievano, L.; Fonda, E.; Jaouen, F. Identification of catalytic sites for oxygen reduction in iron- and nitrogen-doped graphene materials. *Nat. Mater.* **2015**, *14*, 937–942.

[175] He, Y. H.; Hwang, S.; Cullen, D. A.; Uddin, M. A.; Langhorst, L.; Li, B. Y.; Karakalos, S.; Kropf, A. J.; Wegener, E. C.; Sokolowski, J. et al. Highly active atomically dispersed CoN_4 fuel cell cathode catalysts derived from surfactant-assisted MOFs: Carbon-shell confinement strategy. *Energy Environ. Sci.* **2019**, *12*, 250–260.

[176] Chen, Y. J.; Gao, R.; Ji, S. F.; Li, H. J.; Tang, K.; Jiang, P.; Hu, H. B.; Zhang, Z. D.; Hao, H. G.; Qu, Q. Y. et al. Atomic-level modulation of electronic density at cobalt single-atom sites derived from metal–organic frameworks: Enhanced oxygen reduction performance. *Angew. Chem., Int. Ed.* **2021**, *60*, 3212–3221.

[177] Bouwkamp-Wijnoltz, A. L.; Visscher, W.; van Veen, J. A. R.; Boellaard, E.; van der Kraan, A. M.; Tang, S. C. On active-site heterogeneity in pyrolyzed carbon-supported iron porphyrin catalysts for the electrochemical reduction of oxygen: An *in situ* mössbauer study. *J. Phys. Chem. B* **2002**, *106*, 12993–13001.

[178] Shang, H. S.; Zhou, X. Y.; Dong, J. C.; Li, A.; Zhao, X.; Liu, Q. H.; Lin, Y.; Pei, J. J.; Li, Z.; Jiang, Z. L. et al. Engineering unsymmetrically coordinated Cu-S_1N_3 single atom sites with enhanced oxygen reduction activity. *Nat. Commun.* **2020**, *11*, 3049.

[179] Wang, J.; Huang, Z. Q.; Liu, W.; Chang, C. R.; Tang, H. L.; Li, Z. J.; Chen, W. X.; Jia, C. J.; Yao, T.; Wei, S. Q. et al. Design of N-coordinated dual-metal Sites: A stable and active pt-free catalyst for acidic oxygen reduction reaction. *J. Am. Chem. Soc.* **2017**, *139*, 17281–17284.

[180] Lu, Z. Y.; Wang, B.; Hu, Y. F.; Liu, W.; Zhao, Y. F.; Yang, R. O.; Li, Z. P.; Luo, J.; Chi, B.; Jiang, Z. et al. An isolated zinc–cobalt atomic pair for highly active and durable oxygen reduction. *Angew. Chem., Int. Ed.* **2019**, *58*, 2622–2626.

[181] Zang, J.; Wang, F. T.; Cheng, Q. Q.; Wang, G. L.; Ma, L. S.; Chen, C.; Yang, L. J.; Zou, Z. Q.; Xie, D. Q.; Yang, H. Cobalt/zinc dual-sites coordinated with nitrogen in nanofibers enabling efficient and durable oxygen reduction reaction in acidic fuel cells. *J. Mater. Chem. A* **2020**, *8*, 3686–3691.

[182] Zhou, Y. D.; Yang, W.; Utetiwabo, W.; Lian, Y. M.; Yin, X.; Zhou, L.; Yu, P. W.; Chen, R. J.; Sun, S. R. Revealing of active sites and catalytic mechanism in N-coordinated Fe, Ni dual-doped carbon with superior acidic oxygen reduction than single-atom catalyst. *J. Phys. Chem. Lett.* **2020**, *11*, 1404–1410.

[183] Zhang, C.; Sha, J.; Fei, H.; Liu, M.; Yazdi, S.; Zhang, J.; Zhong, Q.; Zou, X.; Zhao, N.; Yu, H. et al. Single-Atomic ruthenium catalytic site on nitrogen-doped graphene for oxygen reduction reaction in acidic medium. *ACS Nano* **2017**, *11*, 6930−6941.

[184] Zhang, Q. Q.; Duan, Z. Y.; Wang, Y.; Li, L. N.; Nan, B.; Guan, J. Q. Atomically dispersed iridium catalysts for multifunctional electrocatalysis. *J. Mater. Chem. A* **2020**, *8*, 19665–19673.

[185] Wan, G.; Yu, P. F.; Chen, H. R.; Wen, J. G.; Sun, C. J.; Zhou, H.; Zhang, N.; Li, Q. R.; Zhao, W. P.; Xie, B. et al. Engineering single-atom cobalt catalysts toward improved electrocatalysis. *Small* **2018**, *14*, 1704319.

[186] Wen, X. D.; Bai, L.; Li, M.; Guan, J. Q. Atomically dispersed cobalt- and nitrogen-codoped graphene toward bifunctional catalysis of oxygen reduction and hydrogen evolution reactions. *ACS Sustainable Chem. Eng.* **2019**, *7*, 9249–9256.

[187] Li, J. Z.; Chen, M. J.; Cullen, D. A.; Hwang, S.; Wang, M. Y.; Li, B. Y.; Liu, K. X.; Karakalos, S.; Lucero, M.; Zhang, H. G. et al. Atomically dispersed manganese catalysts for oxygen reduction in proton-exchange membrane fuel cells. *Nat. Catal.* **2018**, *1*, 935–945.

[188] Guan, J. Q.; Duan, Z. Y.; Zhang, F. X.; Kelly, S. D.; Si, R.; Dupuis, M.; Huang, Q. E.; Chen, J. Q.; Tang, C. H.; Li, C. Water oxidation on a mononuclear manganese heterogeneous catalyst. *Nat. Catal.* **2018**, *1*, 870–877.

[189] Zhang, Q. Q.; Guan, J. Q. Mono-/multinuclear water oxidation catalysts. *ChemSusChem* **2019**, *12*, 3209–3235.

[190] Luo, F.; Hu, H.; Zhao, X.; Yang, Z. H.; Zhang, Q.; Xu, J. X.; Kaneko, T.; Yoshida, Y.; Zhu, C. Z.; Cai, W. W. Robust and stable acidic overall water splitting on Ir single atoms. *Nano Lett.* **2020**, *20*, 2120–2128.

[191] Cao, L. L.; Luo, Q. Q.; Chen, J. J.; Wang, L.; Lin, Y.; Wang, H. J.; Liu, X. K.; Shen, X. Y.; Zhang, W.; Liu, W. et al. Dynamic oxygen adsorption on single-atomic Ruthenium catalyst with high performance for acidic oxygen evolution reaction. *Nat. Commun.* **2019**, *10*, 4849.

[192] Yao, Y. C.; Hu, S. L.; Chen, W. X.; Huang, Z. Q.; Wei, W. C.; Yao, T.; Liu, R. R.; Zang, K. T.; Wang, X. Q.; Wu, G. et al. Engineering the electronic structure of single atom Ru sites via compressive strain boosts acidic water oxidation electrocatalysis. *Nat. Catal.* **2019**, *2*, 304–313.

[193] Lei, C. J.; Chen, H. Q.; Cao, J. H.; Yang, J.; Qiu, M.; Xia, Y.; Yuan, C.; Yang, B.; Li, Z. J.; Zhang, X. W. et al. Fe-N_4 sites embedded into carbon nanofiber integrated with electrochemically exfoliated graphene for oxygen evolution in acidic medium. *Adv. Energy Mater.* **2018**, *8*, 1801912.

[194] Wang, L. G.; Duan, X. X.; Liu, X. J.; Gu, J.; Si, R.; Qiu, Y.; Qiu, Y. M.; Shi, D. E.; Chen, F. H.; Sun, X. M. et al. Atomically dispersed mo supported on metallic Co_9S_8 nanoflakes as an advanced noble-metal-free bifunctional water splitting catalyst working in universal pH conditions. *Adv. Energy Mater.* **2020**, *10*, 1903137.

[195] Qiu, Y.; Peng, X. Y.; Lü, F.; Mi, Y. Y.; Zhuo, L. C.; Ren, J. Q.; Liu, X. J.; Luo, J. Single-atom catalysts for the electrocatalytic reduction of nitrogen to ammonia under ambient conditions. *Chem. Asian J.* **2019**, *14*, 2770–2779.

[196] Cao, Y. Y.; Gao, Y. J.; Zhou, H.; Chen, X. L.; Hu, H.; Deng, S. W.; Zhong, X.; Zhuang, G. L.; Wang, J. G. Highly efficient ammonia synthesis electrocatalyst: Single Ru atom on naturally nanoporous carbon materials. *Adv. Theor. Simul.* **2018**, *1*, 1800018.

[197] Ling, C. Y.; Bai, X. W.; Ouyang, Y. X.; Du, A. J.; Wang, J. L. Single molybdenum atom anchored on N-doped carbon as a promising electrocatalyst for nitrogen reduction into ammonia at ambient conditions. *J. Phys. Chem. C* **2018**, *122*, 16842–16847.

[198] Li, X. F.; Li, Q. K.; Cheng, J.; Liu, L. L.; Yan, Q.; Wu, Y. C.; Zhang, X. H.; Wang, Z. Y.; Qiu, Q.; Luo, Y. Conversion of dinitrogen to ammonia by FeN_3-embedded graphene. *J. Am. Chem. Soc.* **2016**, *138*, 8706–8709.

[199] Huang, Y.; Yang, T. T.; Yang, L.; Liu, R.; Zhang, G. Z.; Jiang, J.; Luo, Y.; Lian, P.; Tang, S. B. Graphene–boron nitride hybrid-supported single Mo atom electrocatalysts for efficient nitrogen reduction reaction. *J. Mater. Chem. A* **2019**, *7*, 15173–15180.

[200] Zheng, X. N.; Yao, Y.; Wang, Y.; Liu, Y. Tuning the electronic structure of transition metals embedded in nitrogen-doped graphene for electrocatalytic nitrogen reduction: A first-principles study. *Nanoscale* **2020**, *12*, 9696–9707.

[201] Ou, P. F.; Zhou, X.; Meng, F. C.; Chen, C.; Chen, Y. Q.; Song, J. Single molybdenum center supported on N-doped black phosphorus as an efficient electrocatalyst for nitrogen fixation. *Nanoscale* **2019**, *11*, 13600–13611.

[202] Zhao, J.; Zhao, J. X.; Cai, Q. H. Single transition metal atom embedded into a MoS_2 nanosheet as a promising catalyst for electrochemical ammonia synthesis. *Phys. Chem. Chem. Phys.* **2018**, *20*, 9248–9255.

[203] Zhang, Q. Q.; Guan, J. Q. Single-atom catalysts for electrocatalytic applications. *Adv. Funct. Mater.* **2020**, *30*, 2000768.

[204] Wang, X. Q.; Wang, W. Y.; Qiao, M.; Wu, G.; Chen, W. X.; Yuan, T. W.; Xu, Q.; Chen, M.; Zhang, Y.; Wang, X. et al. Atomically dispersed Au_1 catalyst towards efficient electrochemical synthesis of ammonia. *Sci. Bull.* **2018**, *63*, 1246–1253.

[205] Qin, Q.; Heil, T.; Antonietti, M.; Oschatz, M. Single-site gold catalysts on hierarchical N-doped porous noble carbon for enhanced electrochemical reduction of nitrogen. *Small Methods* **2018**, *2*, 1800202.

[206] Geng, Z. G.; Liu, Y.; Kong, X. D.; Li, P.; Li, K.; Liu, Z. Y.; Du, J. J.; Shu, M.; Si, R.; Zeng, J. Achieving a record-high yield rate of 120.9 $\mu g_{NH_3} \cdot mg_{cat.}^{-1} \cdot h^{-1}$ for N_2 electrochemical reduction over Ru single- atom catalysts. *Adv. Mater.* **2018**, *30*, 1803498.

[207] Tao, H. C.; Choi, C.; Ding, L. X.; Jiang, Z.; Han, Z. S.; Jia, M. W.; Fan, Q.; Gao, Y. N.; Wang, H. H.; Robertson, A. W. et al. Nitrogen fixation by Ru single-atom electrocatalytic reduction. *Chem* **2019**, *5*, 204–214.

[208] Qiu, J. Z.; Hu, J. B.; Lan, J. G.; Wang, L. F.; Fu, G. Y.; Xiao, R. J.; Ge, B. H.; Jiang, J. X. Pure siliceous zeolite-supported Ru single-atom active sites for ammonia synthesis. *Chem. Mater.* **2019**, *31*, 9413–9421.

[209] Wang, M. F.; Liu, S. S.; Qian, T.; Liu, J.; Zhou, J. Q.; Ji, H. Q.; Xiong, J.; Zhong, J.; Yan, C. L. Over 56.55% Faradaic efficiency of ambient ammonia synthesis enabled by positively shifting the reaction potential. *Nat. Commun.* **2019**, *10*, 341.

[210] Lü, F.; Zhao, S. Z.; Guo, R. J.; He, J.; Peng, X. Y.; Bao, H. H.; Fu, J. T.; Han, L. L.; Qi, G. C.; Luo, J. et al. Nitrogen-coordinated single Fe sites for efficient electrocatalytic N_2 fixation in neutral media. *Nano Energy* **2019**, *61*, 420–427.

[211] Zhang, L. L.; Cong, M. Y.; Ding, X.; Jin, Y.; Xu, F. F.; Wang, Y.; Chen, L.; Zhang, L. X. A Janus Fe-SnO_2 catalyst that enables bifunctional electrochemical nitrogen fixation. *Angew. Chem., Int. Ed.* **2020**, *59*, 10888–10893.

[212] Zang, W. J.; Yang, T.; Zou, H. Y.; Xi, S. B.; Zhang, H.; Liu, X. M.; Kou, Z. K.; Du, Y. H.; Feng, Y. P.; Shen, L. et al. Copper single atoms anchored in porous nitrogen-doped carbon as efficient pH-universal catalysts for the nitrogen reduction reaction. *ACS Catal.* **2019**, *9*, 10166–10173.

[213] Han, L. L.; Liu, X. J.; Chen, J. P.; Lin, R. Q.; Liu, H. X.; Lü, F.; Bak, S.; Liang, Z. X.; Zhao, S. Z.; Stavitski, E. et al. Atomically dispersed molybdenum catalysts for efficient ambient nitrogen fixation. *Angew. Chem., Int. Ed.* **2019**, *58*, 2321–2325.

[214] Gong, N. Q.; Ma, X. W.; Ye, X. X.; Zhou, Q. F.; Chen, X. A.; Tan, X. L.; Yao, S. K.; Huo, S. D.; Zhang, T. B.; Chen, S. Z. et al. Carbon-dot-supported atomically dispersed gold as a mitochondrial oxidative stress amplifier for cancer treatment. *Nat. Nanotechnol.* **2019**, *14*, 379–387.

[215] He, F.; Mi, L.; Shen, Y. F.; Mori, T.; Liu, S. Q.; Zhang, Y. J. Fe–N–C artificial enzyme: Activation of oxygen for dehydrogenation and monoxygenation of organic substrates under mild condition and cancer therapeutic application. *ACS Appl. Mater. Interfaces* **2018**, *10*, 35327–35333.

[216] Huo, M. F.; Wang, L. Y.; Wang, Y. W.; Chen, Y.; Shi, J. L. Nanocatalytic tumor therapy by single-atom catalysts. *ACS Nano* **2019**, *13*, 2643–2653.

[217] Wang, L.; Qu, X. Z.; Zhao, Y. X.; Weng, Y. Z. W.; Waterhouse, G. I. N.; Yan, H.; Guan, S. Y.; Zhou, S. Y. Exploiting single atom Iron centers in a porphyrin-like MOF for efficient cancer phototherapy. *ACS Appl. Mater. Interfaces* **2019**, *11*, 35228–35237.

[218] Lu, X. Y.; Gao, S. S.; Lin, H.; Yu, L. D.; Han, Y. H.; Zhu, P.; Bao, W. C.; Yao, H. L.; Chen, Y.; Shi, J. L. Bioinspired copper single-atom catalysts for tumor parallel catalytic therapy. *Adv. Mater.* **2020**, *32*, 2002246.

[219] Wu, Y.; Jiao, L.; Luo, X.; Xu, W. Q.; Wei, X. Q.; Wang, H. J.; Yan, H. Y.; Gu, W. L.; Xu, B. Z.; Du, D. et al. Oxidase-like Fe-N-C single-atom nanozymes for the detection of acetylcholinesterase activity. *Small* **2019**, *15*, 1903108.

[220] Niu, X. H.; Shi, Q. R.; Zhu, W. L.; Liu, D.; Tian, H. Y.; Fu, S. F.; Cheng, N.; Li, S. Q.; Smith, J. N.; Du, D. et al. Unprecedented peroxidase-mimicking activity of single-atom nanozyme with atomically dispersed Fe–N_x moieties hosted by MOF derived porous carbon. *Biosens. Bioelectron.* **2019**, *142*, 111495.

[221] Huang, L.; Chen, J. X.; Gan, L. F.; Wang, J.; Dong, S. J. Single-atom nanozymes. *Sci. Adv.* **2019**, *5*, eaav5490.

[222] Chen, Q. M.; Li, S. Q.; Liu, Y.; Zhang, X. D.; Tang, Y.; Chai, H. X.; Huang, Y. M. Size-controllable Fe-N/C single-atom nanozyme with exceptional oxidase-like activity for sensitive detection of alkaline phosphatase. *Sens. Actuators B* **2020**, *305*, 127511.

[223] Cheng, N.; Li, J. C.; Liu, D.; Lin, Y. H.; Du, D. Single-atom nanozyme based on nanoengineered Fe–N–C catalyst with superior peroxidase-like activity for ultrasensitive bioassays. *Small* **2019**, *15*, 1901485.

[224] Wu, Y.; Wu, J. B.; Jiao, L.; Xu, W. Q.; Wang, H. J.; Wei, X. Q.; Gu, W. L.; Ren, G. X.; Zhang, N.; Zhang, Q. H. et al. Cascade reaction system integrating single-atom nanozymes with abundant Cu sites for enhanced biosensing. *Anal. Chem.* **2020**, *92*, 3373–3379.

[225] Wen, W.; Yan, X.; Zhu, C. Z.; Du, D.; Lin, Y. H. Recent advances in electrochemical immunosensors. *Anal. Chem.* **2017**, *89*, 138–156.

[226] Yao, L. L.; Gao, S. J.; Liu, S.; Bi, Y. L.; Wang, R. R.; Qu, H.; Wu, Y. E.; Mao, Y.; Zheng, L. Single-atom enzyme-functionalized solution-gated graphene transistor for real-time detection of mercury Ion. *ACS Appl. Mater. Interfaces* **2020**, *12*, 6268–6275.

[227] Hou, H. F.; Mao, J. J.; Han, Y. H.; Wu, F.; Zhang, M. N.; Wang, D. S.; Mao, L. Q.; Li, Y. Single-atom electrocatalysis: A new approach to *in vivo* electrochemical biosensing. *Sci. China Chem.* **2019**, *62*, 1720–1724.

[228] Gu, W. L.; Wang, H. J.; Jiao, L.; Wu, Y.; Chen, Y. X.; Hu, L. Y.; Gong, J. M.; Du, D.; Zhu, C. Z. Single-atom Iron boosts electrochemiluminescence. *Angew. Chem., Int. Ed.* **2020**, *59*, 3534–3538.